People's Democratic Republic of Algeria

Ministry of Higher Education and Scientific Research

Badji Moukhtar University

Faculty of Sciences

Departement of Physics

**Thesis**

Submitted for graduation DOCTORATE

**Field: Material Sciences Sector: Physics**

**Specialization: Condensed Matter Physics and their Applications**

**Laboratory: Nano-materials: Corrosion and Surface Treatment**

**Title**

# First-principles calculations based on various exchange-correlation potentials of the structural, mechanical, electronic, magnetic and thermodynamic properties of quaternary Heusler alloys

***Realized by:***

**MEGHCHOUCHE Houssam**

Defended in front of the jury:

| **Members** | **Grade** | **Institution** | **Quality** |
|---|---|---|---|
| DEBILI Mohamed Yacine | Prof. | Badji Moukhtar University | Chair |
| AMERI Mohammed | Prof. | Djilali Liabes University | Examiner |
| LEMLIKCHI Safia | MCA | CDTA Algiers | Examiner |
| BOUKOUIETE Amel | Prof. | Badji Moukhtar University | Examiner |
| LABIDI Malika | MCA | ENSTI Annaba | Supervisor |
| AMARA Abdelaziz | Prof. | Badji Moukhtar University | Co-supervisor |

**Year 2025**

République Algérienne Démocratique et Populaire
Ministère de l'Enseignement Supérieur et de la Recherche Scientifique

Université de Badji Moukhtar

Faculté des Sciences

Département de Physique

**THESE**

Présentée en vue de l'obtention du diplôme de DOCTORAT

**Domaine: Sciences de la Matière Filière: Physics**

**Option: Physique de la Matière Condensée et ses Applications**

**Laboratoire des Nanomatériaux: Corrosion et Traitement de Surface**

**Thème**

---

# Calcul de premiers principes basés sur divers potentiels d'échange-corrélation des propriétés structurales, mécaniques, électroniques, magnétiques et thermodynamiques des alliages Heusler quaternaires

---

***Présenté par: MEGHCHOUCHE Houssam***

Soutenue devant le jury:

| **Members** | **Grade** | **Institution** | **Qualité** |
|---|---|---|---|
| DEBILI Mohamed Yacine | Prof. | Université de Badji Moukhtar | Président |
| AMERI Mohammed | Prof. | Université de Djilali Liabes | Examinateur |
| LEMLIKCHI Safia | MCA | CDTA Alger | Examinateur |
| BOUKOUIETE Amel | Prof. | Université de Badji Moukhtar | Examinateur |
| LABIDI Malika | MCA | ENSTI Annaba | Encadreur |
| AMARA Abdelaziz | Prof. | Université de Badji Moukhtar | Co-encadreur |

**Année 2025**

# THANKS

THE *success of a doctorate owes much to the scientific and human environment in which it takes place. I would like to sincerely thank all the people who made this thesis work possible.*

*Firstly, i thank Almighty God for giving me courage, patience, and strength during all these years of research.*

*This work was carried out at the Nanomaterials, Corrosion, and Surface Treatment Laboratory (NCSTL), Faculty of Science, Department of Physics, Badji Mokhtar University. I would like to sincerely thank the director of this laboratory Mr. REHAMNIA Rabah, for kindly welcoming me to this laboratory.*

*My highest esteem and first thanks go to my thesis supervisor, Ms. LABIDI Malika, a lecturer at the National School of Technology and Engineering, who enthusiastically supervised my thesis. The trust she placed in me and her commitment allowed me to complete this work under the best possible conditions.*

*I would also like to thank Pr. AMARA Abdelaziz, who has always been able to motivate and co-direct my work. I cannot thank him enough for his advice, his human qualities, and the scientific and cultural knowledge he has provided me.*

*I express my warmest thanks to Mr. DEBILI Mohamed Yacine, Professor at the University of Annaba, for the honor bestowed upon me by agreeing to chair my thesis committee.*

*I would like to thank the members of the jury, Mr. AMERI Mohammed, Professor at the University of Sidi Bel Abbès, Ms. LEMLIKCHI Safia, Senior Lecturer at the Advanced Technology Development Center of Algeria, and Ms. BOUKOUIETE Amel, Professor at the University of Annaba, who agreed to judge and review this work.*

*I also express my sincere gratitude to Pr. LABIDI Salima and Dr. KALARASSE Fateh, who greatly benefited me from these fruitful discussions on computer codes. Their assistance was often invaluable.*

FINALLY, *a big thank you goes to my lovely family: my parents, my wife, my sisters, and my brothers. Thank you, all of you.*

# ABSTRACT

Recently, spintronics has shown as the future technology with potential applications that will replace the conventional electronics. In this field, materials with suitable properties called Heusler alloys are used. Heusler alloys have known major advances in the technological field, the purpose being to propose materials that meet industrial needs. Based on this, we are interested a family of smart materials that are the quaternary Heusler alloys, this class of materials are shown to be able to overcome these challenges as potential candidates with interesting properties (Curie temperature and spin polarization, etc.) for spintronic devices.

In this work, first principle calculations were performed to investigate the structural, mechanical, electronic, magnetic and thermodynamic properties of $d^0$ Heusler alloys KMgNZ (Z = O or S) and quaternary alloys with transition metals FeTiCrX (X = Al or Si) and their doped system $KMgNO_{1-x}S_x$ and $FeTiCrAl_{1-x}Si_x$ (x=0.25, 0.50 and 0.75), respectively. These properties were studied employing the full potential linearized augmented plane waves method (FP-LAPW) implemented in Wien2k package. The exchange-correlation potential was treated by generalized gradient approximation (GGA) in the calculation of the structural, mechanical and thermodynamic properties. While, for the electromagnetic properties the exchange and correlation potential was treated employing the modified Becke-Johnsom (mBJ) approach and GGA + U. Furthermore, a regular-solution model was used to explore the thermodynamic stability of the parent compounds and their doped alloys. The quasi-harmonic Debye model was used to study the behavior of thermodynamic properties under different temperatures and pressures.

**Key Words:** spintronics, Heusler alloys, Wien2k, Curie temperature, spin polarization.

# RÉSUMÉ

Récemment, la spintronique s'est révélée être la technologie d'avenir avec des applications potentielles qui remplaceront l'électronique conventionnelle. Dans ce domaine, des matériaux aux propriétés adaptées, appelés alliages Heusler, sont utilisés. Les alliages Heusler ont connu des avancées majeures dans le domaine technologique, le but étant de proposer des matériaux qui répondent aux besoins industriels. Sur cette base, nous nous intéressons à une famille de matériaux intelligents que sont les alliages Heusler quaternaires. Cette classe de matériaux se révèle capable de surmonter ces défis en tant que candidats potentiels avec des propriétés intéressantes (température de Curie et polarisation de spin, etc.) pour les dispositifs spintroniques.

Dans cette étude, des calculs de premier principe ont été effectués pour étudier la stabilité structurale ainsi que les propriétés mécaniques, électroniques, magnétiques et thermodynamiques des alliages Heusler $d^0$ KMgNZ (Z = O ou S) et des alliages quaternaires avec des métaux de transition FeTiCrX (X = Al ou Si) et leurs systèmes dopés $KMgNO_{1-x}S_x$ et $FeTiCrAl_{1-x}Si_x$ (x = 0,25, 0,50 et 0,75), respectivement. Ces propriétés ont été étudiées en utilisant la méthode des ondes planes augmentées linéarisées à potentiel complet (FP-LAPW) implémentée dans le code Wien2k. Le potentiel d'échange-corrélation été traité par l'approximation de gradient généralisée (GGA) dans le calcul des caractéristiques structurales, mécaniques et thermodynamiques. Alors que pour les propriétés électroniques et magnétiques, le potentiel d'échange et de corrélation a été traité en utilisant l'approche Becke-Johnsom modifiée (mBJ) et GGA + U. De plus, un modèle de solution régulière a été utilisé pour explorer la stabilité thermodynamique des composés parents et de leurs alliages dopés. Le modèle quasi-harmonique de Debye a été utilisé pour étudier le comportement des propriétés thermodynamiques sous différentes températures et pressions.

**Mots clé :** spintronique, alliages Heusler, Wien2k, température de Curie, polarisation de spin.

A

## ملخص

في الآونة الأخيرة، أظهرت السبينترونيك أنها التكنولوجيا المستقبلية ذات التطبيقات المحتملة التي ستحل محل الإلكترونيات التقليدية. في هذا المجال يتم استخدام مواد ذات خصائص مناسبة تسمى سبائك هويسلر. وقد شهدت سبائك هوسلر تقدمًا كبيرًا في المجال التكنولوجي، والغرض من ذلك هو اقتراح مواد تلبي الاحتياجات الصناعية. بناءً على ذلك، نحن مهتمون بعائلة من المواد الذكية التي هي سبائك هوسلر الرباعية. وقد ثبت أن هذه الفئة من المواد قادرة على التغلب على هذه التحديات كمرشحين محتملين بخصائص مثيرة للاهتمام (درجة حرارة كوري واستقطاب الدوران) لأجهزة الإلكترونيات الدورانية.

في هذا العمل، تم إجراء حسابات مبدئية أولية لدراسة الاستقرار الهيكلي وكذلك الخصائص الميكانيكية والإلكترونية والمغناطيسية والديناميكية الحرارية لسبائك KMgNZ (Z = O, S) وسبائك تحتوي على معادن انتقالية FeTiCrX (X = Al, Si) وأيضا أنظمتها المطعمة $KMgNO_{1-x}S_x$ و $FeTiCrAl_{1-x}Si_x$ ، على التوالي. تمت دراسة هذه الخصائص باستخدام طريقة الموجات المستوية المعززة الخطية ذات الجهد الكامل ( FP-LAPW ) ضمن نظرية الكثافة الوظيفية ( DFT ) المثبتة في كود Wien2k . تم معالجة جهد التبادل والارتباط بواسطة تقريبات التدرج المعممة ( GGA ) في حساب الخصائص الهيكلية والميكانيكية والديناميكية الحرارية. بالنسبة للخصائص الإلكترونية والمغناطيسية، تمت معالجة كمون التبادل والارتباط باستخدام نهج Becke-Johnsom المعدل ( mBJ ) و GGA + U . علاوة على ذلك، تم استخدام نموذج الحل المنتظم لاستكشاف الاستقرار الديناميكي الحراري للمركبات الأصلية وسبائكها المطعمة. بالإضافة إلى ذلك تم استخدام نموذج ديباي شبه التوافقي لمعرفة كيف تتغير الخصائص الديناميكية الحرارية، مثل السعة الحرارية والتمدد الحراري ودرجة حرارة ديباي والإنتروبيا، تحت درجة حرارة وضغوط مختلفة.

**كلمات مفتاحية:** سبينترونيك، سبائك هوسلر، DFT ، Wien2k ، درجة حرارة كوري، استقطاب الدوران.

# CONTENTS


0.1 Introduction . . . . . 1

**1 Heusler compounds in the field of spintronics** **9**
1.1 Introduction . . . . . 9
1.2 Heusler compounds . . . . . 10
1.3 Classification of Heusler compounds . . . . . 11
1.3.1 Half-Heusler compounds . . . . . 11
1.3.2 Full-Heusler compounds . . . . . 11
1.3.3 $d^0$ Heusler compounds . . . . . 11
1.4 Crystal structure of Heusler Compounds . . . . . 12
1.4.1 Half-Heusler compounds . . . . . 12
1.4.2 Full-Heusler compounds . . . . . 13
1.4.3 Inverse Heusler compounds . . . . . 14
1.4.4 Quaternary Heusler Compounds . . . . . 14
1.5 Half-metallic feature of Heusler compounds . . . . . 14
1.6 General view on spintronics . . . . . 15
1.7 Giant magnetoresistance GMR . . . . . 16
1.8 Tunnel magnetoresistance TMR . . . . . 18
1.9 Spintronics applications developments . . . . . 19
1.9.1 Magnetic field sensors . . . . . 19
1.9.2 Magnetic random access memory (MRAM) . . . . . 20
1.9.3 Read-Write heads of hard drives . . . . . 22

**2 Density functional theory (DFT)** **30**
2.1 Introduction . . . . . 30
2.2 Schrödinger equation of a solid . . . . . 31
2.3 Born-Oppenheimer approximation . . . . . 32
2.4 Hartree approximation . . . . . 33
2.5 Hartree-Fock approximation . . . . . 34
2.6 Density functional theory (DFT) . . . . . 34
2.6.1 Hohenberg and Kohn theorems . . . . . 35
2.7 Kohn and Sham equations . . . . . 36
2.8 Exchange and correlation potential . . . . . 37
2.9 Local density approximation (LDA) . . . . . 37
2.10 Generalized gradient approximation (GGA) . . . . . 38
2.11 Becke and Johnson modified potential (mBJ) . . . . . 39
2.12 GGA + U approximation . . . . . 39

2.13 Kohn-Sham equations resolution . . . . . 41

**3 FP-LAPW method** **45**
3.1 Introduction: . . . . . 45
3.2 Augmented planes waves method (APW): . . . . . 46
3.3 Basic functions of FP-LAPW method . . . . . 47
3.4 linearization . . . . . 49
3.5 Construction of non-relativistic radial functions . . . . . 49
3.6 Determination of coefficients $A_{lm}$ and $B_{lm}$ . . . . . 51
3.7 Potential determination . . . . . 52
3.7.1 Poisson equation resolution . . . . . 52
3.7.2 Exchange-correlation potential . . . . . 54
3.8 Improvement of the FP-LAPW method . . . . . 55
3.8.1 Multiple energy windows . . . . . 55
3.8.2 Development in local orbitals . . . . . 56
3.9 Concept of FP-LAPW method . . . . . 56
3.10 General description of the WIEN2K code . . . . . 57
3.10.1 WIEN2K algorithm . . . . . 58
3.10.2 SCF calculation . . . . . 58

**4 Results and discussion** **62**
4.1 Introduction . . . . . 62
4.2 Computational details . . . . . 63
4.3 Structural properties . . . . . 64
4.3.1 Equilibrium state and structural stability . . . . . 65
4.4 Mechanical properties . . . . . 70
4.4.1 Introduction . . . . . 70
4.4.2 Elastic properties . . . . . 70
4.4.3 Mechanical parameters . . . . . 72
4.5 Electronic properties . . . . . 78
4.5.1 Introduction . . . . . 78
4.5.2 Band structures . . . . . 78
4.5.3 Density of states . . . . . 83
4.6 Magnetic properties . . . . . 87
4.6.1 Introduction . . . . . 87
4.6.2 Magnetic moment of $KMgNO_{1-x}S_x$ alloys . . . . . 87
4.6.3 Magnetic moment of $FeTiCrAl_{1-x}Si_x$ alloys . . . . . 89
4.7 Thermodynamic properties . . . . . 91
4.7.1 Introduction . . . . . 91
4.7.2 Quasi-harmonic Debye model . . . . . 92
4.7.3 Heat capacity . . . . . 93
4.7.4 Thermal expansion . . . . . 94
4.7.5 Debye temperature . . . . . 95
4.7.6 Entropy . . . . . 97
4.7.7 Thermodynamic properties at different pressures . . . . . 97
4.8 Conclusion . . . . . 99

# LIST OF FIGURES


1.1 Different possible combinations of Heusler compounds. . . . . 10
1.2 Heusler alloys structures: (a) full-Heusler alloy, (b) inverse Heusler alloy, (c) half-Heusler alloy , and (d) quaternary Heusler alloy [31]. . . . . 13
1.3 Simple models of semiconductors (a), metallic ferromagnets (b), half-metallic ferromagnets (c), and spin gapless semiconductors (d). . . . . 15
1.4 **(a)** diagram of the GMR , **(b)** firsts observations of giant magnetoresistance on multilayers Fe/Cr(001). . . . . 17
1.5 **(a)** Tunneling transport for parallel ferromagnetic electrodes (P), **(b)** Tunneling transport for ferromagnetic antiparallel electrodes (AP) [54]. . . . . 18
1.6 **(a)** GMR tooth sensor modules for angle and length measurement, **(b)** TAS series TMR angle sensors, **(c)** GMR current sensors. . . . . 20
1.7 Magnetic random access memory architecture. . . . . 21
1.8 MRAM Standard cells **(a)** STT-MRAM **(b)** SOT-MRAM. . . . . 22
1.9 Hard drive architecture. . . . . 22
1.10 **(a)** Schematic of a GMR device, **(b)** GMR read-write head for hard drive [52]. 23

2.1 Algorithm implementation of Born-Oppenheimer approximation. . . . . 32
2.2 Cycle of SCF calculations for solving Kohn-Sham equations. . . . . 42

3.1 *Muffin-Tin* potential. . . . . 46
3.2 Solving the Poisson equation using the pseudo-charge method. . . . . 53
3.3 Calculation of exchange and correlation potential. . . . . 55
3.4 Structure of the WIEN2k code. . . . . 59

4.1 The crystal structure of KMgNZ (Z = O or S) and FeTiCrX (X = Al or Si) alloys in the three configurations. . . . . 65
4.2 The total energy as a function of unit cell volume of the alloys $KMgNO_{1-x}Si_x$ (a) and $FeTiCrAl_{1-x}Si_x$ (b) in the three different configurations. . . . . 66
4.3 Variation of the calculated lattice parameter $a_0$ and bulk modulus $B_0$ versus S/Si concentration. . . . . 69
4.4 3D surface of mechanical parameters of $KMgNO_{1-x}S_x$ alloys. . . . . 76
4.5 3D surface of mechanical parameters of $FeTiCrAl_{1-x}Si_x$ alloys. . . . . 77
4.6 Band structures of $KMgNO_{1-x}S_x$ for spin up (solid line) and spin down (dashed line). . . . . 80
4.7 Band structures of $FeTiCrAl_{1-x}Si_x$ for spin up (solid line) and spin down (dashed line). . . . . 82

4.8 DOS structures of $KMgNO_{1-x}S_x$ for spin up (solid line) and spin down (dashed line). . . . . 84
4.9 DOS structures of $FeTiCrAl_{1-x}Si_x$ for spin up (solid line) and spin down (dashed line). . . . . 86
4.10 Total and partial magnetic moment of $KMgNO_{1-x}S_x$ alloys versus S concentration. . . . . 89
4.11 Total and partial magnetic moment of $FeTiCrAl_{1-x}Si_x$ alloys versus Si concentration. . . . . 91
4.12 The heat capacity as a function of temperature. . . . . 94
4.13 Thermal expansion as a function of temperature. . . . . 95
4.14 Debye temperature as a function of temperature. . . . . 96
4.15 The entropy as a function of temperature. . . . . 97

# LIST OF TABLES


1.1 Three different occupancy for half-Heusler alloys. . . . . 13

4.1 RMT values of K, Mg, N, O, S, Fe, Ti, Cr, Al and Si atoms. . . . . 64
4.2 Three different occupancy for the parent compounds KMgNZ (Z = O or S) and FeTiCrX (X = Al or Si). . . . . 65
4.3 The equilibrium lattice parameter $a_0$(A), first derivative of the bulk modulus B′ (GPa) and the bulk modulus $B_0$ (GPa). . . . . 67
4.4 The ground state energy $E_{tot}$ (eV), cohesive energy $E_c$(eV/atom), formation energy $E_f$(eV/atom) and Curie temperature $T_c$(K). . . . . 68
4.5 Calculated elastic constants $C_{11}$, $C_{12}$, $C_{44}$ in GPa and melting temperature $T_m$(K). . . . . 71
4.6 Youngs modulus E(GPa), Shear modulus G(GPA), Bulk modulus B(GPa), Poisson's ratio $\nu$, anisotropic factor A, Cauchy pressure $C_P$(GPa), Pugh's ratio B/G, shear constant C′(GPa) and hardness $H_V$. . . . . 74
4.7 Calculated energy band gap (in eV) and the degree of spin polarization for $KMgNO_{1-x}S_x$ Heusler alloys. . . . . 79
4.8 Calculated energy band gap (in eV) and the degree of spin polarization for $FeTiCrAl_{1-x}Si_x$ Heusler alloys. . . . . 81
4.9 Total magnetic moment $M_{tot}$, interstitial magnetic moment $M_{int}$, partial magnetic moment $M_K$, $M_{Mg}$, $M_N$, $M_O$ and $M_S$ in $\mu_B$ for $KMgNO_{1-x}S_x$ alloys. . . . 88
4.10 Total magnetic moment $M_{tot}$, interstitial magnetic moment $M_{int}$, partial magnetic moment $M_{Fe}$, $M_{Ti}$, $M_{Cr}$, $M_{Al}$ and $M_{Si}$ in $\mu_B$ for $FeTiCrAl_{1-x}Si_x$ alloys. . . 90
4.11 Heat capacity $C_V/C_P$ , thermal expansion $\alpha$, Debey temperature $\theta_D$ and entropy S at different pressure P and constant temperature (300 K) for $KMgNO_{1-x}S_x$ alloys. . . . . 98
4.12 Heat capacity $C_V/C_P$ , thermal expansion $\alpha$, Debey temperature $\theta_D$ and entropy S at different pressure P and constant temperature (300 K) for $FeTiCrAl_{1-x}Si_x$ alloys. . . . . 99

# 0.1 Introduction

The development of technology and industry depends on the search for new materials from the periodic table of elements based on the natural law, which states that combining two different materials does not present a combination of their properties but rather gives rise to new characteristics specific to the compound.

Over the past few decades, the global pursuit of radical development in the realm of technology based on smart materials, environmentally friendly materials, and energy storage and control materials has led to intense interest from scientists and researchers in order to discover new, promising, and more effective materials that have new or perhaps exceptional properties. After the establishment of computational physics, which is based on algorithms installed on programs based on the first principle, theoretical prediction of the physical properties of these materials has become easier and more time-saving, as well as preserving the raw materials that make up the discovered materials. These computer programs have proven the experimental results to be reliable within the limits of uncertainty, which has made them a new destination for researchers in the technological field. Among these promising materials in the field of technological industries are insulators, semiconductors, half-metals, and metals, each of which has specific uses in a specific technological branch.

Since their first discovery by Friedrich Heusler in 1903 [1], half and full-Heusler alloys have provided excellent motivation for the development of new technologies and devices due to their rich properties, including high spin magnetic moments and high Curie temperatures [2, 3]. In various magnetic orders, these compounds can exhibit semiconductor, half-metallic, and metallic character. Due to their relatively high Curie temperature [4] and complete spin polarization [5, 6], half-metallic ferromagnets [7, 8] have garnered a lot of attention, particularly in the field of spintronics, such as spin-filters [9], spin injection devices [10], tunneling magnetoresistance (TMR), giant magnetoresistance (GMR) [11], spin-filters [12], magnetic data storage [13], spin-torque systems [14], and ferromagnetic shape memory alloys [15].

Heusler alloys fall into two subgroups and are often ternary materials made up of three different types of elements: X, Y, and Z. The first is known as half-Heusler alloys having the chemical formula XYZ, while the second is known as full-Heusler with a stoichiometric composition. The chemical formula for full-Heusler alloys is $X_2YZ$, where Z is a main group element and X and Y are transition or rare-earth atoms. When one atom X is swapped out for another atom X′, the complete Heusler structure gives rise to the quaternary Heusler alloy structure XX′YZ. The LiMgPdSn prototype crystal structure [16, 17] is widely recognized to

be adopted by the quaternary Heusler alloys with the general formula XX′YZ, where the X, X′, Y, and Z atoms occupy the Wyckoff position coordinates.

Half-Heusler alloys with half-metallic ferromagnet (HMF) characteristics are the most widely used materials for spintronic applications. For electrons with one spin orientation, the vast family of half-metallic ferromagnetic Heusler alloys is semiconductor, whereas, for electrons with the opposite spin orientation, they are metallic. These substances are appropriate materials for spintronics applications because they show complete spin polarization of conduction electrons. Ameri et al. and Missoum et al. have examined the optical properties and optoelectronic applications of half-Heusler alloys CoVX and NiTiX (X=Sb or Sn) and CoCrZ (Z=Al or Ga) [18, 19]. The electromagnetic, and thermodynamic characteristics of $Mn_2IrGe$ alloy were examined by Benaddi et al. [20]. According to the results, the spin down states have a semiconductor nature, whereas the spin up states have a metallic nature. Quaternary Heusler alloys have garnered more attention recently because of their half-metallicity and spin gapless band topologies [21, 22]. CoFeYGe (Y=Ti or Cr) half-metallic Heusler alloys have been studied by Haleoot et al. [23]; they show dynamical stability with very efficient thermoelectric and thermal characteristics. Rani et al. [24] performed an experimental and theoretical investigation on the possible half-metallic behavior of equiatomic quaternary Heusler alloys: CoRuMnGe and CoRuVZ (Z = Al or Ga). In addition, several investigations have been carried out to predict and examine the physical properties of EQH alloys, like FeRhCrSi and FePdCrSi [25], CoFeZrZ (Z = Ge, Sb) [26], FeCrRuSi [27], CoRuFeZ (Z = Si, Ge, Sn) [28], FeRhCrGe [29], FeZrTiZ (Z = Si, Sn, Pb) [30], YFeCrZ (Z = Al, Sb or Sn) [31], ( or ) [32], ZrFeTiZ (Z = Al, Si, Ge) [33] and FeZrCrZ (Z = Si, Ge, Sn) [34]. In addition, there are several works that have highlighted doped alloys, as $Co_2Mn_{1-x}Fe_xSi$ [35], $Fe_2VAl_{1-x}Si_x$ [36], $Fe_2Mn_xNi_{1-x}Si$ [37].

The determination of magnetic moments in Heusler alloys including magnetic transition metal components was the subject of much research in the past [38, 39]. The p-electrons of anions are the primary source and mediator of the magnetic order and spin polarization in sp or $d^0$ magnets, a novel class of materials devoid of magnetic transition metal that have emerged in recent years. Chen et al. [40] predicted that the half-Heusler alloys SnKCa and GeKCa were $d^0$ half-metallic ferromagnets. Using a theoretical analysis, Du et al. projected half-metallic (HM) characteristics in KCaNX (X=O, S, or Se) alloys [41]. Furthermore, the ferromagnetic materials NaXNO (X=Ca, Sr, or Ba) under study are thermodynamically, dynamically, and mechanically stable. They also show a half-metallic nature with 100% spin polarization, according to Belkacem et al. [42]. As far as we are aware, there have only been

a few research on this class of materials published in the literature thus far. In this work, we shed light on the physical properties of $KMgNO_{1-x}S_x$ (x = 00, 0.25, 0.50, 0.75 and 01) alloys, which were not predicted before.

Additionally, after a wide literature search, no theoretical or experimental results were revealed for $FeTiCrAl_{1-x}Si_x$ (x = 00, 0.25, 0.50, 0.75 and 01) alloys, except for the previous ab-initio investigation of the parent compounds FeTiCrAl and FeTiCrSi. K. Ozdogan et al. [43], investigated the electronic properties of FeTiCrAl and FeTiCrSi compounds and found that the former is a semiconductor whereas the latter has a half-metallic feature. G. Qiang et al. [44] shed light on the magnetic, elastic and electronic properties of FeTiCrAl and found that this material is ferromagnet with mechanical stability. Besides, R. Dhakal et al. [45], found that FeTiCrAl and FeTiCrSi alloys reveal mechanical and dynamical stability. The magnetic and electronic properties of FeCrTiAl under uniform (hydrostatic) pressure were investigated by V. Pavel et al. [46].

As a first step, we inspect and estimate the detailed ground state parameters of the whole alloys under consideration $KMgNO_{1-x}S_x$ and $FeTiCrAl_{1-x}Si_x$, with a focus on structural, mechanical, electronic, magnetic and thermodynamic characteristics, employing ab-initio calculations based on the density functional theory (DFT). The goal of this research is to find novel materials with half-metallic or semiconducting features suitable for spintronic applications and study the effect of doping on the structural, mechanical, electromagnetic and thermodynamic properties of the alloys of interest. Furthermore, this work is a comparison between the physical properties of $d^0$ alloys (without transition metals) with Heusler alloys containing transition elements.

# BIBLIOGRAPHY


[1] F. Heusler, "Über magnetische manganlegierungen," *Verh. Dtsch. Phys. Ges*, vol. 5, no. 12, p. 219, 1903.

[2] X. Wang, Z. Cheng, and W. Wang, "L21 and XA ordering competition in hafnium-based full-heusler alloys $Hf_2VZ$ (Z= Al, Ga, In, Tl, Si, Ge, Sn, Pb)," *Materials*, vol. 10, no. 10, p. 1200, 2017.

[3] C. Barman and A. Alam, "Topological phase transition in the ternary half-Heusler alloy ZrIrBi," *Physical Review B*, vol. 97, no. 7, p. 075302, 2018.

[4] P. Webster and K. Ziebeck, "Alloys and compounds of d-elements with main group elements. Part 2," *Landolt-Bornstein, New Series, Group III*, vol. 19, pp. 75–184, 1988.

[5] S. Li, Y. Takahashi, Y. Sakuraba, J. Chen, T. Furubayashi, O. Mryasov, S. Faleev, and K. Hono, "Current-perpendicular-to-plane giant magnetoresistive properties in $Co_2Mn(Ge_{0.75}Ga_{0.25})/Cu_2TiAl/Co_2Mn(Ge_{0.75}Ga_{0.25})$ all-Heusler alloy pseudo spin valve," *Journal of Applied Physics*, vol. 119, no. 9, p. 093911, 2016.

[6] Y. Feng, Z. Cui, M.-s. Wei, and B. Wu, "Spin-polarized quantum transport in $Fe_4N$ based current-perpendicular-to-plane spin valve," *Applied Surface Science*, vol. 466, pp. 78–83, 2019.

[7] Y. Ohnuma, M. Matsuo, and S. Maekawa, "Spin transport in half-metallic ferromagnets," *Physical Review B*, vol. 94, no. 18, p. 184405, 2016.

[8] M. Sun, Q. Ren, Y. Zhao, S. Wang, J. Yu, and W. Tang, "Magnetism in transition metal-substituted germanane: A search for room temperature spintronic devices," *Journal of Applied Physics*, vol. 119, no. 14, p. 143904, 2016.

[9] S. Datta and B. Das, "Electronic analog of the electro-optic modulator," *Applied Physics Letters*, vol. 56, no. 7, pp. 665–667, 1990.

[10] K. Kilian and R. Victora, "Electronic structure of Ni2MnIn for use in spin injection," *Journal of Applied Physics*, vol. 87, no. 9, pp. 7064–7066, 2000.

[11] C. Felser, G. H. Fecher, and B. Balke, "Spintronics: a challenge for materials science and solid-state chemistry," *Angewandte Chemie International Edition*, vol. 46, no. 5, pp. 668–699, 2007.

[12] S. Datta and B. Das, "Electronic analog of the electro-optic modulator," *Applied Physics Letters*, vol. 56, no. 7, pp. 665–667, 1990.

[13] T. Graf, C. Felser, and S. S. Parkin, "Simple rules for the understanding of Heusler compounds," *Progress in solid state chemistry*, vol. 39, no. 1, pp. 1–50, 2011.

[14] F. Wu, S. Mizukami, D. Watanabe, H. Naganuma, M. Oogane, Y. Ando, and T. Miyazaki, "Epitaxial $Mn_2$.5Ga thin films with giant perpendicular magnetic anisotropy for spintronic devices," *Applied Physics Letters*, vol. 94, no. 12, 2009.

[15] K. Ullakko, "JK Huang, C. Kantner, RC O'Handley and VV Kokorin," *Appl. Phys. Lett*, vol. 69, pp. 1966–1968, 1996.

[16] S. Dong and H. Zhao, "Pressure-induced ferromagnetism in open structure alkali metals from first principles," *Applied physics letters*, vol. 100, no. 14, p. 142404, 2012.

[17] F. Heusler, "Über Manganbronze und über die Synthese magnetisierbarer Legierungen aus unmagnetischen Metallen," *Angewandte Chemie*, vol. 17, no. 9, pp. 260–264, 1904.

[18] M. Ameri, A. Touia, R. Khenata, Y. Al-Douri, and H. Baltache, "Structural and optoelectronic properties of NiTiX and CoVX (X= Sb and Sn) half-Heusler compounds: An ab initio study," *Optik*, vol. 124, no. 7, pp. 570–574, 2013.

[19] A. Missoum, T. Seddik, G. Murtaza, R. Khenata, A. Bouhemadou, Y. Al-Douri, A. Abdiche, H. Meradji, and H. Baltache, "Ab initio study of the structural and optoelectronic properties of the half-Heusler CoCrZ (Z= Al, Ga)," *Canadian Journal of Physics*, vol. 92, no. 10, pp. 1105–1112, 2014.

[20] F. Benaddi, F. Belkharroubi, N. Ramdani, M. Ameri, S. Haouari, I. Ameri, L. Drici, S. Azzi, and Y. Al-Douri, "Electronic and magnetic investigation of half-metallic ferrimagnetic full-Heusler $Mn_2IrGe$," *Emergent Materials*, vol. 4, no. 6, pp. 1745–1760, 2021.

[21] A. Kundu, S. Ghosh, R. Banerjee, S. Ghosh, and B. Sanyal, "New quaternary half-metallic ferromagnets with large Curie temperatures," *Scientific reports*, vol. 7, no. 1, pp. 1–15, 2017.

[22] Y. Li, G. Liu, X. Wang, E. Liu, X. Xi, W. Wang, G. Wu, L. Wang, and X. Dai, "First-principles study on electronic structure, magnetism and half-metallicity of the NbCoCrAl and NbRhCrAl compounds," *Results in physics*, vol. 7, pp. 2248–2254, 2017.

[23] R. Haleoot and B. Hamad, "Thermodynamic and thermoelectric properties of CoFeYGe (Y= Ti, Cr) quaternary Heusler alloys: first principle calculations," *Journal of Physics: Condensed Matter*, vol. 32, no. 7, p. 075402, 2019.

[24] D. Rani, L. Bainsla, K. Suresh, and A. Alam, "Experimental and theoretical investigation on the possible half-metallic behaviour of equiatomic quaternary Heusler alloys: CoRuMnGe and CoRuVZ (Z= Al, Ga)," *Journal of Magnetism and Magnetic Materials*, vol. 492, p. 165662, 2019.

[25] L. Feng, J. Ma, Y. Yang, T. Lin, and L. Wang, "The electronic, magnetic, half-metallic and mechanical properties of the equiatomic quaternary heusler compounds FeRhCrSi and FePdCrSi: A first-Principles Study," *Applied Sciences*, vol. 8, no. 12, p. 2370, 2018.

[26] A. Maafa, L. Blaha, H. Rozale, A. Ougilas, M. Boukli, and A. Sayade, "Electronic properties, stability and thermoelectric response of CoFeZrZ (Z= Ge, Sb) quaternary Heuslers," *Materials Chemistry and Physics*, vol. 263, p. 124405, 2021.

[27] X. Wang, H. Khachai, R. Khenata, H. Yuan, L. Wang, W. Wang, A. Bouhemadou, L. Hao, X. Dai, R. Guo, *et al.*, "Structural, electronic, magnetic, half-metallic, mechanical, and thermodynamic properties of the quaternary Heusler compound FeCrRuSi: a first-principles study," *Scientific reports*, vol. 7, no. 1, p. 16183, 2017.

[28] K. Benkaddour, A. Chahed, A. Amar, H. Rozale, A. Lakdja, O. Benhelal, and A. Sayede, "First-principles study of structural, elastic, thermodynamic, electronic and magnetic properties for the quaternary Heusler alloys CoRuFeZ (Z= Si, Ge, Sn)," *Journal of Alloys and Compounds*, vol. 687, pp. 211–220, 2016.

[29] Y. Venkateswara, S. S. Samatham, P. Babu, K. Suresh, and A. Alam, "Coexistence of spin semimetal and Weyl semimetal behavior in FeRhCrGe," *Physical Review B*, vol. 100, no. 18, p. 180404, 2019.

[30] J. Sudharsan, M. Srinivasan, P. Ramasamy, M. K. Choudhary, P. Ravindran, *et al.*, "First-principles calculations to investigate new ferromagnetic quaternary Heusler alloys FeZrTiZ (Z= Si, Sn, Pb): Compatible for spin polarized device and waste heat recovery applications," *Solid State Sciences*, vol. 132, p. 106964, 2022.

[31] S. Idrissi, S. Ziti, H. Labrim, L. Bahmad, I. El Housni, R. Khalladi, S. Mtougui, and N. El Mekkaoui, "Half-metallic behavior and magnetic proprieties of the quaternary Heusler alloys YFeCrZ (Z= Al, Sb and Sn)," *Journal of Alloys and Compounds*, vol. 820, p. 153373, 2020.

[32] R. Haleoot and B. Hamad, "Thermodynamic and thermoelectric properties of CoFeYGe (Y= Ti, Cr) quaternary Heusler alloys: first principle calculations," *Journal of Physics: Condensed Matter*, vol. 32, no. 7, p. 075402, 2019.

[33] S. Berri, M. Ibrir, D. Maouche, and M. Attallah, "First principles study of structural, electronic and magnetic properties of ZrFeTiAl, ZrFeTiSi, ZrFeTiGe and ZrNiTiAl," *Journal of magnetism and magnetic materials*, vol. 371, pp. 106–111, 2014.

[34] H. Frioui, A. Meddour, and M. H. Gous, "Structural, mechanical, electronic, magnetic, optical, and thermoelectric properties of a new equiatomic quaternary heusler compound FeZrCrZ (Z= Si, Ge, Sn): A first-principles investigation," *Materials Science in Semiconductor Processing*, vol. 182, p. 108697, 2024.

[35] B. Balke, G. H. Fecher, H. C. Kandpal, C. Felser, K. Kobayashi, E. Ikenaga, J.-J. Kim, and S. Ueda, "Properties of the quaternary half-metal-type Heusler alloy $Co_2Mn_{1-x}Fe_xSi$," *Physical Review B—Condensed Matter and Materials Physics*, vol. 74, no. 10, p. 104405, 2006.

[36] C. S. Lue, C. Chen, J. Lin, Y. Yu, and Y. Kuo, "Thermoelectric properties of quaternary Heusler alloys $Fe_2VAl_{1-x}Si_x$," *Physical Review B—Condensed Matter and Materials Physics*, vol. 75, no. 6, p. 064204, 2007.

[37] S. Noui, Z. Charifi, H. Baaziz, G. Uğur, and Ş. Uğur, "Effect of structure on the electronic, magnetic and thermal properties of cubic $Fe_2Mn_xNi_{1-x}Si$ Heusler alloys," *Journal of Electronic Materials*, vol. 48, pp. 337–351, 2019.

[38] S. Amari and B. Bouhafs, "Electronic, elastic, and magnetic properties of the full-heusler with the 4d transition metal element, $Co_2YSi$, $Co_2ZrSi$, and $Co_2Y_{0.5}Zr_{0.5}Si$: a first-principle study," *Journal of Superconductivity and Novel Magnetism*, vol. 29, no. 9, pp. 2311–2317, 2016.

[39] B. Balke, H. C. Kandpal, G. H. Fecher, and C. Felser, "The half-metallic ferromagnet $Co_2Mn_{0.5}Fe_{0.5}Si$," *Journal of magnetism and magnetic materials*, vol. 310, no. 2, pp. 1823–1825, 2007.

[40] J. Chen, G. Gao, K. Yao, and M. Song, "Half-metallic ferromagnetism in the half-Heusler compounds GeKCa and SnKCa from first-principles calculations," *Journal of alloys and compounds*, vol. 509, no. 42, pp. 10172–10178, 2011.

[41] J. Du, S. Dong, X. Wang, H. Rozale, H. Zhao, L. Wang, and L. Feng, "Half-metallic ferromagnetism in KCaNX (X= O, S, and Se) quaternary Heusler compounds: A first-principles study," *Superlattices and Microstructures*, vol. 105, pp. 39–47, 2017.

[42] K. Belkacem, Y. Zaoui, S. Amari, L. Beldi, and B. Bouhafs, "First-principles study of the new half-metallic ferromagnetic quaternary-Heusler alloys NaXNO (X= Ca, Sr, Ba)," in *Spin*, vol. 10, p. 2050022, World Scientific, 2020.

[43] K. Özdoğan, E. Şaşıoğlu, and I. Galanakis, "Slater-Pauling behavior in LiMgPdSn-type multifunctional quaternary Heusler materials: Half-metallicity, spin-gapless and magnetic semiconductors," *Journal of Applied Physics*, vol. 113, no. 19, 2013.

[44] Q. Gao, I. Opahle, and H. Zhang, "High-throughput screening for spin-gapless semiconductors in quaternary Heusler compounds," *Physical Review Materials*, vol. 3, no. 2, p. 024410, 2019.

[45] R. Dhakal, S. Nepal, I. Galanakis, R. P. Adhikari, and G. C. Kaphle, "Prediction of half-metallicity and spin-gapless semiconducting behavior in the new series of FeCr-based quaternary Heusler alloys: an Ab initio study," *Journal of Alloys and Compounds*, vol. 882, p. 160500, 2021.

[46] P. V. Lukashev, S. McFadden, P. M. Shand, and P. Kharel, "Pressure modulated spin-gapless semiconductivity in FeCrTiAl," *Journal of Magnetism and Magnetic Materials*, vol. 584, p. 171107, 2023.

# CHAPTER 1

# HEUSLER COMPOUNDS IN THE FIELD OF SPINTRONICS

## 1.1 Introduction

Due to the attraction between magnetite and iron, magnetic facts have been observed, these phenomena have constantly attracted the attention of scientists, especially following the significant advancement in the theory of magnetism over the $19^{th}$ century, particularly following Curie's discovery of the para-magnetic, dia-magnetic, and ferro-magnetic phenomena and Dirac's determination of the electron's intrinsic magnetic moment.

The electromagnetic characteristics of solids have been exploited in the field of technology, where they are incorporated into most electronic components in various electronic devices for use. In the recent decades, a novel field in electronics has attracted a lot of attention lately, which is the spintronic. The basic premise is that an electron has a spin in addition to its charge. In the context of spintronics, the spins of electrons, not just their electric charges, are controlled in the operation of information transfer in circuits.

The development of spintronics therefore requires the use of materials with strong spin polarization. Half-metals are characterized by a 100% rate of spin polarization at Fermi level and therefore possess enormous potential for use in spintronic components like magnetic sensors and magnetic random-access memories (MRAMs). These materials are therefore ideal sources for highly spin-polarized currents, allowing high rates of magnetoresistance to be achieved. Theoretically, certain types of materials, such as $Fe_3O_4$ [1, 2] and Heusler alloys [3, 4], have been predicted to be half-metals. Furthermore, this half-metallic property has been demonstrated experimentally at low temperatures. However, half-metallic oxides have a low Curie temperature and therefore the spin polarization must be negligible at room temperature. While Heusler alloys are promising materials for spintronic applications because

many of them generally have high Curie temperatures [5] and therefore offer a possibility of possessing the half-metallic character even at temperatures above the room temperature.

## 1.2 Heusler compounds

The prototype of Heusler compounds is the $Cu_2MnSn$ alloy, which was discovered by Friedrich Heusler in 1903 [6], where its crystal structure was determined by Bradley and Rodgers in 1934 [7]. They demonstrated that at the ambient temperature, the ferromagnetic phase has a perfectly ordered structure of type $L2_1$ [7]. Indeed, their particularity and their properties are completely different from these constituent elements; for example, $Cu_2MnSn$ compound is a magnetic material, although neither Cu, Mn nor Sn are magnetic in nature [6]. Another example that of TiNiSn alloy [8, 9], which has the behavior of a semiconductor, even though it is composed of three metals [10]. In other word, regardless of the nature of its constituent elements, this kind of materials could have the behavior of metals, half-metals, semiconductors and superconductor.

This previous work gives birth to a new class of the most exciting materials; which contains more than 3000 identified compounds. They are divided into two groups: the half-Heuslers with a composition XYZ and the full-Heusler alloys with the chemical formula $X_2YZ$, where X and Y are transition metals and Z is a semiconductor or non-magnetic element. The main combinations of Heusler alloys are presented in Figure.1.1:

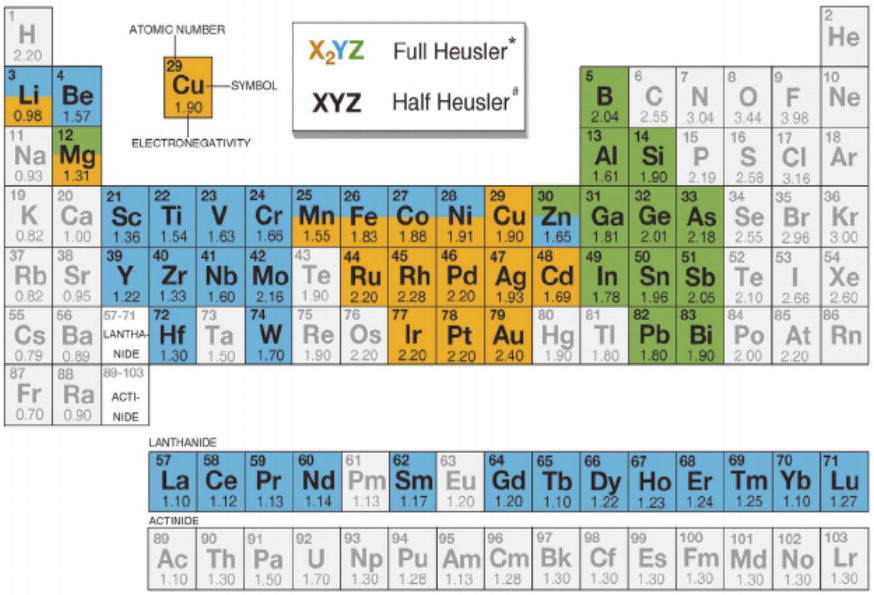


Figure 1.1: Different possible combinations of Heusler compounds.

## 1.3 Classification of Heusler compounds

### 1.3.1 Half-Heusler compounds

In general, half-Heusler alloys can be considered as composites that consist of two different parts, a covalent part and an ionic part. Accordingly, Z can be regarded as equivalently anionic, whereas X and Y atoms have a distinct cationic nature [11]. The nomenclature in the literature does not vary by the alphabetical order of the elements or in a random way but it varies by their degree of electronegativity. The formula starts with the most electropositive element, which could be a rare earth element, transition metal, or main group element. While the most electronegative element is found at end, it is considered as a main group element from the second half of the periodic table, for example, the case of LiAlSi, ZrNiSn, and LuAuSn [12, 13].

### 1.3.2 Full-Heusler compounds

Heusler compounds are often known as full-Heusler alloys, which are a class of intermetallic compounds. The typical formula for these alloys is $X_2YZ$, where X and Y are transition metals, and Z is an element from the periodic table groups III, IV, or V. But occasionally, an alkaline earth metal or a rare earth element takes the role of Y. The element of the group III, IV, or V in the periodic table is typically placed at the end of the formula, while the element that exists in duplicate is typically placed at the beginning, e.g., $Co_2MnSi$, $Fe_2VAl$ [14, 15]. There are a few exceptions where the order can be changed and in which order is chosen by the location of the most electropositive element, for example, $LiCu_2Sb$ and $YPd_2Sb$ [16]. Here, the electropositive element is placed at the beginning in accordance with the nomenclature of the International Union of Pure and Applied Chemistry (IUPAC). Another family exists for Heusler alloys; it is the case of quaternary Heusler compounds, where there are four atoms of different chemical nature with two elements different X and X'. The quaternary Heusler alloy structure, which has the general formula XX'Y Z, arises from the full Heusler structure when the X atom is substituted by another atom X'.

### 1.3.3 $d^0$ Heusler compounds

The extensive research for new materials in the field of technology led to the discovery of new promising materials without magnetic transition metals or rare earth elements that are formed only by intrinsically non-magnetic elements [17, 18], so-called sp or $d^0$ materials. The p-electrons of anions are the primary source of these compounds' magnetic order and spin

polarization. Furthermore, the half-metallic (HM) character and the magnetism associated with the non-magnetic elements with p-type orbitals in both half-Heusler and full-Heusler alloys [19, 20].

Chen et al. predicted the half-metallic ferromagnet feature of SnKCa and GeKCa $d_0$ half-Heusler alloys [21]. Beldi et al. published a theoretical study of the ternary Heusler alloys GeNaZ (Z = Ca, Sr, and Ba) in the three phases $\alpha$, $\beta$, and $\gamma$ [22]. They demonstrated the elastic and dynamic stability of these alloys in the phase $\alpha$ and predicted the half-metallic property. Recently, Wei et al. [23] reported on the electronic and magnetic stability of Heusler CNaCa and SiNaCa ternary alloys, using the method of local and full potential orbitals (FPLO). The structural, electro-magnetic characteristics of half-Heusler alloys RbSrZ (Z=C, Si and Ge) were investigated using full potential linearized augmented plane wave (FP-LAPW) method; Rozale et al. [24] confirm that these alloys reveal a half-metallic ferromagnetic character. Umamaheswari et al. [25] investigated the physical properties of half-Heusler ferromagnets of type XYZ (X = Li, Na, K and Rb; Y = Mg, Ca, Sr and Ba; Z = B, Al and Ga) utilizing the linearized muffin-tin orbitals atomic-sphere approximation coupled with the tight binding method (TB-LMTO-ASA).

The equiatomic quaternary Heusler alloys XX'YZ [26] are a novel type of Heusler alloys that are currently in use, these alloys have aroused great interest because of the perfect spin polarization and high Curie temperature $T_C$. More recently, in the framework of density functional theory, the half-metallic feature has been predicted in several types of quaternary Heusler alloys. But up to date, there are only a few studies focused on the electronic and magnetic structure of quaternary Heusler alloys without the incorporation of transition metals. Using an ab-initio research, Du et al. expected the half-metallic property in KCaNX (X=O, S, or Se) alloys [27]. Additionally, the NaXNO (X=Ca, Sr, or Ba) alloys are dynamically and elastically stable, and they show half-metallic character with perfect spin polarization, according to Belkacem et al. [18].

## 1.4 Crystal structure of Heusler Compounds

### 1.4.1 Half-Heusler compounds

The $C1_b$ structure is the crystal structure of half-Heusler alloys. In other words, they crystallize in a non-centrosymmetric cubic structure (space group No. 216, F-43m) formed by the filling octahedral sites of the lattice from a ZnS-type tetrahedral structure (Figure.1.2). This type of structure can be characterized by the interpenetration of three face-centered

cubic (fcc) sub-lattices, each of which is occupied by atoms X, Y and Z [28]. According to the following Wyckoff positions: 4a (0, 0, 0), 4b (1/2, 1/2, 1/2), and 4c (1/4, 1/4, 1/4), three atomic configurations can be formed, not equivalent to this type of structure ($C1_b$ ). Table 1.1 represents these different configurations (Type I and II are the favorable). The majority of

Table 1.1: Three different occupancy for half-Heusler alloys.

| Type | X | Y | Z |
|---|---|---|---|
| Type I | 4a | 4b | 4c |
| Type II | 4b | 4c | 4a |
| Type III | 4c | 4a | 4b |

half-Heusler compounds follow the atomic arrangement of the compound MgCuSb [29, 30], where the elements Y and Z form a ZnS-type covalent sublattice, while X (electropositive) and Y (electronegative) form an NaCl-type cell.

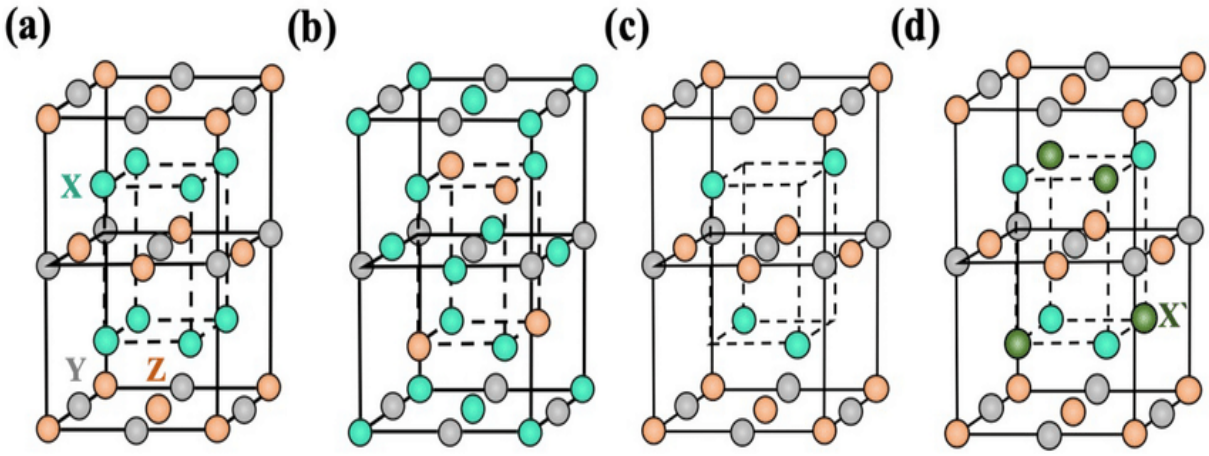


Figure 1.2: Heusler alloys structures: (a) full-Heusler alloy, (b) inverse Heusler alloy, (c) half-Heusler alloy , and (d) quaternary Heusler alloy [31].

### 1.4.2 Full-Heusler compounds

Full-Heusler materials have the form $X_2YZ$ where X and Y are transition or noble metals like Fe, Co, Ni, Mn, Cu etc. and Z is usually a IIIB or IVB element such as Al, In, Si, Ge or Sn. These compounds crystallize in cubic structure with space group Fm-3m (225) with the $Cu_2MnAl$ prototype [6, 32, 33]. This consists of four interpenetrating face-centered cubic (fcc) sublattices (Figure.1.2). One sublattice is occupied by Y and Z atoms, while the other two are occupied by X atoms. In the primitive cell of the $L2_1$ structure, the FCC primitive cell is based on four atoms. The Y and Z atoms are situated at 4a (0, 0, 0) and 4b (1/2, 1/2, 1/2), whereas the X atoms occupy the Wyckoff coordinates 8c (1/4, 1/4, 1/4).

### 1.4.3 Inverse Heusler compounds

If the valence of the X transition metal atom is less than that of the Y transition metal atom from the same period, then full-Heusler alloys are typically inverse Heusler compounds. They crystallize in the so-called $X_\alpha$ structure with space group F-43m. Usually, the element X is more electropositive than Y. In the inverse Heusler structure, X and Z atoms create a rock salt lattice to produce octahedral holes with four-fold symmetry, as opposed to the typical Heusler structure, where all of the X atoms occupy tetrahedral holes. Y and Z atoms are situated at 4c (1/4, 1/4, 1/4) and 4a (0, 0, 0), respectively, while X atoms have Wyckoff locations of 4b (1/2, 1/2, 1/2) and 4d (3/4, 3/4, 3/4) (Figure.1.2). The prototype of this structure is $Hg_2TiCu$. It is possible to emphasize the difference to regular Heusler compounds by expressing the formula as (XY)XZ.

### 1.4.4 Quaternary Heusler Compounds

The ordered quaternary full-Heusler compounds are usually named as LiMgPdSn-type, which have the chemical formula (XX')YZ where X, X' and Y are transition metal atoms where the valence of X' is lower than that of X atoms and the valence of the Y elements is lower than that of X and X' atoms [34, 35]. This structure exhibits a primitive FCC cell with a basis containing four atoms on the Wyckoff positions 4a to 4d, which form a larger cubic cell. The exchange of the atoms between 4a and 4b or 4c and 4d positions and between groups (4a, 4b)$\longleftrightarrow$(4c, 4d) does not change the structure due to symmetry implied by the F-43m space group (Figure.1.2).

## 1.5 Half-metallic feature of Heusler compounds

The term "**half-metallic**" feature was first introduced by Groot et al. [4], focusing on the calculation of the band structure of half-Heusler NiMnSb [36]. Conventional ferromagnetic materials have a density of states ($N\uparrow(E_F)$ and ($N\downarrow(E_F)$ at Fermi level for the spin up and down channels, respectively. It can then define the spin polarization, which measures the spin asymmetry employing the following formula [37]:

$$P\% = \frac{N\uparrow(E_F) - N\downarrow(E_F)}{N\uparrow(E_F) + N\downarrow(E_F)} \times 100 \tag{1.1}$$

Half-metallic compounds (P=100% ) show conduction properties completely different between the majority spins and minority spins states; one of them shows a metallic property

(crosses the Fermi level) and a semiconducting or even insulating property for the other spin direction (no states at the Fermi level). All of these features are illustrated in Figure.1.3.

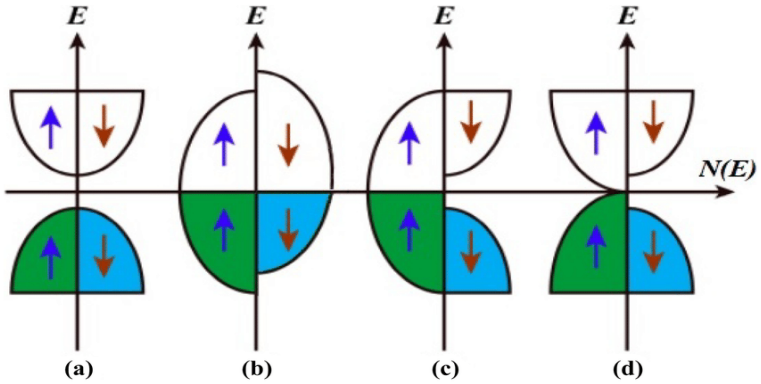


Figure 1.3: Simple models of semiconductors (a), metallic ferromagnets (b), half-metallic ferromagnets (c), and spin gapless semiconductors (d).

Heusler alloys are generally known in the form of ternary compounds, but they can also be in quaternary form, such as, for example, $Co_2Fe(Al, Si)$ alloys [38] and Co2(Fe, Cr)Al [39]. Gercsi et al. [38] studied the alloys based on cobalt, of quaternary form, such as $Co_2FeSi_{1-x}Al_x$, and have demonstrated that the addition of Al results in a reduction in the width of the band gap of spin down states. Xu et al. [38] studied the half-metallic feature of $Co_2FeAl$ in a massif form and in a thin layer, respectively, and showed that the half-metallic feature attenuates with the reduction of size. This decrease is usually associated with chemical disorder [39].

## 1.6 General view on spintronics

The microelectronics industry based on silicon has been the driving force technology of modern society, notably with the inventions of the transistor in 1947 [40] and the integrated circuit in 1958 [41]. The key point for the rapid progress in this area is the miniaturization of devices. Thanks to the miniaturization of transistors, the logic evolution tends towards an increasing integration of functions electronics on a single chip. This reduces weight and increases circuit integration densities while improving their performance (speed, consumption, etc.). The challenges of miniaturization have led the world of microelectronics to look in new directions for research that can supplant conventional electronics. One of the alternatives is the exploitation of another degree of freedom, which is the "**spin**" of the electron, because the classical electronics only depend on their charge. This second property of the electron could be described as the rotation of this particle on itself. It is the quantum equivalent of angular momentum in classical physics. The quantum angular momentum is the origin of the

magnetic moment carried by a particle possessing a spin; therefore, every particle having a spin can be seen as a tiny magnet. The exploitation of this additional property of the electron gave rise to a new discipline of solid state physics called spin electronics [42]. Spintronics, or spin electronics, also known as magnetoelectronics [43, 44], can be defined as electronics that take advantage of the electrons' spin in addition to their charge. It evolved when the giant magnetoresistance (GMR) was discovered in 1988 [45, 46]. The basic idea behind spintronics is to place ferromagnetic materials on the electron's path and to use the influence of the spin on the electrons' mobility in these materials. This influence, first suggested by Mott [47] in 1936, was then demonstrated experimentally and described theoretically at the end of 1960 [48, 49]. The discovery of GMR has led to the first practical uses of this influence. Many other phenomena exploiting also the spin of the electrons are then revealed, and today, spintronics is developing in many directions.

The use of spin in the storage of information leads to benefits such as:

1. The non-volatility of the information stored when the computer is turned off.
2. Obtaining much information bit processing speeds faster.
3. The significant drop in electricity consumption (a standard processor uses a lot of current and must be effectively cools).

## 1.7 Giant magnetoresistance GMR

In 1988 in Orssay, the giant magnetoresistance was discovered by two teams of researchers: a team by Albert Fert and that of Peter Grünberg [45, 46], during their studies of Fe/Cr/Fe in superlattices and trilayers, respectively. They have noted that the electrical current resistance from one layer to another depends on the relative alignment of the magnetization of each iron layer. This magnetoresistance effect is manifested in multilayer assemblies ferromagnetic/nonmagnetic. The thickness of these multilayers does not exceed a few atomic layers. At this scale of matter (nanometric scale), it is the quantum physics that dictates its laws, and we turn to the exploitation of spin instead of charge. This breakthrough allowed the creation of hard drives with a much greater density of information on the disks.

Figure.1.4 illustrates the general mechanism of the giant magnetoresistance in ferromagnetic multilayer structures alternating: two ferromagnetic layers separated by a non-magnetic layer thinner than the mean free path of electrons.

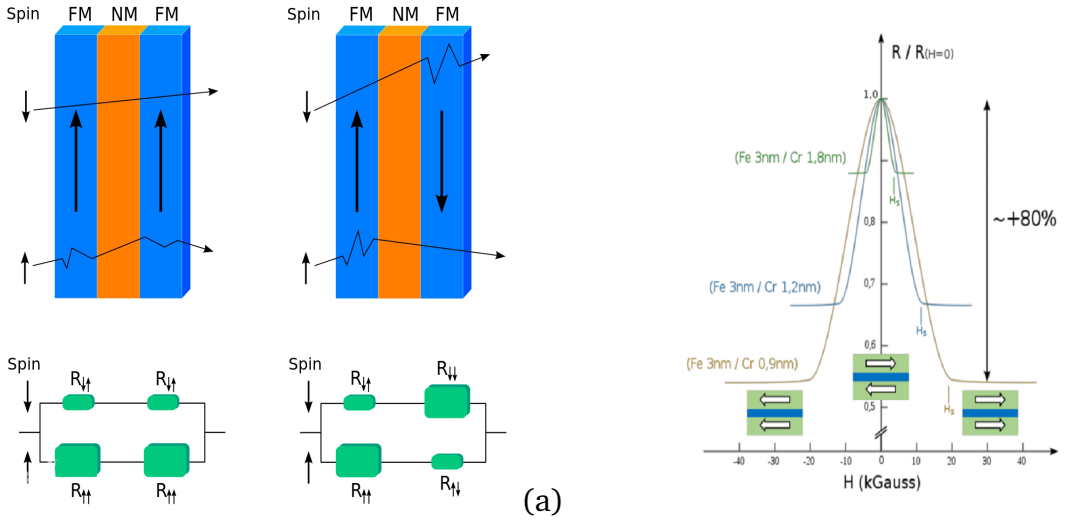


Figure 1.4: **(a)** diagram of the GMR , **(b)** firsts observations of giant magnetoresistance on multilayers Fe/Cr(001).

On the left, in the antiparallel magnetic configuration (AP) (Figure.1.4-a), the electrons circulate more easily when their magnetization points in the same direction as the magnetization of the layers. The resistance of the bilayer is high under these conditions (antiparallel magnetic configuration) because all of the electrons are blocked either at the beginning or at the end (Figure.1.4-b). When we apply an external magnetic field, we reverse the magnetization of a layer, and one falls under these conditions on the parallel magnetic configuration (P) (Figure.1.4-a). In this case, half electrons are no longer blocked, and the resistance is much lower.

Briefly, the magnetoresistance manifests as the difference in electrical resistance between two configurations, one where the ferromagnetic layers are parallelly magnetized, and the other where they are antiparallelly magnetized. The ratio of magnetoresistance MR (effect of size) is given by the following relationship:

$$GMR = \frac{\Delta R}{R} = \frac{R_{\uparrow\downarrow} - R_{\uparrow\uparrow}}{R_{\uparrow\uparrow}} \tag{1.2}$$

Where the system's equivalent resistances in the parallel and antiparallel alignments are denoted by $R_{\uparrow\downarrow}$ and $R_{\uparrow\uparrow}$, respectively.

This discovery was crowned by a Nobel Prize in Physics in October 2007 [50, 51]. Then, many efforts have been made in terms of experimental and theoretical research for the exploitation of GMR in the field of spintronics, and the best known of its applications concerns the read/write heads of computer hard disks [52].

## 1.8 Tunnel magnetoresistance TMR

Another characteristic effect of spintronics similar to giant magnetoresistance (GMR) is the Tunnel Magnetoresistance (TMR). The structures called magnetic tunnel junctions use a thin layer of dielectric material (for example, the layer of alumina $Al_2O_3$ with a thickness of 1.5 nm) between the two ferromagnetic layers (electrodes) [53], as shown schematically in Figure. 1.5. The interstitial layer prevents the passage of electrons (an energy barrier), while the tunneling effect ensures that this phenomenon occurs in a purely quantum way.

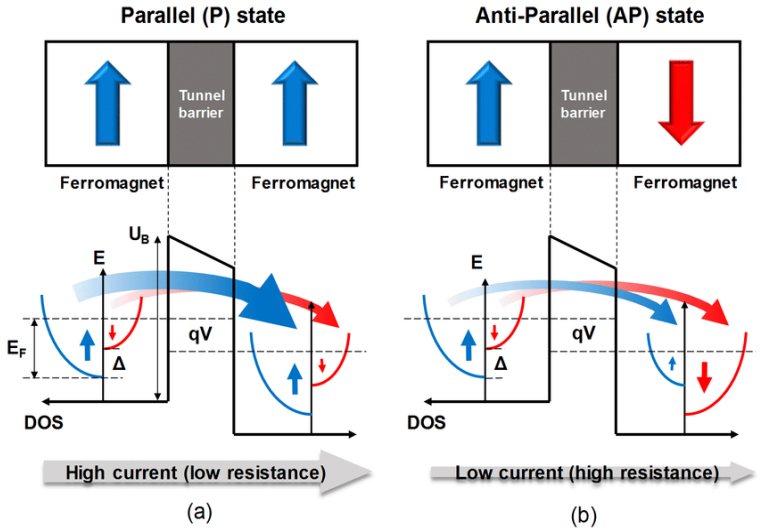


Figure 1.5: **(a)** Tunneling transport for parallel ferromagnetic electrodes (P), **(b)** Tunneling transport for ferromagnetic antiparallel electrodes (AP) [54].

In the TMR model, the angle formed by the electrons' spin moment and the magnetization of the electrode that receives them after they cross the barrier determines the probability of electron transmission over the insulating barrier. According to Figure.1.5, the TMR is described as the difference in resistance between parallel and antiparallel magnetic systems.

- The tunnel current is significant because, in the parallel arrangement, the majority and minority electrons at the Fermi level will find the same density of states on the opposite side of the tunnel barrier.

- In the antiparallel configuration, the up electrons will have a higher density while the down electrons will have a lower density; this results in a lower tunnel current.

One of the most used devices in current technologies (MRAM memories, for example) exploiting the TMR is the Magnetic Tunnel Junction (MTJ). Although the first observations of this effect were made in 1975 by Julliere [55], it was only from 1995, assisted by the work of Moodera et al. on $Co/Al_2O_3/CoFe$ stacks [56], carried out at room temperature and which

have magnetoresistance amplitudes three times higher than the GMR, of the order of 30% to 70% . There are other materials that make up tunnel barriers that have been developed, such as the magneto-crystalline junctions based on magnesium oxide (MgO), exhibiting a magnetoresistance capacity greater than 400% at room temperature. This significant increase in the ferromagnetic resistance capacity of the MgO-based junctions compared to the amorphous junctions based on alumina comes from the crystalline nature of the MgO barriers. Regarding the half-metallic compounds, the tunnel magnetoresistance would theoretically be infinite and the current would be 100% polarized. Heusler alloys have been predicted to be half-metallic materials; these compounds can exhibit a TMR up to 330% at room temperature [57]. It should be noted that the spintronic devices based on spin-polarized electron transport are thought to match the demands for future technologies, including low power consumption since stored data is not volatile and a significant improvement in processing speed [58].

Besides the interest of these phenomena, tunnel junctions are attracting considerable interest for different types of applications in the realm of technology, namely, they allow the production of magnetic field sensors even more sensitive than spin valves due to their greater amplitude of magnetoresistance. These sensors are already used in the latest generation of the hard drive read/write heads but could also be used in position encoders or angular encoders for robotics or as electronic compasses [59].

## 1.9 Spintronics applications developments

With the rapid development of science and technology, the growing demand for high-performance materials with multifunctional properties has increased. Modern technologies require transduction materials, also referred to as "smart materials", which undergo a substantial change of one or several properties in response to changing external conditions. All smart materials are transducer materials because they transform energy into another form. They therefore have many applications, such as a sensor (signal detector), processor (process and store information), magnetic random access memory (MRAM), and read/write heads of hard drive.

### 1.9.1 Magnetic field sensors

Magnetic sensors are implanted in a very large number of technological objects that surround us. For example, a recent car will contain more than thirty magnetic sensors, and you will also find some in a refrigerator, washing machine and even some sports shoes. Magnetic

sensors make it possible to detect and measure a magnetic field created by a magnetic object (magnet or bobbin) or by an electric current (through its radiated magnetic field). They therefore offer many possibilities related to the transmission of information without contact, remote detection, or current measurement.

There are several types of magnetic sensors; some are field sensors (of the Hall effect, GMR and TMR types), and others are flux sensors (i.e., measuring the integral of the field passing through a surface). It is always difficult to compare magnetic sensors, insofar as each has particular advantages. For example, Hall effect sensors are not very sensitive but present the advantage of being absolute and linear on a very wide range of field; they are therefore essential in applications that measure high field values. A second determining aspect is the extension of the magnetic field to be measured. If it is large, as for imaging terrestrial, it is necessary to use flow sensors, which are much more sensitive than field sensors. If the spatial extension becomes small, field sensors must be used. This is why giant magnetoresistance (GMR) sensors derived from spin electronics have been implanted in read heads instead of inductive coils; they can be miniaturized to sizes of a few tens of microns and integrated into CMOS (Complementary Metal Oxide Semiconductor) systems containing signal processing electronics.

These sensors have many applications: reading hard disks, spatial positioning control, position and angle coding, non-contact electrical current measurement, magnetic and medical imaging, etc. (Figure.1.6).

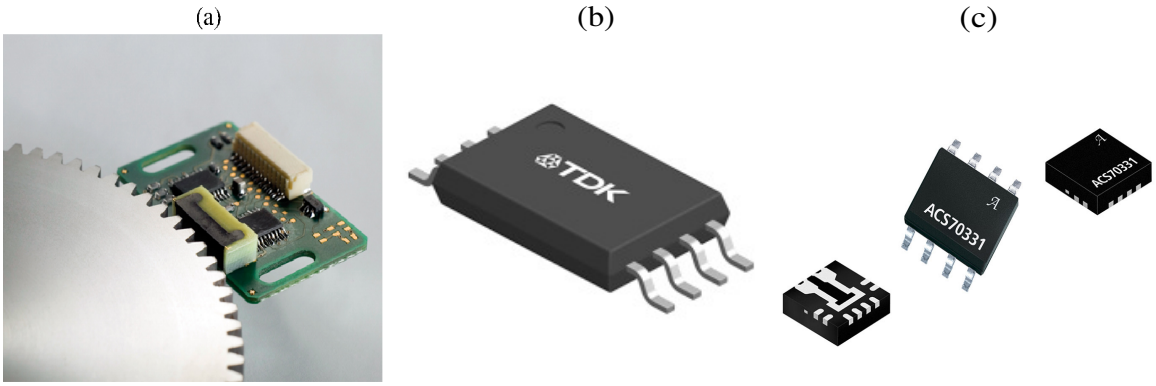


Figure 1.6: **(a)** GMR tooth sensor modules for angle and length measurement, **(b)** TAS series TMR angle sensors, **(c)** GMR current sensors.

### 1.9.2 Magnetic random access memory (MRAM)

Magnetic random access memories are a new type of computer memory that is intuitively very fast, non-volatile, and has almost unlimited endurance. This type of memory is a com-

bination of static random access memory (SRAM) speed (down to 5 ns read/write), dynamic random access memory (DRAM) density, and the non-volatile feature of Flash (retain the information even when the computer is not powered on).

The basic concept of MRAM is to use the magnetization configuration (P/AP) in MTJ for information storage “0” and “1” (binary information). In other words, a low resistance state represents a logic "0", while a high resistance state represents a logic "1". The information written in the bit is read back by measuring the resistance level of the tunnel junction (Figure.1.7).

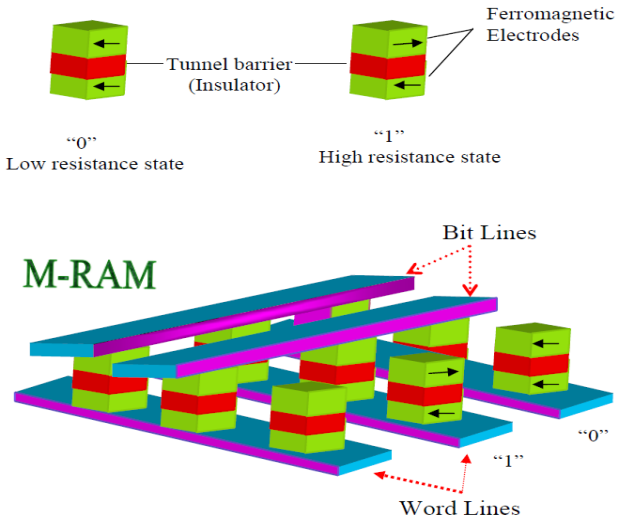


Figure 1.7: Magnetic random access memory architecture.

MRAMs will eliminate, for example, the time required today to load (“boot”) the operating system when switching on current computers. They will also be less energy-intensive than current DRAMs, whose memory must be "refreshed" approximately every thousandths of a second. They will therefore be very interesting for mobile electronics, computers or mobile phones, etc. In recent years, research has led to the invention of an advanced type of MRAM devices, namely, Spin-Transfer Torque MRAM (STT-RAM) and Spin-Orbit Torque MRAM (SOT-MRAM). STT-MRAM enables higher densities, low power consumption, and reduced cost compared to regular (so-called Toggle MRAM) devices. The main advantage of STT-MRAM over Toggle MRAM is the ability to scale the STT-MRAM chips to achieve higher densities at a lower cost. Since SOT-MRAM is a quicker, denser, and far more effective memory technology, it might pose a challenge to STT-MRAM. Figure.1.8 displays a comparison of the STT-RAM and SOT-RAM cell models.

SOT-MRAM devices property switching of the free magnetic layer done by injecting in-plane current in a neighboring SOT layer, in contrast to STT-MRAM, which uses the same

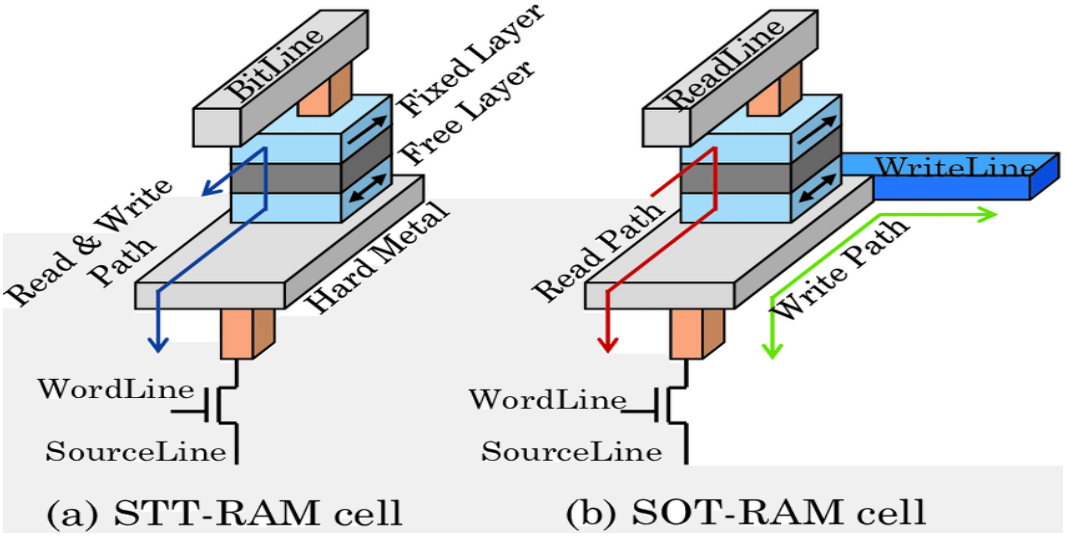


Figure 1.8: MRAM Standard cells **(a)** STT-MRAM **(b)** SOT-MRAM.

channel for both read and write operations and injects current into the magnetic tunnel junction perpendicularly.

### 1.9.3 Read-Write heads of hard drives

A hard disk drive (HDD) is a magnetic rotating disk mass memory used mainly in computers. The hard disk drive was first produced by IBM (International Business Machines) in 1956 and shipped as a component of the IBM 305 Random Access Memory Accounting (RAMAC) system in 1957 (Figure.1.9). In a hard drive, there are platters that are rigid in ro-

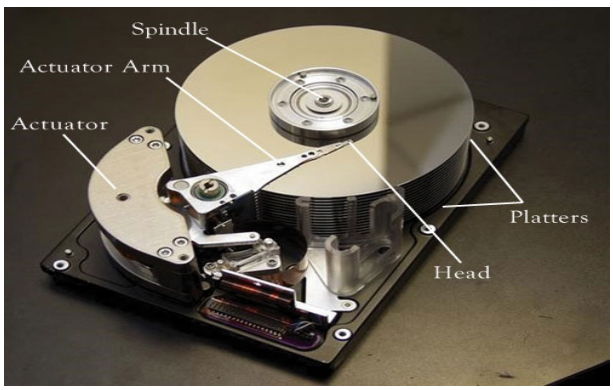


Figure 1.9: Hard drive architecture.

tation. Each platter consists of a disk generally made of aluminum, which has the advantages of being light, easily machined, and paramagnetic. From 1990, new techniques used glass or ceramics, which allowed even smoother surface conditions than those of aluminum. The sides of these platters are covered with a magnetic layer (a cobalt alloy), on which the data is stored. This data is written in binary code (0/1) on the disk thanks to a read/write head,

which uses the GMR/TMR technique (see Figure.1.10). Depending on the electric current passing through it, this head modifies the local magnetic field to write either a 1 or a 0 on the surface of the disc. To read, the same material is used, but in the other direction, the local magnetic field movement creates at the head's terminals an electric potential that depends on the value previously written; one can thus read a 1 or a 0.

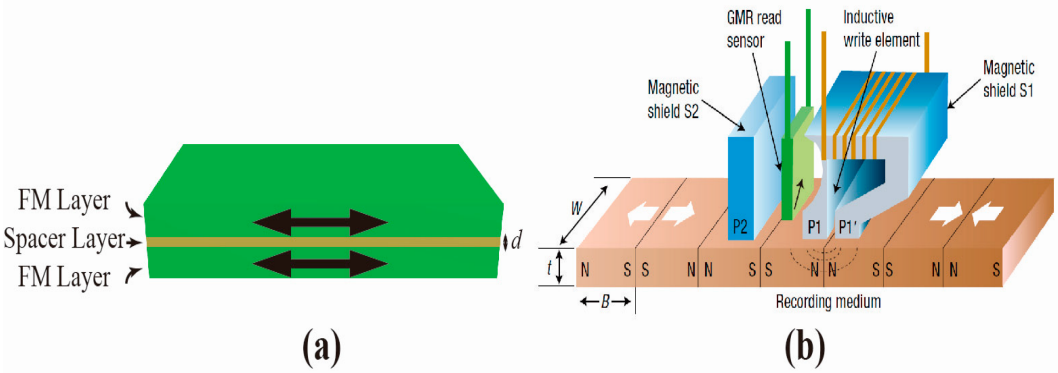


Figure 1.10: **(a)** Schematic of a GMR device, **(b)** GMR read-write head for hard drive [52].

Hard disk drive technology faced several challenges, such as cell size, power consumption, density (around 400GB/in$^2$) and access time (around 9 ms). On the other hand, NAND flash memories have developed a significant presence in the non-volatile memory (NVM) market and are now attempting to move into the computer storage market in the form of solid state drives (SSDs). This kind of flash memory offers lower power consumption, higher density (around 400 GB/chip), faster read access time (around 200 $\mu$s) and better mechanical reliability than HDDs; however, the cost per gigabyte (GB) for flash memories is nearly 10 that of magnetic storage [60].

# BIBLIOGRAPHY


[1] A. Yanase and K. Siratori, "Band structure in the high temperature phase of $Fe_3O_4$," *Journal of the Physical Society of Japan*, vol. 53, no. 1, pp. 312–317, 1984.

[2] Z. Zhang and S. Satpathy, "Electron states, magnetism, and the verwey transition in magnetite," *Physical Review B*, vol. 44, no. 24, p. 13319, 1991.

[3] H. C. Kandpal, G. H. Fecher, and C. Felser, "Calculated electronic and magnetic properties of the half-metallic, transition metal based heusler compounds," *Journal of Physics D: Applied Physics*, vol. 40, no. 6, p. 1507, 2007.

[4] R. De Groot, F. Mueller, P. v. van Engen, and K. Buschow, "New class of materials: half-metallic ferromagnets," *Physical review letters*, vol. 50, no. 25, p. 2024, 1983.

[5] S. Trudel, O. Gaier, J. Hamrle, and B. Hillebrands, "Magnetic anisotropy, exchange and damping in cobalt-based full-Heusler compounds: an experimental review," *Journal of Physics D: Applied Physics*, vol. 43, no. 19, p. 193001, 2010.

[6] F. Heusler, W. Starck, and E. Haupt, "Magnetisch-chemische studien," *Verh. Dtsch. Phys. Ges*, vol. 5, pp. 219–232, 1903.

[7] A. J. Bradley and J. W. Rodgers, "The crystal structure of the heusler alloys," *Proceedings of the Royal Society of London. Series A, Containing Papers of a Mathematical and Physical Character*, vol. 144, no. 852, pp. 340–359, 1934.

[8] S. Sakurada and N. Shutoh, "Effect of Ti substitution on the thermoelectric properties of (Zr, Hf) NiSn half-Heusler compounds," *Applied Physics Letters*, vol. 86, no. 8, p. 082105, 2005.

[9] P. Webster, "Magnetic and chemical order in heusler alloys containing cobalt and manganese," *Journal of Physics and Chemistry of Solids*, vol. 32, no. 6, pp. 1221–1231, 1971.

[10] H. Van den Berg, M. Gijs, P. Grünberg, T. Rasing, and K. Röll, *Magnetic multilayers and giant magnetoresistance: fundamentals and industrial applications*, vol. 37. Springer Science & Business Media, 2000.

[11] H. ZENASNI, *Etude théorique des propriétés magnétiques, électroniques et structurales des alliages Heusler*. PhD thesis, 2013.

[12] H.-U. Schuster, H.-W. Hinterkeuser, W. Schäfer, and G. Will, "Notizen: Neutronenbeugungsuntersuchungen an den Phasen LiAlSi und LiAlGe. / Investigations on Neutron Diffraction of the Phases LiAlSi and LiAlGe," *Zeitschrift für Naturforschung B*, vol. 31, no. 11, pp. 1540–1541, 1976.

[13] C. P. Sebastian, S. Rayaprol, and R. Pöttgen, "119Sn Mössbauer spectroscopy and specific heat studies of the stannides RETSn (RE=Gd–Er and T=Cu,Ag)," *Solid State Communications*, vol. 140, no. 6, pp. 276–280, 2006.

[14] P. Grünberg, R. Schreiber, Y. Pang, M. Brodsky, and H. Sowers, "Layered magnetic structures: evidence for antiferromagnetic coupling of Fe layers across Cr interlayers," *Physical review letters*, vol. 57, no. 19, p. 2442, 1986.

[15] S. S. P. Parkin, N. More, and K. P. Roche, "Oscillations in exchange coupling and magnetoresistance in metallic superlattice structures: Co/Ru, Co/Cr, and Fe/Cr," *Phys. Rev. Lett.*, vol. 64, pp. 2304–2307, May 1990.

[16] N. Mott, "A discussion of the transition metals on the basis of quantum mechanics," *Proceedings of the Physical Society*, vol. 47, no. 4, p. 571, 1935.

[17] T. Malsawmtluanga and R. Thapa, "Ground state study of half-metallic ferromagnetism in the half-Heusler compound Gekca using density functional theory," in *AIP Conference Proceedings*, vol. 1536, pp. 1047–1048, American Institute of Physics, 2013.

[18] K. Belkacem, Y. Zaoui, S. Amari, L. Beldi, and B. Bouhafs, "First-Principles Study of the New Half-Metallic Ferromagnetic Quaternary-Heusler Alloys NaXNO (X= Ca, Sr, Ba)," in *Spin*, vol. 10, p. 2050022, World Scientific, 2020.

[19] S. De Souza, R. Saxena, W. Shreiner, and F. Zawislak, "Magnetic hyperfine fields in Heusler alloys CoYZ (Y= Ti, Zr; Z= Al, Ga, Sn)," *Hyperfine Interactions*, vol. 34, no. 1-4, pp. 431–434, 1987.

[20] S. Benatmane and B. Bouhafs, "Investigation of new $d^0$ half-metallic full-heusler alloys $N_2BaX$ (X= Rb, Cs, Ca and Sr) using first-principle calculations," *Computational Condensed Matter*, vol. 19, p. e00371, 2019.

[21] J. Chen, G. Gao, K. Yao, and M. Song, "Half-metallic ferromagnetism in the half-Heusler compounds GeKCa and SnKCa from first-principles calculations," *Journal of alloys and compounds*, vol. 509, no. 42, pp. 10172–10178, 2011.

[22] L. Beldi, Y. Zaoui, K. Obodo, H. Bendaoud, and B. Bouhafs, "$d^0$ Half-metallic ferromagnetism in GeNaZ (Z= Ca, Sr, and Ba) ternary half-heusler alloys: an ab initio investigation," *Journal of Superconductivity and Novel Magnetism*, vol. 33, no. 10, pp. 3121–3132, 2020.

[23] X.-P. Wei, Y.-D. Chu, X.-W. Sun, J.-B. Deng, and Y.-Z. Xing, "Stability, electronic, magnetic and pressure effect of half-Heusler alloys CNaCa and SiNaCa: A first-principles study," *Superlattices and Microstructures*, vol. 74, pp. 70–77, 2014.

[24] H. Rozale, A. Amar, A. Lakdja, A. Moukadem, and A. Chahed, "Half-metallicity in the half-Heusler RbSrC, RbSrSi and RbSrGe compounds," *Journal of magnetism and magnetic materials*, vol. 336, pp. 83–87, 2013.

[25] R. Umamaheswari, M. Yogeswari, and G. Kalpana, "Ab-initio investigation of half-metallic ferromagnetism in half-Heusler compounds XYZ (X= Li, Na, K and Rb; Y= Mg, Ca, Sr and Ba; Z= B, Al and Ga)," *Journal of magnetism and magnetic materials*, vol. 350, pp. 167–173, 2014.

[26] J. Du, S. Dong, X. Wang, H. Zhao, L. Wang, and L. Feng, "First-principles study on the half-metallic properties of the $d^0$ quaternary Heusler compounds: KCaCBr and KCaCI," *AIP Advances*, vol. 6, no. 10, p. 105308, 2016.

[27] J. Du, S. Dong, X. Wang, H. Rozale, H. Zhao, L. Wang, and L. Feng, "Half-metallic ferromagnetism in KCaNX (X= O, S, and Se) quaternary Heusler compounds: A first-principles study," *Superlattices and Microstructures*, vol. 105, pp. 39–47, 2017.

[28] P. Villars and K. Cenzual, "Landolt-Börnstein - Group III Condensed Matter, Volume 43A10," *Landolt Börnstein*, vol. 43A1, Jan. 2011.

[29] H. Nowotny and W. Sibert, "Ternäre Valenzverbindungen in den Systemen Kupfer (Silber)-Arsen (Antimon, Wismut)-Magnesium," *International Journal of Materials Research*, vol. 33, no. 12, pp. 391–394, 1941.

[30] J. Nuss and M. Jansen, "Zur Abgrenzung der PbFCl-und $Cu_2Sb$-Strukturfamilien: Neubestimmung und Verfeinerung der Kristallstrukturen von CuMgSb, $Cu_2Sb$ und CuMgAs," *Zeitschrift für anorganische und allgemeine Chemie*, vol. 628, no. 5, pp. 1152–1157, 2002.

[31] T. Jin and Y. Jung, "Classifying intermetallic tetragonal phase of all-d-metal Heusler alloys for catalysis applications," *Topics in Catalysis*, vol. 65, no. 1-4, pp. 208–214, 2022.

[32] F. H. Verh, "Ueber magnetische Manganlegierungen," *Verh. Dtsch. Phys. Ges.*, vol. 5, p. 219, 1903.

[33] T. Graf, S. S. Parkin, and C. Felser, "Heusler compounds—A material class with exceptional properties," *IEEE Transactions on Magnetics*, vol. 47, no. 2, pp. 367–373, 2010.

[34] J. Drews, U. Eberz, and H.-U. Schuster, "Optische Untersuchungen an farbigen Intermetallischen phasen," *Journal of the Less Common Metals*, vol. 116, no. 1, pp. 271–278, 1986.

[35] G. Bacon and J. Plant, "Chemical ordering in Heusler alloys with the general formula $A_2BC$ or ABC," *Journal of Physics F: Metal Physics*, vol. 1, no. 4, p. 524, 1971.

[36] K. Watanabe, "Magetic Properties of Clb-Type Mn Base Compounds," *Transactions of the Japan Institute of Metals*, vol. 17, no. 4, pp. 220–226, 1976.

[37] M. HEHN, F. MONTAIGNE, and A. SCHUHL, "Magnétorésistance géante et électronique de spin," *Techniques de l'ingénieur. Electronique*, vol. 3, no. E2135, pp. 1–15, 2002.

[38] Z. Gercsi and K. Hono, "Ab initio predictions for the effect of disorder and quarternary alloying on the half-metallic properties of selected $Co_2Fe$-based Heusler alloys," *Journal of Physics: Condensed Matter*, vol. 19, no. 32, p. 326216, 2007.

[39] X. Xu, Y. Wang, D. Zhang, and Y. Jiang, "Electronic structures and the spin polarization of Heusler alloy $Co_2FeAl$ surface," in *Journal of Physics: Conference Series*, vol. 263, p. 012016, IOP Publishing, 2011.

[40] J. Bardeen and W. H. Brattain, "The Transistor, A Semi-Conductor Triode," *Phys. Rev.*, vol. 74, pp. 230–231, Jul 1948.

[41] J. S. Kilby, "Miniaturized electronic circuits," *USP3, 138,743*, 1964.

[42] I. Žutić, J. Fabian, and S. D. Sarma, "Spintronics: Fundamentals and applications," *Reviews of modern physics*, vol. 76, no. 2, p. 323, 2004.

[43] G. A. Prinz, "Magnetoelectronics," *Science*, vol. 282, no. 5394, pp. 1660–1663, 1998.

[44] G. A. Prinz, "Magnetoelectronics applications," *Journal of magnetism and magnetic materials*, vol. 200, no. 1-3, pp. 57–68, 1999.

[45] M. N. Baibich, J. M. Broto, A. Fert, F. N. Van Dau, F. Petroff, P. Etienne, G. Creuzet, A. Friederich, and J. Chazelas, "Giant magnetoresistance of (001) Fe/(001) Cr magnetic superlattices," *Physical review letters*, vol. 61, no. 21, p. 2472, 1988.

[46] G. Binasch, P. Grünberg, F. Saurenbach, and W. Zinn, "Enhanced magnetoresistance in layered magnetic structures with antiferromagnetic interlayer exchange," *Physical review B*, vol. 39, no. 7, p. 4828, 1989.

[47] N. F. Mott, "The electrical conductivity of transition metals," *Proceedings of the Royal Society of London. Series A-Mathematical and Physical Sciences*, vol. 153, no. 880, pp. 699–717, 1936.

[48] A. Fert and I. A. Campbell, "Two-Current Conduction in Nickel," *Phys. Rev. Lett.*, vol. 21, pp. 1190–1192, Oct 1968.

[49] B. Loegel and F. Gautier, "Origine de la resistivite dans le cobalt et ses alliages dilues," *Journal of Physics and Chemistry of Solids*, vol. 32, no. 12, pp. 2723–2735, 1971.

[50] A. Fert, "Nobel lecture: Origin, development, and future of spintronics," *Reviews of modern physics*, vol. 80, no. 4, p. 1517, 2008.

[51] P. A. Grünberg, "Nobel Lecture: From spin waves to giant magnetoresistance and beyond," *Reviews of Modern Physics*, vol. 80, no. 4, p. 1531, 2008.

[52] C. Chappert, A. Fert, and F. V. Dau, "The emergence of spin electronics in data storage.," *Nature materials*, vol. 6 11, pp. 813–23, 2007.

[53] M. Kerekes, R. Sousa, I. Prejbeanu, O. Redon, U. Ebels, C. Baraduc, B. Dieny, J. Nozières, P. Freitas, and P. Xavier, "Dynamic heating in submicron size magnetic tunnel junctions with exchange biased storage layer," *Journal of applied physics*, vol. 97, no. 10, p. 10P501, 2005.

[54] X. Fong, Y. Kim, K. Yogendra, D. Fan, A. Sengupta, A. Raghunathan, and K. Roy, "Spin-transfer torque devices for logic and memory: Prospects and perspectives," *IEEE Transactions on Computer-Aided Design of Integrated Circuits and Systems*, vol. 35, no. 1, pp. 1–22, 2015.

[55] M. Julliere, "Tunneling between ferromagnetic films," *Physics letters A*, vol. 54, no. 3, pp. 225–226, 1975.

[56] J. Moodera, L. Kinder, J. Nowak, P. LeClair, and R. Meservey, "Geometrically enhanced magnetoresistance in ferromagnet–insulator–ferromagnet tunnel junctions," *Applied physics letters*, vol. 69, no. 5, pp. 708–710, 1996.

[57] W. Wang, H. Sukegawa, R. Shan, S. Mitani, and K. Inomata, "Giant tunneling magnetoresistance up to 330% at room temperature in sputter deposited $Co_2FeAl$/MgO/CoFe magnetic tunnel junctions," *Applied Physics Letters*, vol. 95, no. 18, p. 182502, 2009.

[58] C. Felser, G. H. Fecher, and B. Balke, "Spintronics: a challenge for materials science and solid-state chemistry," *Angewandte Chemie International Edition*, vol. 46, no. 5, pp. 668–699, 2007.

[59] C. BOUROUIS, *Etude des propriétés structurales, électroniques et magnétiques des semiconducteurs magnétiques dilués (DMS):* $Cd_{1-x}Fe_xS$. PhD thesis, 2016.

[60] M. H. Kryder and C. S. Kim, "After hard drives—What comes next?," *IEEE Transactions on Magnetics*, vol. 45, no. 10, pp. 3406–3413, 2009.

CHAPTER 2

# DENSITY FUNCTIONAL THEORY (DFT)

## 2.1 Introduction

The discovery of X-ray diffraction at the start of the $XX^{th}$ century was the first step toward a good description of the physical characteristics of the solid state. This one then made it possible to analyze the atomic positions in the crystals. Since then, increasingly sophisticated experimental techniques have facilitated the observation of the solid phases of elements.

In parallel with these experimental advances, theories have been developed that allow a good description of the solid phases and their electronic structure, such as ab-initio calculation models, which are directly derived from the Schrödinger equation and which allow access to all the physico-chemical properties of a system. This is well known since the development of quantum mechanics. To understand these physical properties of the studied systems, such as the structural, electronic, magnetic, optical, mechanical or thermal properties of solids, it is necessary to study the physical environment in which charge carriers (electrons) move. This implies knowing how the atoms are arranged inside the solid, and to predict the performance of electrical components, it is also necessary to study the energy structure corresponding to this physical environment.

Because each particle interacts with all the other particles, it is highly challenging to investigate these ground state characteristics of N-body system in a crystal theoretically. As a result, Schrödinger's equation mathematically becomes unsolvable. According to Dirac (1929), advancement hinges on the creation of approximation methods that are sufficiently precise. The density functional theory (DFT), which is founded on the Hohenberg-Kohn theorems, was developed in this context.

In the literature, the first exploitation of ab-initio calculations was in 1985 by R. Car and

M. Parrinello [1], it was for the feasibility of ab-initio molecular dynamics. Since that date, this method has borne very good fruit and spread in many directions of research. Simulation on a computer offers a qualitative way to study various properties of the matter. It was able to give enough muscle to the computer; this gives the simulator a chance to build the model of a real system and explore its behavior.

Moreover, all ab-initio methods have benefited in recent years from the availability of increasingly powerful computers. This has contributed to the current success of these calculations for real material systems in interesting situations and with sufficient accuracy. Therefore, there can be meaningful detailed comparisons with experimental measurements.

## 2.2 Schrödinger equation of a solid

The Schrödinger equation is the basic equation of solid state physics. The energy and related wave function of a particular system can be found using this equation. Furthermore, the charge density, a basic parameter of the system, can be obtained from this wave function.

Here is an expression of the time-independent Schrödinger equation:

$$H\Psi = E\Psi. \tag{2.1}$$

Where:

H: Hamiltonian operator.

$\Psi$: wave function.

E: energy of the system "eigenvalue" .

For a system of M nuclei with charge $Z_k e$ and mass $M_k$, placed at positions $\vec{R}_k$ ($k = 1, \cdots, M$), and with N electrons of positions $\vec{r}_i$ ($i = 1, \cdots, N$), charge (-e) and mass $m_e$, the Hamiltonian is written [2]:

$$H = T_e + T_n + V_{e\text{–}e} + V_{n\text{–}n} + V_{e\text{–}n}. \tag{2.2}$$

Where:

$T_e = -\sum_{i=1}^{N} \frac{\hbar^2}{2m_e} \nabla_i^2$ : electrons kinetic energy.

$T_n = -\sum_{k=1}^{M} \frac{\hbar^2}{2M_n} \nabla_k^2$ : nuclei kinetic energy.

$V_{e\text{–}e} = \frac{1}{2} \sum_{i_1 \neq i_2 = 1}^{N} \frac{1}{4\pi\epsilon_0} \frac{e^2}{|\vec{r}_{i1} - \vec{r}_{i2}|}$ : interaction energy between the electrons.

$V_{n\text{–}n} = \frac{1}{2} \sum_{k_1 \neq k_2 = 1}^{M} \frac{1}{4\pi\epsilon_0} \frac{Z_{k1} Z_{k2} e^2}{|\vec{R}_{k1} - \vec{R}_{k2}|}$ : interaction energy between the nuclei.

$V_{n-n} = -\sum_{k_1}^{M} \sum_{i=1}^{N} \frac{1}{4\pi\epsilon_0} \frac{Z_k e^2}{|\vec{R}_k - \vec{r}_i|}$ : interaction energy between electrons and nuclei.

In this system, $\Psi$ is a function of $3(M + N)$ continuous variables (the coordinates x, y, z of each particle) and $(M + N)$ discrete variables (the spins).

Accordingly, solving the Schrödinger equation with all these variables is not possible. Hence, What is the solution to the N-body problem?, and how can the Schrödinger equation be used to determine the ground state of the system?

Several approaches are used for this, including the Born-Oppenheimer approximation, the Hartree approximation, the Hartree-Fock approximation, and finally the density functional theory (DFT).

## 2.3 Born-Oppenheimer approximation

Born-Oppenheimer (1927) asserts that treating a system's electrons and nuclei independently is the only method for obtaining a simplification that enables the Schrödinger equation to be solved.

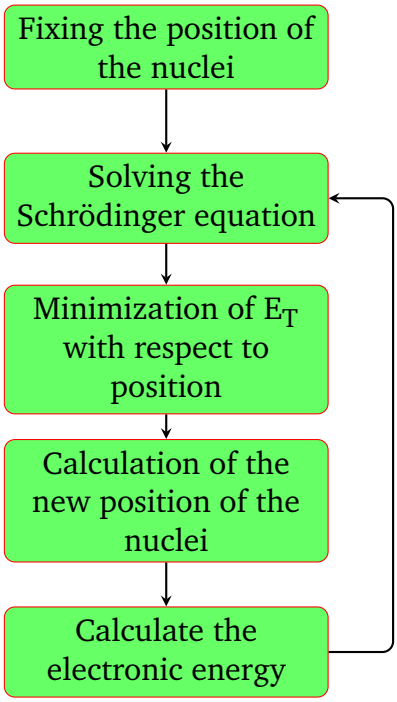


Figure 2.1: Algorithm implementation of Born-Oppenheimer approximation.

In comparison to the electrons, the nuclei are extremely hefty (1840 times for the lightest nucleus), hence they move much faster than the nuclei, and the electrons "immediately" go into their new places prior to the nuclei being displaced. The result of this approximation is

a Hamiltonian for which the electrons move in an external potential that the nuclei create.

The Hamiltonian can be defined as:

$$H = T_e + V_{e-e} + V_{e-n}. \tag{2.3}$$

The resolution by Born-Oppenheimer can be translated by the flowchart illustrated in Figure.2.1.

This approximation significantly reduces the degree of complexity, but the new system wave function $\Psi$ depends on N bodies, while this approach is followed by additional approximations that are required to be able to effectively solve this equation.

## 2.4 Hartree approximation

Despite the Born-Oppenheimer approximation, which only takes electrons into consideration. We are again faced with the N-body problem because of the electron-electron interaction term; hence, it becomes almost intuitive to look for a method to solve this complex problem on the basis of the mono-electron case.

In 1927, Dauglas Hartree [3] proposed a method for calculating the wave functions and the approximate energies of ions and atoms. The fundamental idea of this approach is to consider that electrons move independently to each other (the free electron hypothesis).

Thus, the Hamiltonian can be written as follows:

$$H = \sum_{i=1}^{N} h(i), \tag{2.4}$$

Where h is the mono-electron Hamiltonian:

$$h(i) = T_e + V_i(r_i) + V_H(r_i). \tag{2.5}$$

Where:

$V_i(r_i)$ : electron's potential energy (i) in the field of all nuclei (k).

$V_H(r_i)$ : Hartree's effective field.

In other way, the mono-electron wave function is written as follows:

$$\Psi_e(r_1, r_2, ...r_N) = \prod_{i=1}^{N} \Psi_i(r_i). \tag{2.6}$$

A more reasonable wave function should be anti-symmetric when exchanging two electrons. In addition, this function does not respect the Pauli exclusion principle. For this, it is necessary to incorporate the spin in the wave function, which leads to Hartree-Fock approximation.

## 2.5 Hartree-Fock approximation

The electronic system in the Hartree approximation is not entirely defined. First, the Pauli principle is not verified, but in this approximation the electrons obey the Pauli exclusion principle (anti-symmetric), which states that a negative sign must occur in the wave function after two electrons are exchanged:

$$\Psi(x_1, x_2) = -\Psi(x_2, x_1). \tag{2.7}$$

It was demonstrated by Hartree and Fock that this concept is upheld if the wave function is expressed as a Slater determinant of the N function $\Psi$.

The following is how this determinant is expressed [4]:

$$\Psi^s(r_i) = \frac{1}{\sqrt{N!}} \begin{vmatrix} \Phi_1(r_1) & \Phi_2(r_1) & \cdots & \Phi_n(r_1) \\ \Phi_1(r_2) & \Phi_2(r_2) & \cdots & \Phi_n(r_2) \\ \vdots & \vdots & \ddots & \vdots \\ \Phi_1(r_n) & \Phi_2(r_n) & \cdots & \Phi_n(r_n) \end{vmatrix} \tag{2.8}$$

Mono-electron wave functions are included in this determinant as a product of Hartree's wave functions. The function that fulfills the Hartree-Fock equations is written as follows [5]:

$$\left[-\frac{\hbar^2}{2m_e}\nabla_i^2 + V_i(r_i) + V_H(r_i)\right]\Psi_i(r_i) - \sum \int \frac{d^3r}{|r - r'|}\Psi_j^*(r').\Psi_j(r')]\Psi_j(r) = \epsilon_i\Psi_i(r). \tag{2.9}$$

The Hartree-Fock equations are different from the Hartree equations by the exchange term, which is the final term before the equality.

Despite the exchange term, this approach ignores the correlation that exists between electrons; the inclusion of this correlation is done by the density functional theory (DFT).

## 2.6 Density functional theory (DFT)

This theory's basic premise is to express any other quantity as a function of the ground state electron density $\rho(r)$, which is the key variable. The basis of this theory is a variational principle that requires the total energy to be a single, distinct functional of the density and to be at its lowest for the ground state density. The optimal process for performing this theory is the Kohn-Sham method; they treated the N-body problem using one-particle Schrödinger equations called the Kohn-Sham equations [6], solving these equations normally leads to the energy $E(\rho)$ and the density $\rho(r)$ of the ground state. The non-classical contribution to the

functional $E(\rho)$ is known as the exchange and correlation energy $E_{xc}(\rho)$, and its derivative with respect to $\rho$, which represents the exchange and correlation potential $V_{xc}(\rho)$.

### 2.6.1 Hohenberg and Kohn theorems

In 1964, Hohenberg and Kohn created a method [7] that extends the density functional theory proposed by Thomas-Fermi. It applies to any system with N interacting particles evolving in an external potential. It is based on two theorems:

**Theorem 1** *For any system of interacting particles in an external potential, this potential is uniquely determined, up to a constant, using the particles density in the ground state.*

Put otherwise, the electronic density of the ground state $\rho^{gro}$ and the potential that the electrons experience are in a one to one relationship. This suggests that each feature of the system can be fully ascertained (the Hamiltonian can be constructed) if we know the basic electron density.

**Theorem 2** *For any external potential, there is a functional* $E(\rho)$ *that represents the energy as a function of the electron density* $\rho$*. This functional is minimized by the accurate electron density of the ground state* $\rho^{gro}$.

Along with proving that the energy of the system can be represented as a functional of the electron density, this second theorem also demonstrates that the energy complies with the variational principle. Hence, we have:

$$E_v(\rho) = F_{HK}[\rho] + \int v(r)\rho(r)dr \tag{2.10}$$

$$F_{HK}[\rho] = T[\rho] + V_{ee}[\rho] \tag{2.11}$$

Where:

$F_{HK}[\rho]$ is the functional of Hohenberg and Kohn.

The functional $F_{HK}$ introduced depends on a density associated with the ground state of a Hamiltonian, which contains a local exterior potential; this means that $F_{HK}$ depends on the potential. To eliminate this dependency and find a functional Universal $F[\rho]$ (independent of the potential), Levy and Lieb [8] proposed the method constrained search. The sum of the kinetic and repulsion energies yields to a universal functional.

$$F[\rho] = \min_{\varphi \to \rho} \langle \varphi \,|T + V_e|\, \varphi \rangle \tag{2.12}$$

Using the definition of F[$\rho$], it can be written:

$$E(\rho) = F[\rho] + \int v(r)\rho(r)dr \tag{2.13}$$

The Hohenberg and Kohn theorems demonstrate that the functional F[$\rho$] is universal and exists for any system since it is independent of the external potential. However, the difficulty is still not removed; the lack of expression analysis of this functional F[$\rho$] for a limit system of N electrons makes the application of this approach quite difficult. Further approximations are necessary, leading to Kohn and Sham equations, which allow an effective exploitation of the Hohenberg-Kohn theorems.

## 2.7 Kohn and Sham equations

In principle the Euler equation can be used to determine the ground state's energy:

$$\frac{\delta F[\rho]}{\delta \rho} + v(r) = \mu \tag{2.14}$$

Where:

$\mu$: the chemical potential.

However, the precise form of the functional F[$\rho$] is unknown.

$$F[\rho] = T[\rho] + V_{ee}[\rho] \tag{2.15}$$

It is possible to reduce a system of N interacting electrons to a fictitious system of N electrons that are subject to effective potentials ($V_{eff}$) but do not interact with one another thanks to the Kohn and Sham theorem [6]. It should be noted that the density and total energy of this system are identical to those of the real system. Kohn and Sham showed that the true density is given by a self-consistent resolution of the set of one-particle equations with the Schrödinger type, also called Kohn-Sham equations, which are given as follows:

$$\left[-\frac{\hbar^2}{2m_e}\nabla_i^2 + V_{eff}\right]\Psi_i(r) = \epsilon_i \Psi_i(r). \tag{2.16}$$

Where:

$V_{eff}$ is the effective potential, which can be expressed as:

$$V_{eff} = V_{ion}(r) + V_H(r) + V_{xc}(r) \tag{2.17}$$

Where:

$V_{ion}(r)$: ion potential which is a real local function of r.

$V_H(r)$: Haretree-Fock potential.

$V_{xc}$: exchange and correlation potential.

The Kohen-Sham equations are perhaps the most important in the density functional theory as they simplify the analysis of the interacting electron issue to the study of an independent electrons system immersed in an effective potential, which contains all possible interactions between electrons [8].

The energy is written as a function of the Kohn-Sham orbitals $\psi_i$ in the form:

$$E[\psi_i] = 2\sum_i \int \psi_i(-\frac{\hbar^2}{2m})\psi_i d^3r + \int V_{ion}(r)\rho(r)d^3r + \frac{e^2}{2}\int \frac{\rho(r)\rho(r')}{|r-r'|}d^3r d^3r' + E_{xc}[\rho(r)] + E_{ion}[R_I] \tag{2.18}$$

With: $\rho = \sum_i^N |\psi_i(r)|^2$

## 2.8 Exchange and correlation potential

If the exchange and correlation potential is known, the density functional theory gives accurate results, but the exact expression of this potential still remains unknown, and we use only approximate expressions. Much effort has gone into the search for the expression of this term, and several approximate forms have been proposed.

Local Density Approximation (LDA) [6, 9] or Local Spin Density Approximation (LSDA) and the Generalized Gradient Approximation (GGA) are the most practical approximations.

## 2.9 Local density approximation (LDA)

The only unidentified functional in the preceding equations is that of exchange and correlation. The simplest way to obtain this contribution is to use the local density approximation (LDA) approach [6].

The assumption that underlies this approximation is that the terms of exchange-correlation are only dependent on the local value $\rho(r)$, i.e., it treats a non-homogeneous system as being locally homogeneous, which is equivalent to neglecting the effects of density variations.

The exchange-correlation energy is given in the following relationship:

$$E_{xc}^{LDA}(\rho) = \int \rho(r)\epsilon_{xc}[\rho(r)]\, d^3r. \tag{2.19}$$

Where:

$\epsilon_{xc}$ is the exchange and correlation energy of a uniform electron gas; it is divided into two terms:

$$\epsilon_{xc}(\rho) = \epsilon_x(\rho) + \epsilon_c(\rho). \tag{2.20}$$

Where :

$\epsilon_x(\rho)$: exchange energy.

$\epsilon_c(\rho)$: correlation energy.

For polarized (magnetic) spin systems, the local spin density approximation (LSDA) must be included to this approximation, for which the exchange and correlation energy becomes as follows:

$$E_{xc}^{LDA}(\rho) = \int \rho(r)\epsilon_{xc}\left[\rho_\uparrow(r), \rho_\downarrow(r)\right] d^3r. \tag{2.21}$$

Hence, the potential of the exchange and correlation can be expressed as follows:

$$\upsilon_{xc}^{LDA}(r) = \frac{\delta E_{xc}[\rho]}{\delta\rho} = \varepsilon_{xx}(\rho) + \frac{\delta\varepsilon_{xc}[\rho(r)]}{\delta\rho}\rho(r) \tag{2.22}$$

The magnitude $\epsilon_{xc}$ can be constant, but there are parameterization procedures to determine it, such as those of Kohn-Sham[6], Perdew and Wang[9] and Hedin and Lundqvist[11].

## 2.10 Generalized gradient approximation (GGA)

The density in a real system is spatially non-homogeneous, but in the LDA and LSDA approaches, we use the density at the point r, and therefore it will be more convenient to introduce a correction to this approximation considering functions of exchange and correlation depend not only on the density at each point but also on its gradient. Therefore, the exchange and correlation energy is written as follows:

$$E_{xc}^{GGA}(\rho) = \int \rho(r)F\left[\rho(r), \nabla\rho(r)\right] d^3r \tag{2.23}$$

For a polarized spin system, it is written as:

$$E_{xc}^{GGA}(\rho) = \int \rho(r)F\left[\rho_\uparrow(r), \rho_\downarrow, \nabla\rho_\uparrow(r), \nabla\rho_\downarrow(r)\right] d^3r \tag{2.24}$$

$F[\rho(r), \nabla\rho(r)]$: being the correlation and exchange function that is reliant on the electron density and its gradient. The parameterizations used for the GGA approximation are different, among them those of Perdew et al. (1992) [9] and Perdew et al. (1996) [10].

## 2.11 Becke and Johnson modified potential (mBJ)

In general, the GGA and LDA approximations work very well for many systems. However, they fail to predict well certain electronic properties, such as the energy gap, which is under estimated, especially when dealing with highly correlated systems. Becke and Johnson [12] have developed a method based on the method of the optimized effective potential (OEP), which is a very computationally demanding method but which considerably improves the value of the energy gap. The generalized gradient approximation (GGA) or the local density approximation (LDA) correlation is used in conjunction with the exchange potential of Becke Roussel (BJ). Tran and Blaha [13, 14] modified the BJ (mBJ) function, which further improved the energy gaps. The mBJ potential can be defined as [12]:

$$V_{x,\sigma}^{mBJ}(r) = cV^{BR}(r) + (3c-2)\frac{1}{\pi}\sqrt{\frac{12}{5}}\sqrt{\frac{2t_\sigma(r)}{\rho_\sigma(r)}} \tag{2.25}$$

Where:

$\rho_\sigma(r)$: electronic density.

$t_\sigma(r)$: kinetic energy density.

$V^{BR}(r)$: Becke-Roussel potential.

Tran and Blaha propose to determine c for crystalline materials by the following empirical relationship:

$$c = \alpha + \beta\left(\frac{1}{V_{cell}}\int_{V_{cell}}\frac{\bigtriangledown\rho(r')}{\rho(r')}d^3r'\right)^{1/2} \tag{2.26}$$

Where:

$\alpha$ and $\beta$ are parameters adjusted according to experimental values.

$V_{cell}$: volume of the unit cell.

The original BJ potential is replicated for c = 1. It has been discovered that for many solids, the gap energy grows monotonically with respect to **c** when **c** is varied for a given material [13]. In particular, for solids with small gaps, $c_{opt}$ (the value of **c** that leads to perfect agreement with the experiment) ranges from 1.1 to 1.3, while for solids with a larger gap, $c_{opt}$ is larger (its value ranges from 1.4 to 1.7) [15].

## 2.12 GGA + U approximation

For systems with strongly localized d or f orbitals, the effective intra-site Coulomb repulsion between localized electrons, represented by U, the Hubbard term, is strong compared

to the bandwidth. The LDA method is then insufficient, and intra-atomic correlations must be taken into account. Mott Hubbard insulators such as compounds of transition metals of the end of the 3d series, rare earths, or actinides are indeed obtained metallic in LDA. This erroneous description of systems with strong correlation comes from the fact that in the LDA method, the charge density is defined by an occupation averaged over all orbitals with the same orbital quantum number **l**. The effective mono-electronic potential, which is a functional of the charge density, is therefore identical for all orbitals with the same value of **l**. This is in contradiction with Hund's second rule associated with orbital polarization and responsible for local moments. A method known as the DFT + U has been used to introduce the strong intra-site Coulombic screened interactions between d electrons, which combines the DFT method with Hubbard Hamiltonian $\hat{H}_U$ [16, 17]. Therefore, we employed a version of basic DFT + U that was based on a Hamiltonian of the following form and was suggested by Dudarev et al. [18]:

$$\hat{H}_U = \frac{U}{2} \sum_{m,m',\sigma} \hat{n}_{m,\sigma}\hat{n}_{m',-\sigma} + \frac{U-J}{2} \sum_{m\neq m',\sigma} \hat{n}_{m,\sigma}\hat{n}_{m',\sigma} \tag{2.27}$$

The operator $\hat{n}_{m,\sigma}$ indicates the number of electrons filling an orbital with spin $\sigma$ and magnetic quantum number **m** at a certain location. The energy cost of placing an electron at a certain location, is described by the spherically averaged Hubbard parameter U; $U = E(d^{n+1}) + E(d^{n-1}) - 2E(d^n)$, J represents the screened exchange energy. J is an estimate of the Stoner exchange parameter, and U is dependent on the screening and the spatial extension of the wave functions.

The energy contributions that the DFT functional has previously counted are contained in the Mott-Hubbard Hamiltonian. After subtracting the double-counted terms from the energy given by the classical DFT method, the energy of the spin-polarized DFT + U functional of Dudarev et al. [17, 18] is obtained:

$$E_{DFT+U} = E_{DFT} + \frac{U-J}{2} \sum_{m,\sigma} (\hat{n}_{m,\sigma} - \hat{n}^2_{m,\sigma}) \tag{2.28}$$

Instead of intervening independently, U and J intervene by their difference, which is written in the following formula:

$$U_{eff} = U - J \tag{2.29}$$

## 2.13 Kohn-Sham equations resolution

Solving the Kohn-Sham equations requires choosing a basis for the wave functions that can be described as a linear combination, called Kohn-Sham orbitals. These orbitals are as follows:

$$\psi_i(r) = \sum_j c_{ij}\phi_j(r). \tag{2.30}$$

The coefficients $c_{ij}$ are determined by a variational procedure, which leads to the resolution of the following matrix problem [19]:

$$(H - \epsilon S)c = 0. \tag{2.31}$$

Here :

The eigenvalue is denoted by $\epsilon$ and the solution's coefficients denoted by c are represented as column vectors. The Hamiltonian and the covering matrix are denoted by H and S, respectively, and contain the following matrix elements:

$$H_{ij} = \int \phi_i^*(r)[-\frac{\hbar^2}{2m}\nabla^2 + V_{eff}(r)]\phi_j(r)dr, \tag{2.32}$$

$$S_{ij} = \int \phi_i^*(r)\phi_j(r)dr. \tag{2.33}$$

Finding the coefficients $c_{ij}$ is the result of solving the Kohn-Sham equations; this is accomplished iteratively through a self-consistent cycle of iterations as depicted in Figure.2.2 [20]. This is achieved by injecting the initial charge density to diagonalize the equation (2.31), we start with this charge density.

To create a new charge, we first determine an appropriate potential, then we solve the Kohn-Sham equations and combine the resulting charge with the initial charge. The cycle is repeated until the verification of certain convergence criterion.

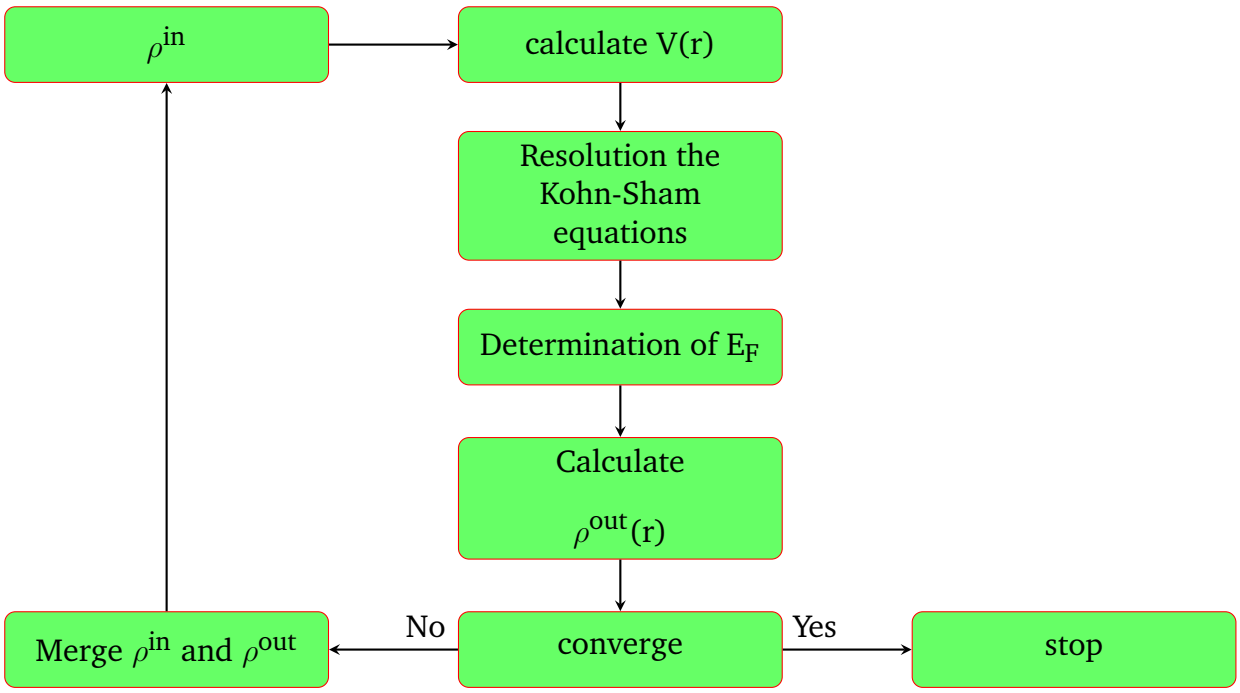


Figure 2.2: Cycle of SCF calculations for solving Kohn-Sham equations.

# REFERENCES


[1] D. Marx and M. Parrinello, "Structural quantum effects and three-centre two-electron bonding in $CH_5^+$," *Nature*, vol. 375, no. 6528, pp. 216–218, 1995.

[2] M. Springborg, "Electronic and structural properties of extended-chain compounds and polymers," *International Journal of Quantum Chemistry*, vol. 77, no. 5, pp. 843–858, 2000.

[3] C. J. Cramer, "Computational chemistry: Theories and models," 2004.

[4] J. C. Slater, "The theory of complex spectra," *Physical Review*, vol. 34, no. 10, p. 1293, 1929.

[5] J. Hafner, "Atomic-scale computational materials science," *Acta Materialia*, vol. 48, no. 1, pp. 71–92, 2000.

[6] W. Kohn and L. J. Sham, "Self-consistent equations including exchange and correlation effects," *Physical review*, vol. 140, no. 4A, p. A1133, 1965.

[7] P. Hohenberg and W. Kohn, "Density functional theory (DFT)," *Phys. Rev*, vol. 136, no. 1964, p. B864, 1964.

[8] Á. Nagy, "Density functional. Theory and application to atoms and molecules," *Physics Reports*, vol. 298, no. 1, pp. 1–79, 1998.

[9] J. P. Perdew and Y. Wang, "Accurate and simple analytic representation of the electron-gas correlation energy," *Physical review B*, vol. 45, no. 23, p. 13244, 1992.

[10] J. P. Perdew, K. Burke, and M. Ernzerhof, "Generalized gradient approximation made simple," *Physical review letters*, vol. 77, no. 18, p. 3865, 1996.

[11] L. Hedin and B. I. Lundqvist, "Explicit local exchange-correlation potentials," *Journal of Physics C: Solid state physics*, vol. 4, no. 14, p. 2064, 1971.

[12] A. D. Becke and E. R. Johnson, "A simple effective potential for exchange," *The Journal of chemical physics*, vol. 124, no. 22, 2006.

[13] F. Tran and P. Blaha, "Accurate band gaps of semiconductors and insulators with a semilocal exchange-correlation potential," *Physical review letters*, vol. 102, no. 22, p. 226401, 2009.

[14] F. Tran, P. Blaha, and K. Schwarz, "Band gap calculations with Becke–Johnson exchange potential," *Journal of Physics: Condensed Matter*, vol. 19, no. 19, p. 196208, 2007.

[15] S. Noui, *Les alliages d'Heusler demi-métallique: étude théoriques des propriétés magnétiques et électroniques*. PhD thesis, UB1, 2019.

[16] V. I. Anisimov, J. Zaanen, and O. K. Andersen, "Band theory and Mott insulators: Hubbard U instead of Stoner I," *Physical Review B*, vol. 44, no. 3, p. 943, 1991.

[17] S. Dudarev, A. Liechtenstein, M. Castell, G. Briggs, and A. Sutton, "Surface states on NiO (100) and the origin of the contrast reversal in atomically resolved scanning tunneling microscope images," *Physical Review B*, vol. 56, no. 8, p. 4900, 1997.

[18] S. L. Dudarev, G. A. Botton, S. Y. Savrasov, C. Humphreys, and A. P. Sutton, "Electron-energy-loss spectra and the structural stability of nickel oxide: An LSDA+ U study," *Physical Review B*, vol. 57, no. 3, p. 1505, 1998.

[19] D. J. Singh and L. Nordstrom, *Planewaves, Pseudopotentials, and the LAPW method*. Springer Science & Business Media, 2006.

[20] E. Wimmer and A. Freeman, "Fundamental of the electronic structure of surfaces," *Electronic structure, edited by K. Horn and M. Scheffler*, vol. 2, 2000.

CHAPTER 3

# FP-LAPW METHOD

## 3.1 Introduction:

Density functional theory (DFT) is an effective and important approach for dealing with the N-body problem. However, the foundation of the wave functions must be properly selected in order to solve the Kohn-Sham equations. According to the density functional theory, the Schrödinger equation may be solved using various methods. These methods vary in terms of the potential that is employed and the wave functions that are utilized as a foundation. Among them are orthogonalized plane wave (OPW) methods and their derivatives [1, 2], which are applicable to conduction bands of (s-p) character of metals, as well as cellular methods of augmented plane wave type ( APW)[3] and the linearized augmented plane wave (LAPW) method.

Periodic boundary conditions are linked to the base of the plane waves in the DFT architecture, very answered in particular for the study of solids, because they satisfy the wave function established by Bloch. The decomposition into plane waves consists in expressing the wave functions using Fourier series as follows:

$$\Psi_n(k, n) = \sum_G C_n(k, G) e^{i(k+G)r} \tag{3.1}$$

Where:

n: band index.

k: wave vector.

## 3.2 Augmented planes waves method (APW):

The augmented plane wave (APW) approach to solving the single-electron Schrödinger equation was first presented by Slater in 1927 [3], which corresponds to the Kohn-Sham equation based on DFT. The potential and wave functions in the vicinity of an atomic nucleus have the form (*Muffin-Tin*), displaying spherical symmetry within the sphere of MT of radius $R_\alpha$ between the atoms, they can be considered as being smooth (constant), as illustrated in Figure.3.1.

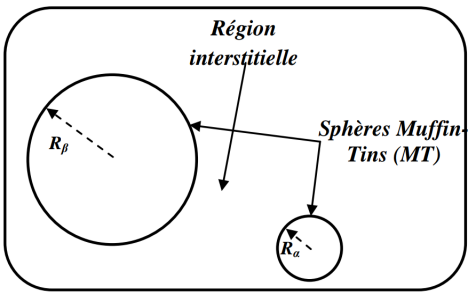


Figure 3.1: *Muffin-Tin* potential.

$$V(\vec{r}) = \begin{cases} V(r) & \cdots r < R_\alpha \\ 0 & \cdots r > R_\alpha \end{cases} \tag{3.2}$$

Consequently, depending on the region taken into consideration, the crystal's wave functions are expanded in various bases:

1. Within the MT sphere, the wave functions are radial solutions (spherical potentials).
2. In the interstitial region, the wave functions are plane waves (constant potential).

Then the wave function $\Phi(r)$ can be expressed as follows:

$$\Phi(r) = \begin{cases} \Omega^{-\frac{1}{2}} \sum_G C_G e^{i(G+k)r} & \cdots r > R_\alpha \\ \sum_{lm} A_{lm} U_l(r) Y_{lm}(r) & \cdots r < R_\alpha \end{cases} \tag{3.3}$$

Where:

$\Omega$: represents the unit cell volume.

$C_G$ and $A_{lm}$: are the coefficients of the spherical harmonic expansion $Y_{lm}$.

r: is the position in polar coordinates inside the MT sphere.

k: is the wave vector in the irreducible Brilloin zone.

G: reciprocal space vector.

The function $U_l(r)$ is a solution of the Schrödinger equation for the radial component, which is expressed as follows:

$$\left[-\frac{d^2}{dr^2} + \frac{l(l+1)}{r^2} + V(r) - E_l\right] rU_l(r) = 0 \tag{3.4}$$

Where:

V(r): the spherical component of the potential in the MT sphere.

$E_l$ : the linearization energy.

Any eigenstate of the core is orthogonal to the radial functions specified by the equation (3.4); nevertheless, this orthogonality vanishes on the sphere's limit [4]. To ensure the continuity of the function $\Phi(r)$ on the surface of the sphere, the coefficients $A_{lm}$ must be constructed in accordance with the coefficients $C_G$ of the plane waves exist in the interstitial area. These coefficients are thus described by the following expression:

$$A_{lm} = \frac{4\pi i^l}{\Omega^{\frac{1}{2}} U_l(R_\alpha)} \sum C_G J_l(|k+G|R_\alpha) Y^*_{lm}(k+G) \tag{3.5}$$

with $J_l(x) = \sqrt{\frac{\pi}{2x}} j_{l+1/2}(x)$: represents the *Bessel* function.

Although the reduction in the material's symmetry makes this method less desirable, it is appropriate for materials having a face-centered cubic (fcc) structure. Furthermore, it exhibits issues with the function $U_l(R_\alpha)$ that is present in the equation's denominator (3.5). Truthfully, depending on how much of the parameter $E_l$ is present, the $U_l(R_\alpha)$ value at the surface of the MT sphere can reach zero, causing a separation of the radial functions with respect to plane wave functions (problem of the asymptote).

To overcome this issue, Koelling [5] and Andersen [4] proposed a number of changes to the APW method. The FP-LAPW method is one of these modifications; it uses a linear combination of the radial functions $U_l(r)$ and their derivatives with respect to the energy $\dot{U}_l$ (r) to represent the wave function $\Phi(r)$ inside the spheres.

## 3.3 Basic functions of FP-LAPW method

To deal with the asymptote issue with the APW method, *Anderson* [4] introduced the LAPW method in 1975. The basis functions in the MT sphere of the FP-LAPW method are linear combinations of the radial functions $U_l Y_{lm}(r)$ and their energy-dependent derivatives $\dot{U}_l\, Y_{lm}(r)$.

The $U_l$ functions are defined as in the APW(3.4) method, and the function $\dot{U}_l\, Y_{lm}(r)$ needs to meet the following condition:

$$\left[-\frac{d^2}{dr^2} + \frac{l(l+1)}{r^2} + V(r) - E_l\right] r\, \dot{U}_l\,(r) = rU_l(r) \tag{3.6}$$

In the non-relativistic situation, by altering the basis's functions, *Anderson* introduced the radial function's first derivative with respect to the energy in the spherical area, thus the new LAPW basis of the FP-LAPW method can be written in the following formula:

$$\Phi(r) = \begin{cases} \Omega^{-\frac{1}{2}} \sum_G C_G e^{i(G+k)r} & \cdots r > R_\alpha \\ \\ \sum_{lm} [A_{lm} U_l(r) + B_{lm}\, \dot{U}_l\,(r)] Y_{lm}(r) & \cdots r < R_\alpha \end{cases} \tag{3.7}$$

The same method used to calculate the coefficients $A_{lm}$ is also used to determine the coefficients $B_{lm}$, which correspond to the function $\dot{U}_l$. In the linearized augmented plane wave (LAPW) method, plane waves are always used in the interstitial area (as in the APW approach), but inside the sphere, linearly augmented plane waves (LAPWs) are used, which have more variational freedom than the augmented plane waves (APWs) in the augmented plane wave (APW) approach. The following expression can be used to expand radial functions in the region of $E_l$:

$$U_l(E, r) = U_l(\varepsilon_l, r) + (\varepsilon - E_l)\, \dot{U}_l\,(r) + O[(\varepsilon - E_l)^2] \tag{3.8}$$

Where:

$O[(E - E_l)^2]$ represents the quadratic energy error.

However, in comparison to the augmented plane wave method, this approach somewhat reduces the computations' precision; the errors on the wave functions and the band energy are of the order $(\varepsilon - E_l)^2$ and $(\varepsilon - E_l)^4$, respectively.

When compared to the augmented plane wave approach, the LAPW method's primary advantages are:

1. The LAPW functions form a good basis, which allows with a single value of El to obtain all the valence bands in a large energy region. If this is not possible, the energy window can usually be split into two parts, which is much simpler than the APW method.

2. The LAPW method ensures that the plane waves with radial functions do not decouple and removes the asymptote problem by incorporating the derived from the radial function with respect to the energy.

## 3.4 linearization

In the LAPW approach, the linearization energies $E_l$ are crucial. The LAPW method reduces to APW method when $E_l$ equals the energy of the considered band , the selection of this parameter is not always easy; in some cases, the existence of core states, extended states known as semi-core states can occasionally cause issues and cause calculations to fail. If there are no core states with the same moment angular l, the functions $U_l(r)Y_{lm}(r)$ and $\dot{U}_l(r)Y_{lm}(r)$ are orthogonal for the core states that are fully contained in the spheres. These states are not orthogonal if this criterion is not met since the wave functions of the valence states will have an extended core states component. In certain cases, the base LAPW's functions and the core's states will overlap, and the energy spectrum will show what is known as the ghost band. The best solution to this problem is to use development in local orbitals [6], but this solution is not available in all the codes, increasing the muffin-tin spheres' radius is an additional option.

## 3.5 Construction of non-relativistic radial functions

Plane waves in the interstitial area are the basic components of the linearized augmented plane wave (LAPW) approach. As long as the fundamental functions and their derivatives are continuous at the sphere's surface, they are produced in the numerical radial functions form inside the MT spheres. Therefore, building the LAPW method's fundamental functions entails figuring out:

1. The radial functions $U_l(r)$ and their derivatives with respect to the energy $\dot{U}_l(r)$.

2. The boundary conditions are met by the coefficients $A_{lm}$ and $B_{lm}$.

Boundary conditions offer a straightforward method for representing the cutoff $G_{max}$ of plane waves in the MT sphere and for calculating the cutoff angular moment (cutoff) $l_{max}$. A reasonable approach would be to select these cutoffs such that $R_\alpha G_{max} = l_{max}$, which is accomplished in practice since $R_\alpha G_{max}$ between 7 and 9 guarantees the convergence of the LAPW calculations. In the non-relativistic application, the radial functions $U_l(r)$ are solutions of the radial Schrödinger equation with a spherical potential and for a linearization energy $E_l$. We have:

$$\left[-\frac{d^2}{dr^2} + \frac{l(l+1)}{r^2} + V(r) - E_l\right] rU_l(r) = 0 \tag{3.9}$$

Where the radial part of the potential in the MT sphere for $l = 0$ is denoted by V(r). When the boundary condition $rU_l(r) = 0$ is applied, the derivative of the equation (3.9) with respect to $E_l$ is:

$$\left[-\frac{d^2}{dr^2} + \frac{l(l+1)}{r^2} + V(r) - E_l\right] r\,\dot{U}_l(r) = rU_l(r) \tag{3.10}$$

It is necessary that the radial solutions be normalized inside the MT spheres:

$$\int_0^{R_\alpha} [rU_l(r)]^2\,dr = 1 \tag{3.11}$$

$U_l$ is a solution of the inhomogeneous equation (3.10) of the form:

$$h_1\,\dot{U}_l - E\,\dot{U} = U_l \tag{3.12}$$

The orthogonalization of $U_l(r)$ and $\dot{U}_l(r)$ gives:

$$\int_0^{R_\alpha} r^2 U_l(r)\,\dot{U}_l(r)\,dr = 0 \tag{3.13}$$

The function $\dot{U}_l(r)$ is normalized:

$$\int_0^{R_\alpha} \left[r\,\dot{U}_l(r)\right]^2 dr = 1 \tag{3.14}$$

This normalization condition can be replaced by the following equation:

$$R_\alpha^2 \left[U_l'(R_\alpha)\,\dot{U}_l(R_\alpha) - U_l(R_\alpha)\,\dot{U}_l'(R_\alpha)\right] = 1 \tag{3.15}$$

Where:

$U_l'(E, r) = \left(\frac{\partial U_l(E,r)}{\partial r}\right)$

$\dot{U}_l'(E, r) = \left(\frac{\partial U_l(E,r)}{\partial E}\right)$

This equation is used to calculate the functions $U_l(r)$ and $\dot{U}_l(r)$, and the function $U_l$ can be defined as follows:

$$U_l(E + \delta) = U_l(E) + \delta\,\dot{U}(E) + \ldots \tag{3.16}$$

With this choice, the norm of $\dot{U}_l'$, which is $\|\dot{U}_l\|$, allows an indication on the interval where the linearizing of the energy will be a good and reasonable approximation. The errors of linearization are acceptable for most quantities when the condition $\|\dot{U}_l'\|\,|E_l - \epsilon| \leq 1$ is verified, where $E_l$ is the energy parameter and $\epsilon$ is the band energy.

Otherwise, other options are adopted, namely:

1. Divide the energy interval into windows and treat them separately.

2. Use a development of local orbitals (the quadratic method).

3. Reduce the size of the sphere, i.e., reduce the norm $\dot{U}_l$ (r).

The relativistic correction is important only when the kinetic energy becomes important; in other words, this effect is important in the heavy elements, which possess a high atomic number. Relativistic effects are taken into account inside the spheres and are neglected in the interstitial area, so the modifications will affect only the radial functions in the spheres and the components of the Hamiltonian operating on them.

## 3.6 Determination of coefficients $A_{lm}$ and $B_{lm}$

For each atom, the coefficients $A_{lm}$ and $B_{lm}$ are found by requiring that the basis functions and their first derivatives be continuous at the spheres' boundaries [7, 8].

The basis functions are plane waves in the interstitial area:

$$\Phi_{k_n} = \Omega^{-\frac{1}{2}} e^{ik_n r} \tag{3.17}$$

$$k_n = k + K_n \tag{3.18}$$

Where :

$\Omega$: volume of the elementary cell.

k: wave vector.

$k_n$: reciprocal lattice vector.

In the spherical region:

$$\Phi_{k_n} = \sum_{lm} [A_{lm} U_l(E_l) + B_{lm} \dot{U}_l (E_l)] Y_{lm}(r) \tag{3.19}$$

A plane wave expansion of *Rayleigh* can be used because of the boundary condition at the MT sphere's surface.

$$\Phi(k_n, R_\alpha) = \frac{4\pi}{\sqrt{\Omega}} \sum_{lm} i^l j_l(k_n, R_\alpha) Y^*_{lm}(k_n) Y_{lm}(R_\alpha) \tag{3.20}$$

Taking into account the continuity of the angular momentum it can obtain:

$$A_{lm}(k_n) = \frac{4\pi}{\sqrt{\Omega}} R^2_\alpha i^l Y^*_{lm}(k_n) a_l(k_n) \tag{3.21}$$

$$a_l(k_n) = \frac{\dot{U}_l\,(\frac{d}{dr})j_l(k_nR_\alpha) - (\frac{d\dot{U}_l}{dr})j_l(k_nR_\alpha)}{R_\alpha^2\left[(\frac{dU_l}{dr})\,\dot{U}_l - U_l(\frac{d\dot{U}_l}{dr})\right]} \tag{3.22}$$

$$B_{lm}(k_n) = \frac{4\pi}{\sqrt{\Omega}}R_\alpha^2 i^l Y_{lm}^*(k_n)b_l(k_n) \tag{3.23}$$

$$b_l = \frac{(\frac{dU_l}{dr})j_l(k_nR_\alpha) - U_l(\frac{d}{dr})j_l(k_nR_\alpha)}{R_\alpha^2\left[(\frac{dU_l}{dr})\,\dot{U}_l - U_l(\frac{d\dot{U}_l}{dr})\right]} \tag{3.24}$$

The full potential linearized augmented plane wave (FP-LAPW) method has thus eliminated the problem of the asymptote, which appears in the augmented plane wave (APW) method.

## 3.7 Potential determination

### 3.7.1 Poisson equation resolution

The exchange and correlation terms as well as the Coulomb term $V_C(r)$ are included in the potential utilized in the Kohn-Sham equations. The Coulomb term is the sum of the Hartree potential and nuclear potential.

The Poisson equation is used to get $V_C(r)$ from the charge density:

$$\nabla^2 V_C(r) = 4\pi\rho(r) \tag{3.25}$$

This equation can only be integrated in the reciprocal lattice. The resolution of this equation is done with the so-called pseudo-charge method [8] (the process is demonstrated in Figure.3.2), based on two observations:

1. The charge density is continuous; in the spherical zone, it fluctuates quickly, while in the interstitial region, it varies slowly.

2. Both the interstitial charge and the multi-pole of the charge inside the sphere affect the Coulomb potential in the interstitial region.

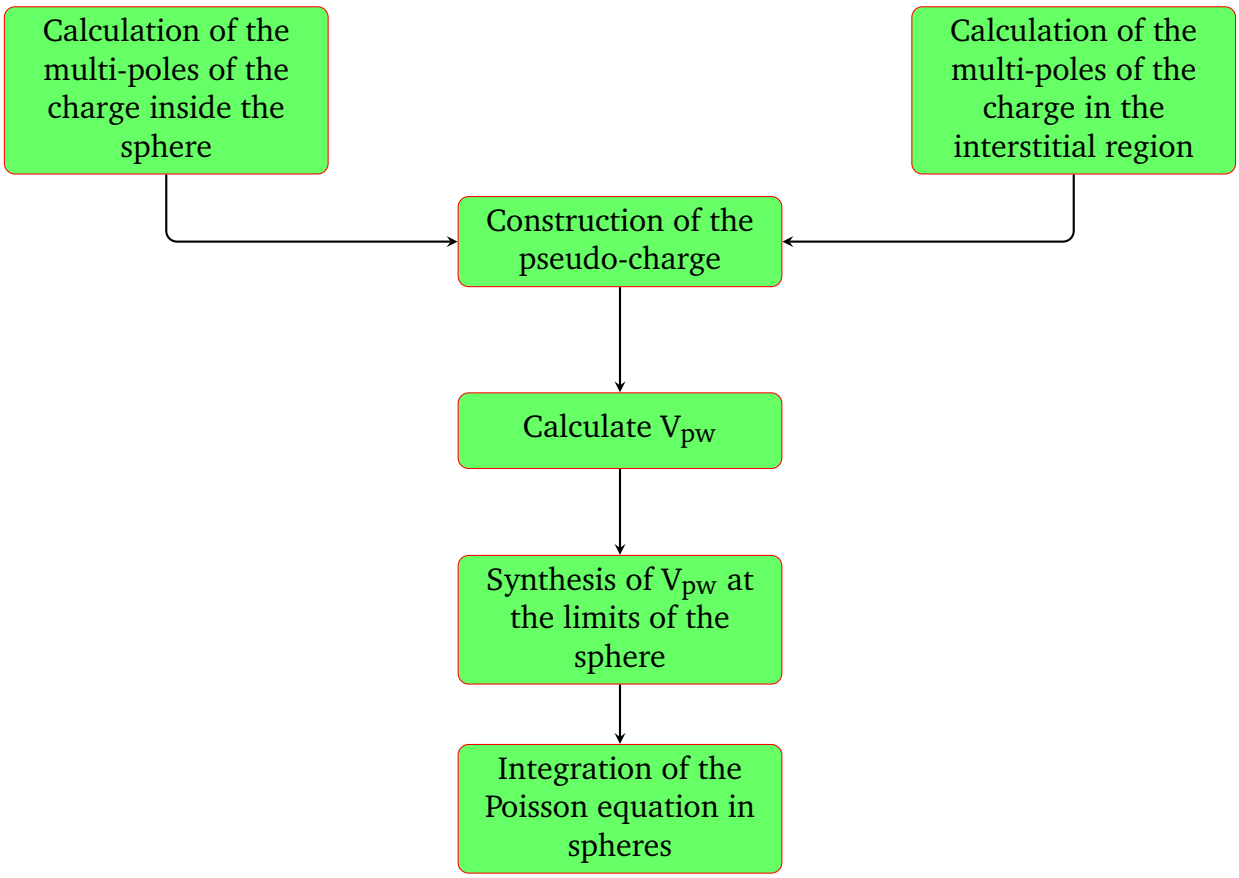


Figure 3.2: Solving the Poisson equation using the pseudo-charge method.

The charge density in the interstitial region is developed in Fourier series, and the Poisson equation is integrated in the reciprocal space.

$$\rho(r) = \sum_G \rho(G) e^{iGr} \tag{3.26}$$

The plane waves $e^{iGr}$ are expressed in terms of Bessel functions $j_l$.

$$\int_0^R r^{l+2} j_l(Gr)dr = \begin{cases} \sum_k V_k e^{ikr} \frac{R^{l+3} j_l(Gr)}{Gr} & \cdots G \neq 0 \\ \frac{R^3}{3}\delta_{l,0} & \cdots G = 0 \end{cases} \tag{3.27}$$

$$e^{iGr} = 4\pi e^{iGr_\alpha} \sum_{lm} i^l j_l(|G|.|r - r_\alpha|) Y^*_{lm}(G) Y_{lm}(r - r\alpha) \tag{3.28}$$

Where:

r: is the radial coordinate.

$r_\alpha$: the position of the sphere $\alpha$ and its radius $R_\alpha$.

$$V_C(G) = \frac{4\pi\rho(G)}{G^2} \tag{3.29}$$

The interstitial potential $V_{pw}$ is given by:

$$V_{pw} = \sum_{lm} V_{lm}^{pw}) Y_{lm}(r) = \sum_{\nu} V_{\nu}^{pw}) Y_{\nu}(r) \tag{3.30}$$

Either:

$$K_{\nu}(r) = \sum_{m} C_{\nu m} Y_{lm}(r) \tag{3.31}$$

Where:

$K_{\nu}(r)$ are the symmetrical spherical harmonics (the lattice harmonics).

Hence:

$$V_{\nu}^{pw} = \sum_{lm} C_{\nu m} Y_{lm}^{pw}(r) \tag{3.32}$$

The Green function is used to compute the potential inside the Muffin-Tin sphere.

$$V_{r}^{(}r) = V_{lm}^{pw}(r) \left[\frac{r}{R}\right]^{l} + \frac{4\pi}{2l+1} \left\{ \frac{1}{r^{l+1}} \int_{0}^{r} dr' r'^{l+1} \rho_{nu}(r') - \frac{r^{l}}{R^{2l+1}} \int_{0}^{Rr} dr' r'^{l+2} \rho_{\nu}(r) \right\} \tag{3.33}$$

Where the $\rho_{v}(r)$ are the radial parts of the charge density.

### 3.7.2 Exchange-correlation potential

In the local density approximation (LDA), the exchange and correlation potential is linear, unlike the Coulomb potential. As a result, it needs to be computed in real space, which is fortunately diagonal. The procedure is illustrated in Figure.3.3. Through the Fourier transformation, the pore load is obtained directly in real space [9, 10].

Mattheiss [11] used Wigner's formula [12] to obtain the interstitial potential following exchange and correlation:

$$V_{xc} = -\rho^{1/3} \left[ 0.984 + \frac{0.943656 + 8.8963\rho^{1/3}}{\left(1 + 12.57\rho^{1/3}\right)^{2}} \right] \tag{3.34}$$

Inside the spheres, the same procedure is applied with different values of $\rho$ and a spherically symmetric potential.

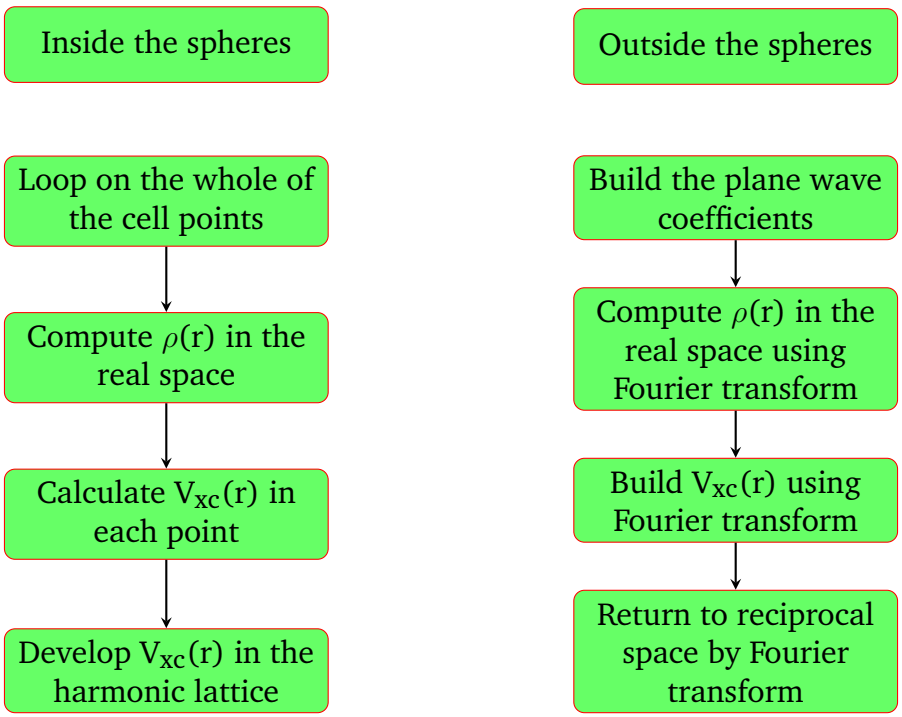


Figure 3.3: Calculation of exchange and correlation potential.

## 3.8 Improvement of the FP-LAPW method

Accurate band energies near the linearization energies $E_l$ are the aim of the LAPW method [4]. Selecting these energies close to the band center is adequate for the majority of materials. As an example, materials having 4f orbitals [13, 14], and elements of transition metals [15] are examples of materials for which selecting a single value of $E_l$ is insufficient to calculate all the bands energy. This is the primary problem with the semi-core state, which is intermediate between the valence and the core states.

There are two approaches to handling this circumstance:

1. Use multiple energy windows.

2. Use a development in local orbitals.

### 3.8.1 Multiple energy windows

The method most used to treat the problem of the semi-core is the division of the energy spectrum into windows, each of which represents an energy $E_l$ [11, 14].
The semi-core state and the valence state are separated in this window-based treatment, where each window's relevant states are processed by selecting a set of $E_l$. This is equivalent to performing two LAPW calculations, independent, having the same potential, though.

The foundation of the full potential linearized augmented plane wave (FP-LAPW) method is the fact that the functions $U_l$ and $\dot{U}_l$ are orthogonal to any proper core's state, especially those at the sphere's surface. However, semi-core states often satisfy this condition, unless the valence state and the semi-core state are separated by ghost bands.

### 3.8.2 Development in local orbitals

In order to avoid using multiple windows, the LAPW method's evolution involves modifying the local orbitals of its database. The main idea is to treat all bands with a single energy window by particularizing the semi-core state.
Several proposals have been made by Takeda [16] and Srnrcka [17] and others. A linear combination of two radial functions that represent two distinct energies and the derivative with regard to the energy of one of these functions has been recently put forward by Singh [18]:

$$\phi_{lm}(r) = \begin{cases} \left[A_{lm}U_l(r, E_{1,l}) + B_{lm}\ \dot{U}_l\ (r, E_{2,l}) + C_{lm}U_l(r, E_{2,L})\right] Y_{lm}(r) & \cdots r < R_\alpha \\ 0 & \cdots r > R_\alpha \end{cases} \tag{3.35}$$

Where:

$C_{lm}$ coefficients are identical to the previously specified coefficients $A_{lm}$ and $B_{lm}$. Additionally, this modification minimizes the inaccuracy in the conduction and valence bands' calculation.

## 3.9 Concept of FP-LAPW method

Instead, they are developed into Fourier series in the interstitial regions and in harmonics of the lattice within each atomic sphere. This is where the moniker Full-Potential came from. This method develops the potential in the following form and guarantees its continuity on the sphere MT's surface:

$$V(r) = \begin{cases} \sum_k V_k e^{ikr} & \cdots r < R_\alpha \\ \sum_k V_{lm}(r) Y_{lm}(r) & \cdots r > R_\alpha \end{cases} \tag{3.36}$$

Similarly, the charge density is developed as follows:

$$\rho(r) = \begin{cases} \sum_k \rho_k e^{ikr} & \cdots r < R_\alpha \\ \sum_k \rho_{lm}(r) Y_{lm}(r) & \cdots r > R_\alpha \end{cases} \tag{3.37}$$

The use of lattice symmetry is fruitful in representing the density of charge and potential, and helps a lot to simplify and reduce the calculation time.

In the LAPW method, only the charge density considered:

- Has the site's symmetry inside the spheres.
- In the interstitial region, it has space group symmetry.
- The density is a real quantity.
- Is identical inside the equivalent atoms.

## 3.10 General description of the WIEN2K code

The Institute of Materials Chemistry at the Technical University of Vienna developed the WIEN2K simulation code, which Blaha P., Schwartz K., Sorintin P., and Trickey S.B. published in 1990 [19, 20]. In the years that followed, this code was continually revised and underwent several updates. Versions of the original WIEN code were developed (named according to the year of their appearance, WIEN93, WIEN95, WIEN97, etc.). In our case we used the WIEN2K version 2021.

The WIEN2K package is written in FORTRAN, it works under the system LINUX operating system. It consists of several independent programs that are linked by C-SHEL SCRIPT. These programs use the density functional theory (DFT) to calculate the electronic structure of solid bodies.

Several properties of materials can be calculated with this code, among which:

- ✳ Density of state, bands structure and Fermi energy.
- ✳ Spin density, electron's density and X-ray structure factors.
- ✳ Total energy, atomic forces, equilibrium geometries and structural optimizations.
- ✳ Spin polarization (ferromagnetic, antiferromagnetic, etc.).
- ✳ X-ray emission and absorption spectra.
- ✳ Optical properties.

### 3.10.1 WIEN2K algorithm

The structure of the WIEN2K program (computation steps) is demonstrated in Figure.3.4. The first calculation step is the initialization, which consists in executing a series of auxiliary programs that will produce inputs for the main programs:

**NN**: a subroutine allowing to check the distances between nearest neighbors and equivalent positions (non-overlapping spheres) as well as to determine the atomic radius of the spheres.

**LSTART**: it specifies how the various atomic orbitals are treated in the band structure calculation and enables the generation of atomic densities.

**SYMMETRY**: it enables the generation of the space group's symmetry operations and the identification of each atomic site's point group.

**KGEN**: in the first Brilloin zone, it produces the number of k-points.

**DSART**: by superposing the atomic densities produced in LSTART, it creates started density for the self-consistent cycle, also known as the SCF cycle.

### 3.10.2 SCF calculation

The initialization of the calculation having thus been created, the SCF process is then launched and iterated until the solution converges. The SCF cycle can be invoked by the command **run_LAPW**, which includes the following steps:

**LAPW0**: uses the total electron density, known as the input, to produce the potential (the sum of the coulomb and the exchange-correlation potential). It divides space into sphere MT and interstitial region and computes $V_{XC}$ numerically.

**LAPW1**: this is the subroutine that finds the Hamiltonian, the matrix of overlap, eigenvalues, and eigenvectors (it calculates valence bands) by a diagonalization method. This program consumes most of the calculation time.

**LAPW2**: it calculates the Fermi energy, the valence densities (from vectors own) made up of the densities of electrons inside each sphere MT (expressed by spherical harmonics) and in the interstitial region (expressed by a series of Fourier).

**LCORE**: determines the densities of the core states of the potential's spherical part.

**MIXER**: creates a new density by combining the valence and core densities.

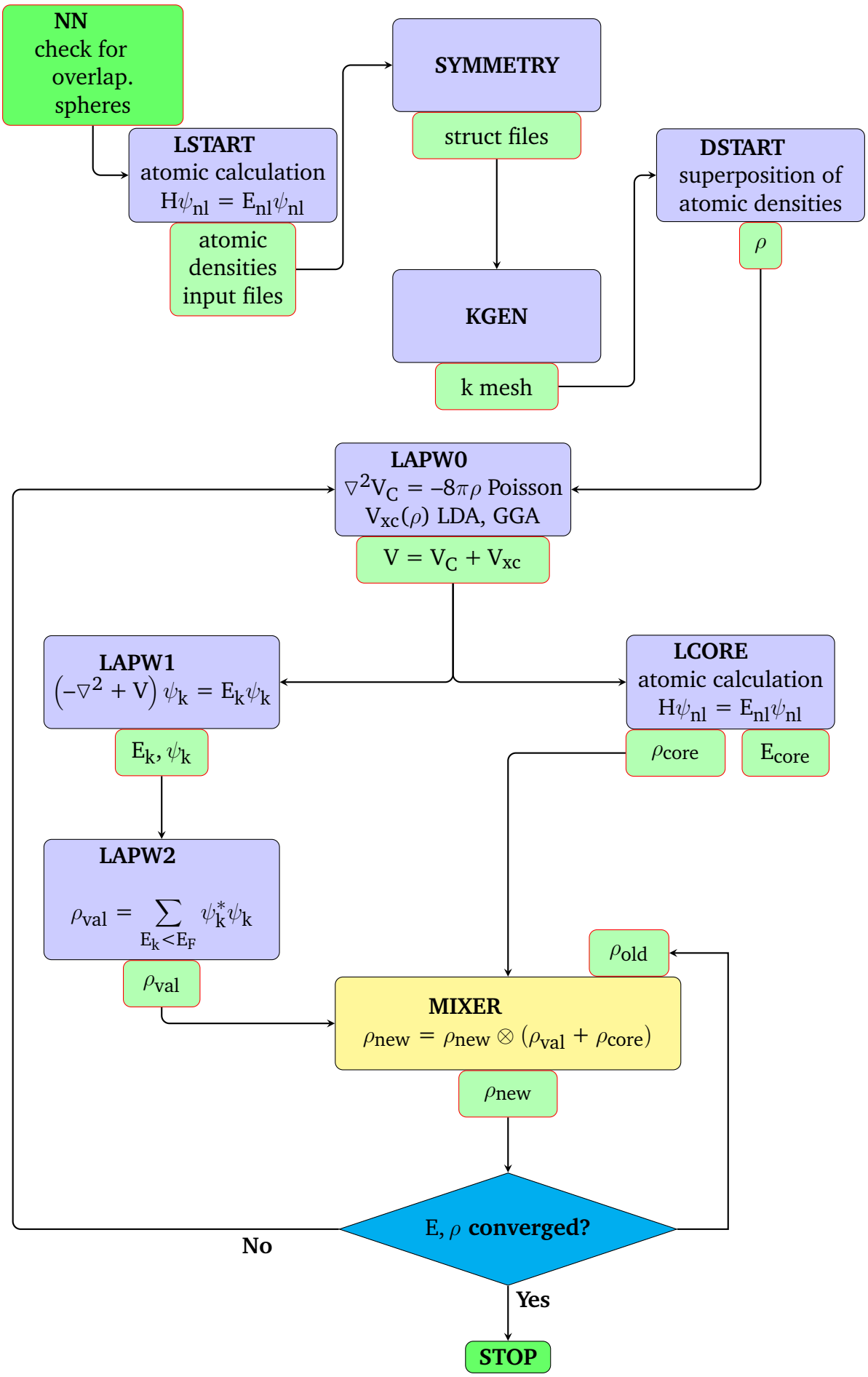


Figure 3.4: Structure of the WIEN2k code.

# REFERENCES


[1] J. C. Slater, *Quantum Theory of Molecules and Solids. Vol. 2: Symmetry and Energy Bands in Crystals*. New York, 1965.

[2] C. Herring, "A new method for calculating wave functions in crystals," *Physical Review*, vol. 57, no. 12, p. 1169, 1940.

[3] J. C. Slater, "Wave functions in a periodic potential," *Physical Review*, vol. 51, no. 10, p. 846, 1937.

[4] O. K. Andersen, "Linear methods in band theory," *Physical Review B*, vol. 12, no. 8, p. 3060, 1975.

[5] D. Koelling and G. Arbman, "Use of energy derivative of the radial solution in an augmented plane wave method: application to copper," *Journal of Physics F: Metal Physics*, vol. 5, no. 11, p. 2041, 1975.

[6] J. Singh David, "Planewaves, pseudopotentials and the lapw method," 1994.

[7] K. Schwarz and P. Blaha, "Description of an LAPW DF program (WIEN95)," *Quantum-Mechanical Ab-initio Calculation of the Properties of Crystalline Materials*, pp. 139–153, 1996.

[8] F. El Haj Hassan, *Contribution à l'étude des propriétés électroniques et structurales des composés à base de bore et de cuivre*. PhD thesis, Metz, 2000.

[9] R. Singleton, "An algorithm for computing the mixed radix fast Fourier transform," *IEEE Transactions on audio and electroacoustics*, vol. 17, no. 2, pp. 93–103, 1969.

[10] A. McLaren, “Optimal numerical integration on a sphere,” *Mathematics of Computation*, vol. 17, no. 84, pp. 361–383, 1963.

[11] L. Mattheiss and D. Hamann, “Linear augmented-plane-wave calculation of the structural properties of bulk Cr, Mo, and W,” *Physical Review B*, vol. 33, no. 2, p. 823, 1986.

[12] E. Wigner, “On the interaction of electrons in metals,” *Physical Review*, vol. 46, no. 11, p. 1002, 1934.

[13] D. Singh, “Adequacy of the local-spin-density approximation for Gd,” *Physical Review B*, vol. 44, no. 14, p. 7451, 1991.

[14] S. Goedecker and K. Maschke, “Alternative approach to separable first-principles pseudopotentials,” *Physical Review B*, vol. 42, no. 14, p. 8858, 1990.

[15] D. Singh and H. Krakauer, “H-point phonon in molybdenum: Superlinearized augmented-plane-wave calculations,” *Physical Review B*, vol. 43, no. 2, p. 1441, 1991.

[16] T. Takeda and J. Kubler, “Linear augmented plane wave method for self-consistent calculations,” *Journal of Physics F: Metal Physics*, vol. 9, no. 4, p. 661, 1979.

[17] L. Smrčka, “Linearized augmented plane wave method utilizing the quadratic energy expansion of radial wave functions,” *Czechoslovak Journal of Physics B*, vol. 34, no. 7, pp. 694–704, 1984.

[18] D. Singh, “Ground-state properties of lanthanum: Treatment of extended-core states,” *Physical Review B*, vol. 43, no. 8, p. 6388, 1991.

[19] J. P. Perdew, “Density-functional approximation for the correlation energy of the inhomogeneous electron gas,” *Physical Review B*, vol. 33, no. 12, p. 8822, 1986.

[20] J. P. Perdew, “Erratum: Density-functional approximation for the correlation energy of the inhomogeneous electron gas,” *Physical review B*, vol. 34, no. 10, p. 7406, 1986.

# CHAPTER 4

# RESULTS AND DISCUSSION

## 4.1 Introduction

Heusler alloys have long been of particular interest, as they are the basis of many applications in spintronics. As a result, their roles in future industries will continue to grow more and more important. In the context of DFT, ab-initio methods enable the prediction of the physical and chemical characteristics of solid materials under high-pressure conditions. In order to design new materials, various theoretical models have been proposed in order to interpret experimental measurements and predict new effects.

Recently, a novel type of materials called sp ($d^0$) magnets have garnered significant attention due to their diverse functional properties, including half-metallicity, high spin polarization, and potential applications in the field of spintronic. Additionally, an interesting class of Heusler alloys that has received considerable attention in theoretical studies is the iron (Fe)-based alloys. $Fe_2$-based Heusler alloys open new avenues for accelerated materials discovery and its use in spintronics and superconductivity [1, 2]. These kinds of materials have an interesting Curie temperature, a half metallic ferromagnet (HMF) feature, and perfect spin polarization (100%).

In this chapter, we are interested in quaternary Heusler alloys excluding and including transition metals. These alloys are in the form $KMgNO_{1-x}Si_x$ and $FeTiCrAl_{1-x}Si_x$ with $(0 \leq x \leq 1)$. The aim of this work is the contribution to the determination of the structural, mechanical, electronic, magnetic and the thermodynamic properties of these promising materials. For this purpose, we used a theoretical method called FP-LAPW within the framework of the density functional theory (DFT).

## 4.2 Computational details

In this work, the calculations of the physical characteristics of the studied alloys were performed using the Wien2k package [3] based on the density functional theory (DFT) [4] utilizing FP-LAPW method [5]. For the calculation of the mentioned properties, the exchange-correlation potential was treated by the generalized gradient approximation (GGA). Although this standard DFT function generally provides good predictions, it fails to obtain a correct insulating ground state, accurate charge densities, and correct orbital occupancy when applied to strongly correlated electron systems.

To correct the limitations, the so-called GGA + Hubbard (GGA + U) method is developed. The GGA + U method provides a way to overcome these errors through the use of a parameterized potential that uses an exact treatment of exchange interactions. The GGA + U approach was applied to investigate the on-site correlation at the 3d transition metals. In particular, the values of U are calculated using the Quantum espresso package [6], and the obtained values are 5.00 eV, 3.75 eV and 4.68 eV for Fe, Ti and Cr atoms, respectively. The electronic properties were also calculated using the mBJ approach [7], which was also used to overcome the problem of underestimation of the gap energy obtained by the standard DFT method (GGA). The electronic configurations of each atom of KMgNZ (Z = O or S) alloys are: K:[Ar]$4s^1$, Mg:[Ne]$3s^2$, N:[He]$2s^2 2p^3$, O:[He]$2s^2 2p^4$ and S:[Ne]$3s^2 3p^4$. While the electronic configurations of FeTiCrX ((X = Al or Si) atoms are: Fe: [Ar] $3d^6 4s^2$, Ti: [Ar] $3d^2 4s^2$, Cr: [Ar] $3d^5 4s^1$, Al: [Ne] $3s^2 3p^1$ and Si: [Ne] $3s^2 4p^2$. Further, the muffin-tin (MT) radii is 2.50 bohr for K and Mg atoms and 2.00 bohr for O and S atoms. While its values in bohr are 2.04, 1.94, 1.99, 1.69 and 1.97 for Fe, Ti, Cr, Al and Si, respectively.

For the cubic configurations Y-type (type I, type II and type III), a set of 5000 k-points was used in the Brillouin zone (BZ) integration, which was sufficient to achieve convergence. The basis function for each type was expanded up to $R_{MT}K_{max} = 7$, where $R_{MT}$ is the smallest muffin-tin radius and $K_{max}$ is the largest reciprocal lattice vector. In addition, the self-consistent cycles are considered to be converged when the total energy and the charge of the system are stable within $10^{-5}$ Ry and $10^{-3}$ e, respectively. The electronic density of states (DOS) was calculated with a dense mesh of 17x17x17 k-points for the most stable phase. Besides, the muffin-tin radius of each atom in the studied alloys is chosen as follows:

Table 4.1: RMT values of K, Mg, N, O, S, Fe, Ti, Cr, Al and Si atoms.

| Element | K | Mg | N | O | S | Fe | Ti | Cr | Al | Si |
|---|---|---|---|---|---|---|---|---|---|---|
| $R_{MT}$ (u.m.a) | 2.50 | 2.20 | 2.00 | 2.00 | 2.00 | 2.04 | 1.94 | 1.99 | 1.69 | 1.97 |

## 4.3 Structural properties

The optimization of the total energy for the materials at hand is required in order to determine the various ground state features. This step allows us to predict the most stable phase in which the material crystallizes. Once hydrostatic equilibrium is reached, we can access the different physical properties (electronic, mechanical, thermodynamic, optical, etc.).

The common procedure used to determine these properties is to perform a self-consistent calculation (SCF) of the total energy for different values of the lattice parameter $a_0$. Moreover, to ascertain the ground state characteristics, such as the equilibrium lattice parameter ($a_0$) and bulk modulus (B), the equation of states was fitted using the Murnaghan formula [8], which expressed as follows:

$$E_T(V) = E_0 + \left(\frac{BV}{B'}\right)\left[\left(\frac{V_0/V}{B'-1}\right)^{B'} + 1\right] \tag{4.1}$$

Where:

$V_0$ is the volume of the unit cell at equilibrium, and $B_0'$ is the first derivative of the bulk modulus. Using the following formula, we can get the bulk modulus from the curve E(V) minimum:

$$B_0 = V\frac{\delta^2 E}{\delta V^2} \tag{4.2}$$

It is worth to mention that all crystal optimizations were performed in two steps:

1. The first at fixed volume (relaxation) in order to optimize the atomic positions in the cell.

2. The second at unconstrained volume in order to optimize the cell parameters and refine the position of the atoms.

Moreover, the calculations were carried out by taking supercells of 16 atoms repeated periodically.

### 4.3.1 Equilibrium state and structural stability

The studied alloys KMgNZ (Z = O or S) and FeTiCrX (X = Al or Si) have a chemical composition XX′YZ with F$\bar{4}$3m space group (LiMgPdSn prototype), where the X, X′, Y and Z atoms can occupy one of the following sites: 4a(0.0.0), 4c(0.25,0.25,0.25), 4b(0.5,0.5,0.5), and 4d(0.75,0.75,0.75), respectively (see Figure.4.1). The atomic coordinates of each element in the three possible configurations of the considered materials are depicted in Table.4.2.

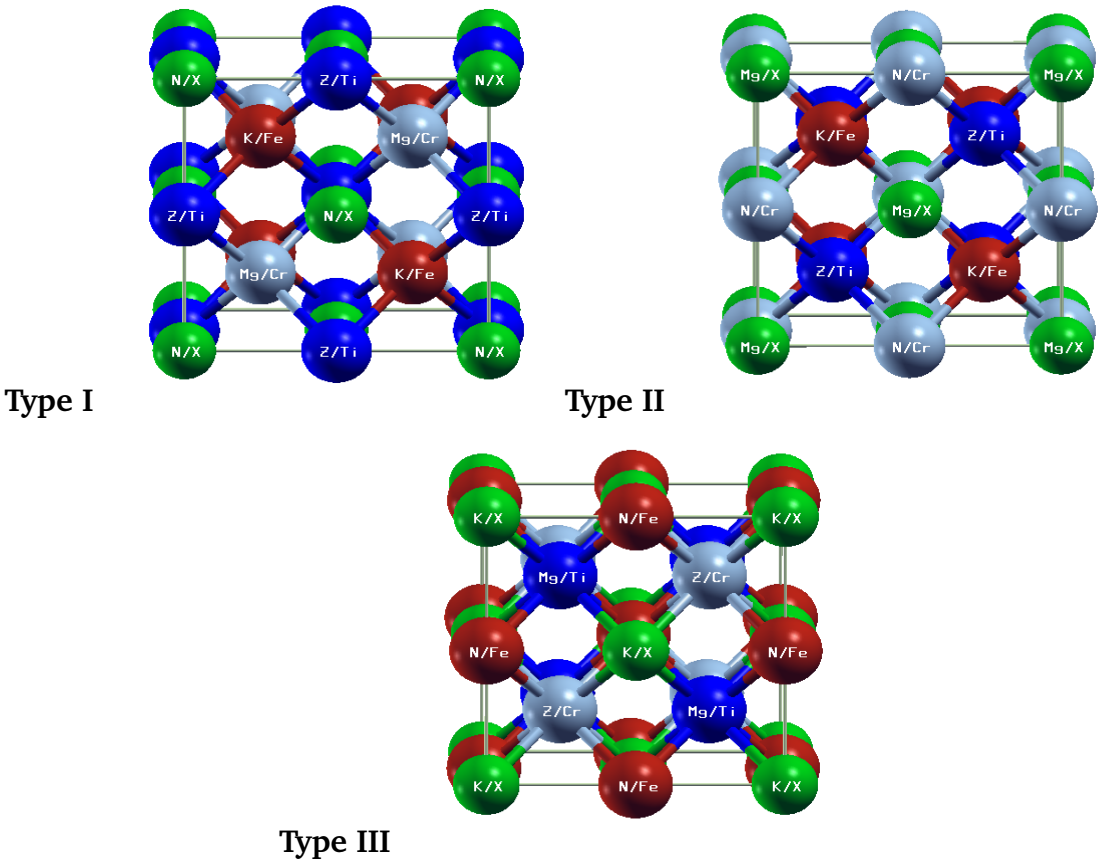


Figure 4.1: The crystal structure of KMgNZ (Z = O or S) and FeTiCrX (X = Al or Si) alloys in the three configurations.

Table 4.2: Three different occupancy for the parent compounds KMgNZ (Z = O or S) and FeTiCrX (X = Al or Si).

| Configuration | Space group | 4a | 4b | 4c | 4d |
|---|---|---|---|---|---|
| **Type I** | F$\bar{4}$3m | N/X | Z/Ti | K/Fe | Mg/Cr |
| **Type II** | F$\bar{4}$3m | Mg/X | N/Cr | K/Fe | Z/Ti |
| **Type III** | F$\bar{4}$3m | K/X | N/Fe | Mg/Ti | Z/Cr |

Initially, we used the GGA exchange-correlation function, and performed a spin polarization calculation, in order to determine the most stable type, which has the lowest energy. The obtained results are shown in Figure.4.2. One can notice that the total energy of type I for the parent compounds is the lowest for both systems. Providing that, this configuration is the most stable.

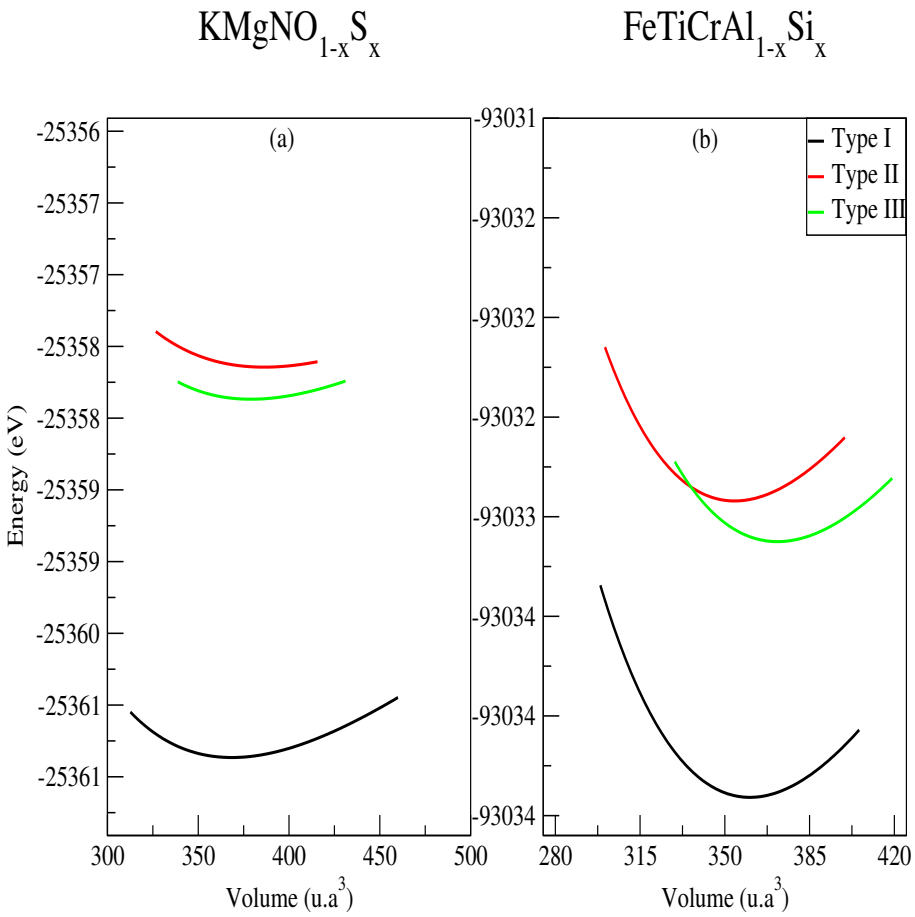


Figure 4.2: The total energy as a function of unit cell volume of the alloys $KMgNO_{1-x}Si_x$ (a) and $FeTiCrAl_{1-x}Si_x$ (b) in the three different configurations.

Tables.4.3 and 4.4 summarized different ground states properties of the materials under consideration. For $KMgNO_{1-x}S_x$ there are no theoretical or experimental data to compare our results with. While for $FeTiCrAl_{1-x}Si_x$, we can conclude from the obtained values of the lattice parameter and the bulk modulus that they agree well with the corresponding calculated data in Ref. [9] using the same functional algorithm (GGA). In addition, one can observe that the bulk moduli of Fe-Based alloys are higher than those of K-based alloys, hence the formers are the stiffer. For $KMgNO_{1-x}S_x$ alloys the lattice parameter increases the S concentration. While for $FeTiCrAl_{1-x}Si_x$ we note that the lattice parameter decreases by increasing the concentration of Si atoms.

Furthermore, by making a comparison between the total energy of the ferromagnetic

Table 4.3: The equilibrium lattice parameter $a_0$(A), first derivative of the bulk modulus B′ (GPa) and the bulk modulus $B_0$ (GPa).

| Compound | $a_0$ | B' | $B_0$ |
|---|---|---|---|
| KMgNO | 6.02 | 4.68 | 65.31 |
| $KMgNO_{0.75}S_{0.25}$ | 6.21 | 5.00 | 57.33 |
| $KMgNO_{0.50}S_{0.50}$ | 6.36 | 4.71 | 52.21 |
| $KMgNO_{0.25}S_{0.75}$ | 6.51 | 4.08 | 48.42 |
| KMgNS | 6.64 | 3.68 | 48.58 |
| FeTiCrAl | 5.97 | 4.16 | 165.42 |
| **Other calc.**[9] | 5.97 | – | – |
| $FeTiCrAl_{0.75}Si_{0.25}$ | 5.94 | 4.35 | 171.91 |
| $FeTiCrAl_{0.50}Si_{0.50}$ | 5.89 | 5.10 | 184.90 |
| $FeTiCrAl_{0.25}Si_{0.75}$ | 5.85 | 5.21 | 189.43 |
| FeTiCrSi | 5.81 | 3.23 | 207.06 |
| **Other calc.**[9] | 5.81 | – | – |

(FM) and the paramagnetic (PM) states, we found that the former state has the lowest total energy, as summarized in Table.4.4. Based on the obtained result, the ferromagnetic phase is the most stable, indicating the ferromagnetic nature for the considered alloys. In addition, when comparing the obtained results with similar alloys analyzed previously [10, 11], our results show a clear similarity as they theoretically found that quaternary Heusler alloys (QHA) crystallize in the mentioned structure with a ferromagnetic character.

Moreover, since the systems under study have not been investigated theoretically or experimentally fabricated before apart from the parent compounds of Fe-based alloys, they thus need further authentication for structural stability. Therefore, we have determined the cohesive and formation energies ($E_c$ and $E_f$) in order to verify the materials' physical stability. The predicted values of these pivotal parameters are computed as follows [12]:

$$E_c = \left[E^{atom}_{K/Fe} + E^{atom}_{Mg/Ti} + E^{atom}_{N/Cr} + (1-x)E^{atom}_{O/Al} + xE^{atom}_{S/Si}\right] - E_{tot} \tag{4.3}$$

$$E_f = E_{tot} - \left[E^{bulk}_{K/Fe} + E^{bulk}_{Mg/Ti} + E^{bulk}_{N/Cr} + (1-x)E^{bulk}_{O/Al} + xE^{bulk}_{S/Si}\right] \tag{4.4}$$

The registered values of $E_c$ and $E_f$ of the parent materials and their doped systems are summarized in Table.4.4. From a theoretical point of view, the negative formation energy of the investigated alloys indicates that they are thermodynamically stable. In addition,

Table 4.4: The ground state energy $E_{tot}$ (eV), cohesive energy $E_c$(eV/atom), formation energy $E_f$(eV/atom) and Curie temperature $T_c$(K).

| Compound | $E_{tot}^{NM}$ | $E_{tot}^{FM}$ | $E_c$ | $E_f$ | $T_c$ |
|---|---|---|---|---|---|
| KMgNO | -25360.460 | -25360.87 | 2.61 | -4.28 | 862 |
| $KMgNO_{0.75}S_{0.25}$ | -110253.56 | -110255.06 | 2.54 | -4.35 | 722 |
| $KMgNO_{0.50}S_{0.50}$ | -119065.82 | -119067.32 | 2.48 | -3.94 | 722 |
| $KMgNO_{0.25}S_{0.75}$ | -127878.49 | -127879.98 | 2.44 | -3.94 | 722 |
| KMgNS | -34172.862 | -34173.264 | 2.35 | -3.49 | 733 |
| FeTiCrAl | -93033.66 | -93034.34 | 6.44 | -0.62 | 1290 |
| **Other calc.**[9] | – | -101299.87 | – | -0.31 | – |
| $FeTiCrAl_{0.75}Si_{0.25}$ | -373419.69 | -373421.73 | 6.55 | -0.74 | 985 |
| $FeTiCrAl_{0.50}Si_{0.50}$ | -374704.8 | -374706.38 | 6.64 | -0.86 | 722 |
| $FeTiCrAl_{0.25}Si_{0.75}$ | -375989.95 | -375991.04 | 6.74 | -0.99 | 525 |
| FeTiCrSi | -94318.856 | -94318.99 | 6.84 | -0.82 | 424 |
| **Other calc.**[9] | – | -102264.66 | - | -0.446 | - |

lower formation energy designates that the corresponding alloy is easier to be formed spontaneously during the growth process. As listed in Table.4.4, it is clear that the series of the studied alloys have a negative formation energy indicating their thermodynamic stability, and they can be achieved experimentally. In the same vein, the cohesive energy's recorded positive values validate the doped systems' physical stability.

Furthermore, in order to check the suitability of the systems under study in the spintronic applications, the Curie temperature $T_C$ of the investigated alloys was calculated using the mean field approximation (MFA), which has the following expression [13, 14]:

$$T_c = \frac{2\Delta E}{3K_B T} \tag{4.5}$$

Where $\Delta E$ is the difference in total energy between the paramagnetic and ferromagnetic states, and $K_B$ is the Boltzmann constant.

According to the last column of Table.4.4, for $KMgNO_{1-x}S_x$ alloys, the predicted values of $T_C$ can be expected to be 862 K, 722 K, 722 K, 722 K and 733 K for the concentrations x = 00, 0.25, 0.50, 0.75 and 01, respectively. While, for $FeTiCrAl_{1-x}Si_x$ materials, the registered values of $T_C$ reach 1296 K, 985 K, 722 K, 525 K and 424 K for the concentrations x = 00,

0.25, 0.50, 0.75 and 01, respectively. Besides, we note that the Curie temperature is observed to decrease with the increasing of Si concentration.

Kübler et al. [15], report that some $Co_2$-based Heusler compounds have a high Curie temperature, such as $Co_2MnSi$ (990 K), $Co_2MnSn$ (899 K) and $Co_2FeSi$ (1185 K). Hence, we can expect that $KMgNO_{1-x}S_x$ and $FeTiCrAl_{1-x}Si_x$ alloys are suitable for spintronic and magnetoelectronic devices. It should be noted that this parameter ($T_C$) of these materials has not been calculated before, hence why we hope to accomplish it experimentally.

On the other hand, figure.4.3 shows the variation of the optimized lattice parameter ($a_0$) and bulk modulus ($B_0$) as a function of S/Si concentration (x) for the alloys of interest together with that employing Vegard's law [16] and the linear composition dependency (LCD) for $a_0$a and $B_0$, respectively.

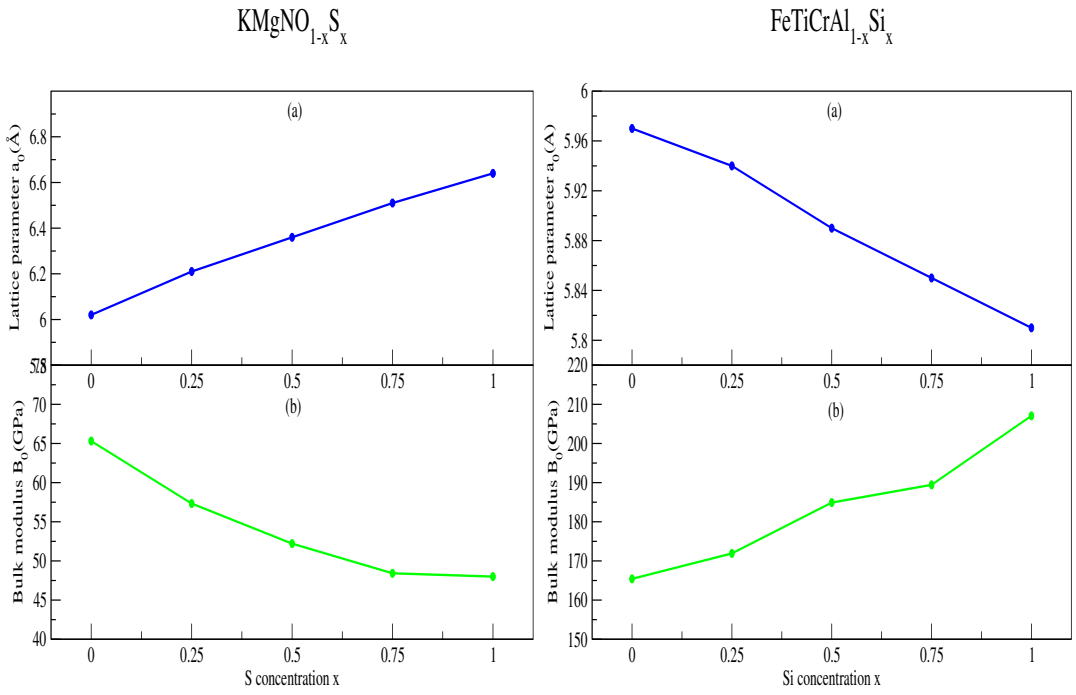


Figure 4.3: Variation of the calculated lattice parameter $a_0$ and bulk modulus $B_0$ versus S/Si concentration.

For the lattice parameter (Figure.4.3.a-c) we see a linear variation with the S and Si doped atom according to Vegard's law. While, for the bulk modulus (Figure4.3.b and d), we notice a slight deviation from the LCD. This law is only an approximate law and can be observed either in positive deviations or in negative deviations from linearity. In this context, it is clear that the lattice parameter increases with increasing x, whereas the bulk modulus decreases with increasing x for the alloys $KMgNO_{1-x}S_x$. While, for $FeTiCrAl_{1-x}Si_x$, one can observe a reverse behavior; $a_0$ decreases with increasing x, whereas $B_0$ increases with increasing Si concentration.

## 4.4 Mechanical properties

### 4.4.1 Introduction

It has become widely recognized that first-principle methods based on the DFT could be used to investigate the elastic characteristics of inorganic substances [17]. Any solid body subjected to external stresses, responds to a slight deformation, and this is known by elasticity. The applied stresses are described by tensors that determine the direction of the forces and the plane on which they are applied. The elastic moduli linearly relate the stress tensor to the strain tensor in the regime where Hooke's law applies.

### 4.4.2 Elastic properties

The elastic characteristics allow us to understand the response of crystals to external forces (shear, tension, compression, etc.) [18]. Therefore, the independent elastic constants $C_{ij}$, namely, $C_{11}$, $C_{12}$ and $C_{44}$, were computed for the compounds under consideration using IRELAST package implemented in the Wien2k code [19].

To calculate the coefficients $C_{11}$ and $C_{12}$, we apply an orthorhombic strain tensor with conserved volume. Furthermore, the incompressibility modulus for an isotropic cubic crystal is written as a function of $C_{11}$ and $C_{12}$ as follows:

$$B = \frac{1}{3}(C_{11} + 2C_{12}) \tag{4.6}$$

For the calculation of the elastic constant $C_{44}$, a monoclinic strain tensor with conserved volume is used. Furthermore, we recommend reference [20] for more details on strain tensors for a cubic crystal. These constants are tabulated in Table.4.5.

For the cubic system, the mechanical stability conditions of Born-Huang [21] are:

$$C_{11} - C_{12} > 0 \tag{4.7}$$

$$C_{12} > 0, C_{44} > 0 \tag{4.8}$$

$$(C_{11} + 2C_{12}) > 0 \tag{4.9}$$

$$C_{12} < B < C_{11} \tag{4.10}$$

It is clearly seen that the computed elastic constants fulfill the mechanical stability conditions of Born-Huang; this suggests that the series of $KMgNO_{1-x}S_x$ and $FeTiCrAl_{1-x}Si_x$ alloys

Table 4.5: Calculated elastic constants $C_{11}$, $C_{12}$, $C_{44}$ in GPa and melting temperature $T_m$(K).

| **Alloy** | | $C_{11}$ | $C_{12}$ | $C_{44}$ | $T_m$ |
|---|---|---|---|---|---|
| $KMgNO_{1-x}S_x$ | x=00 | 132.20 | 35.70 | 05.10 | 1334 |
| | x=0.25 | 105.20 | 34.80 | 04.30 | 1174 |
| | x=0.50 | 94.46 | 35.37 | 26.63 | 1111 |
| | x=0.75 | 95.50 | 24.20 | 03.40 | 1117 |
| | x=01 | 90.20 | 24.00 | 03.60 | 1086 |
| $FeTiCrAl_{1-x}Si_x$ | x=00 | 218.68 | 130.35 | 89.69 | 1845 |
| | **Other calc.**[9] | 264.20 | 109.00 | 107.30 | - |
| | x=0.25 | 231.15 | 134.22 | 140.63 | 1919 |
| | x=0.50 | 251.42 | 143.74 | 105.44 | 2039 |
| | x=0.75 | 273.26 | 160.37 | 98.79 | 2168 |
| | x=01 | 267.27 | 164.59 | 120.85 | 2133 |
| | **Other calc.**[9] | 271.00 | 168.00 | 114.20 | - |

at their optimized equilibrium lattice parameter are mechanically stable against elastic deformations. Besides, it is clear that the $C_{ij}$ magnitude of the doped systems $KMgNO_{1-x}S_x$ and $FeTiCrAl_{1-x}Si_x$ increases in the order $C_{44} < C_{12} < C_{11}$, except for $FeTiCrAl_{0.75}Si_{0.25}$. These findings signify that these alloys show higher resistance against unidirectional deformation than pure shear deformation. It is clearly seen that the elastic constants of $FeTiCrAl_{1-x}Si_x$ alloys (containing transition metals) are larger than those of the $d^0$ Heusler alloys $KMgNO_{1-x}S_x$ (containing no transition metals), signifying that the former are stiffer. Moreover, we notice that the computed elastic constants of the parent compound FeTiCrAl and FeTiCrSi are in accordance with the obtained values by R. Dhakal et al. [9].

Furthermore, the melting temperature ($T_m$) is related to the elastic constant $C_{11}$ and it is computed employing the following expression [22]:

$$T_m(K) = \left[553K + \left(\frac{5.91K}{GPa}\right) C_{11}\right] \tag{4.11}$$

The calculated melting temperatures are listed in the last column of Table.4.5. The melting temperatures range from 1086 K to 1334 K and 1845 K to 2168 K for $KMgNO_{1-x}S_x$ and $FeTiCrAl_{1-x}Si_x$, respectively. We note that $FeTiCrAl_{1-x}Si_x$ alloys have higher $T_m$ due to their higher elastic constant $C_{11}$ compared to that of $KMgNO_{1-x}S_x$ materials, proving the stiffness

of the Fe-based alloys compared to K-based alloys. Whereas, all of these alloys have a high melting temperature; hence, these materials can retain their crystal structure even at high temperatures.

To the best of our knowledge, these magnitudes have not been established for these alloys before; based on this, we hope that our calculations can be used to compensate for the lack of data on these compounds.

### 4.4.3 Mechanical parameters

Mechanical properties are an important criterion used to estimate and discuss the mechanical stability and to understand the mechanical behavior of the parent compounds KMgNZ (Z = O or S) and FeTiCrX (X = Al or Si) and their doped systems $KMgNO_{1-x}S_x$ and $FeTiCrAl_{1-x}Si_x$.

In this context, the mechanical parameters have been computed as the Young's modulus (E), shear modulus (G), bulk modulus (B), Poisson's ratio ($\nu$), anisotropic factor (A), Cauchy pressure $C_P$, Pugh's ratio (B/G) and the shear constant ($C'$), which are summarized in Table.4.6. These parameters are computed using the elastic constants $C_{ij}$ in the following Voigt-Reuss-Hill (VRH) approximations [23]:

$$E = \frac{9BG}{3B + G} \tag{4.12}$$

$$B = \frac{1}{3}(C_{11} + 2C_{12}) \tag{4.13}$$

$$G = \frac{1}{2}(G_V + G_R) \tag{4.14}$$

$$G_V = \frac{1}{5}(C_{11} - C_{12} + 3C_{44}) \tag{4.15}$$

$$G_R = \frac{5C_{44}(C_{11} - C_{12})}{4C_{44} + 3(C_{11} - C_{12})} \tag{4.16}$$

$$B = \frac{1}{3}(C_{11} + 2C_{12}) \tag{4.17}$$

$$\nu = \frac{3B - 2G}{2(3B + G)} \tag{4.18}$$

$$A = \frac{2C_{44}}{C_{11} - C_{12}} \tag{4.19}$$

$$C_P = C_{12} - C_{44} \tag{4.20}$$

$$C' = \frac{1}{2}(C_{11} - C_{12}) \tag{4.21}$$

Where $G_V$ and $G_R$ are Voigt's shear modulus and Reuss's shear modulus corresponding to the upper and lower bounds of G value, respectively.

Additionally, the calculated values of Young's (E), shear (G) and bulk (B) modulus of the studied alloys were estimated by adopting the Voigt, Reuss and Hill scheme using the elastic constants. Furthermore, Young's modulus (E) is an indication about the material stiffness, and it is a quantitative criterion of the resistance to elastic deformation caused by a mechanical load. Higher value of E for a given material, stiffer is the material. In light of the achieved outcomes, the obtained values are high, demonstrating the stiffness property of the alloys under study. Moreover, it is obvious that Young's moduli of $FeTiCrAl_{1-x}Si_x$ alloys are higher than that of $KMgNO_{1-x}S_x$ materials (about 3 times), hence the former are more stiffer than the latter.

Furthermore, shear modulus (G) is an indicator of the plastic deformation resistance. It is noted that the high G values found suggest that the materials are more resistant to volume compression than to shape change. We notice that the series of $FeTiCrAl_{1-x}Si_x$ have high values of G compared to $KMgNO_{1-x}S_x$ alloys, indicating that Heusler alloys containing transition metals are more resistant. Poisson's ratio ($\nu$) and Pugh's ratio are two factors that determine the materials nature.

Pugh and Frantsevich set a standard for determining the ductility or brittleness nature of materials [24, 25]. Apart from $FeTiCrAl_{0.75}Si_{0.25}$, the calculated values of $\nu$ and B/G ratio are higher than 0.26 and 1.75, respectively. Thus, the $FeTiCrAl_{0.75}Si_{0.25}$ alloy reflects a brittle nature, whereas all other alloys have a ductile character. Additionally, Poisson's ratio provides other information about the nature of the binding forces. For a typical ionic material, this coefficient is equal to 0.25 [26], whereas for a typical covalent bonding, its value is about 0.1. Poisson's ratio value for both materials is higher than 0.29 except for the $FeTiCrAl_{0.75}Si_{0.25}$ alloy. Hence the considered alloys reveal a high metallic character, whereas the $FeTiCrAl_{0.75}Si_{0.25}$ alloy is an ionic material. A pivotal parameter of the brittle/ductile feature and the chemical bonds nature of the materials is called Cauchy pressure ($C_P$). The positive value of this indicator suggests that this compound has a ductile character with a predominant metallic bonding; otherwise, it is expected to be brittle with a dominant

Table 4.6: Youngs modulus E(GPa), Shear modulus G(GPA), Bulk modulus B(GPa), Poisson's ratio $\nu$, anisotropic factor A, Cauchy pressure $C_P$(GPa), Pugh's ratio B/G, shear constant $C'$(GPa) and hardness $H_V$.

| **Compound** | E | G | B | $\nu$ | A | $C_P$ | B/G | $C'$ | $H_V$ |
|---|---|---|---|---|---|---|---|---|---|
| KMgNO | 60.48 | 22.38 | 67.86 | 0.34 | 0.11 | 30.60 | 3.03 | 48.25 | 2.35 |
| $KMgNO_{0.75}S_{0.25}$ | 32.74 | 11.64 | 58.27 | 0.37 | 0.12 | 30.50 | 3.49 | 35.20 | 2.45 |
| $KMgNO_{0.50}S_{0.50}$ | 71.30 | 27.76 | 55.07 | 0.28 | 0.90 | 8.74 | 1.98 | 29.54 | 4.45 |
| $KMgNO_{0.25}S_{0.75}$ | 30.16 | 10.81 | 47.97 | 0.39 | 0.09 | 20.80 | 2.94 | 35.65 | 2.40 |
| KMgNS | 41.55 | 15.39 | 46.07 | 0.34 | 0.11 | 20.40 | 2.99 | 33.10 | 1.83 |
| FeTiCrAl | 186 | 71.00 | 160 | 0.31 | 2.02 | 40.00 | 2.25 | 45.00 | 7.50 |
| **Other calc.**[9] | 236.51 | 94.25 | 160.69 | 0.25 | 1.38 | 1.70 | 1.70 | - | - |
| $FeTiCrAl_{0.75}Si_{0.25}$ | 258 | 104.0 | 167 | 0.24 | 2.90 | -6.41 | 1.60 | 48.46 | 14.4 |
| $FeTiCrAl_{0.50}Si_{0.50}$ | 220 | 84.80 | 180 | 0.29 | 1.96 | 38.30 | 2.11 | 53.84 | 8.16 |
| $FeTiCrAl_{0.25}Si_{0.75}$ | 216 | 81.85 | 198 | 0.31 | 1.75 | 61.58 | 2.41 | 56.44 | 6.36 |
| FeTiCrSi | 241 | 93.00 | 197 | 0.30 | 1.69 | 41.00 | 2.12 | 66.00 | 9.60 |
| **Other calc.**[9] | 218.95 | 82.96 | 202.31 | 0.32 | 2.22 | 53.80 | 2.44 | - | - |

covalent/ionic bonds. It is clear that Cauchy pressure is positive for the series of $KMgNO_{1-x}S_x$ and $FeTiCrAl_{1-x}Si_x$ alloys except $FeTiCrAl_{0.75}Si_{0.25}$. This result is corroborating with the predictable findings based on Poisson's ratio.

On the other side, in order to study the anisotropic character, the anisotropic factor (A) was calculated using Equation.(4.19). In general, if A = 1, the material is isotropic, otherwise, it behaves in an anisotropic manner. The obtained values show that A $\neq$ 1, hence all the materials under investigation are elastically anisotropic, which means that they possess a small probability to develop structural defects or micro-cracks during their growth process. Additionally, the shear constant explains the dynamical stability [27], if $C'$ is positive, the material has dynamical stability; otherwise, it is dynamically unstable. According to the calculated values listed in Table.4.6. It is obvious that $C'$ of the studied alloys is positive, hence they are dynamically stable. Furthermore, the hardness is a mechanical property that gives information about the elasticity, plasticity and resistance of materials. There are many models for calculating this property in the literature. In this study, Vicker's micro-hardness model is calculated using the following expression given by Tian et al. [28]:

$$H_V = 0.92 \left(\frac{G}{B}\right)^{1.137} G^{0.708} \tag{4.22}$$

Table.4.6 shows that the calculated values of the hardness are rather small for the studied systems; this is in good accordance with the values of G/B and G because a high hardness is associated with a high G/B ratio and G value. The hardness values show that $FeTiCrAl_{0.75}Si_{0.25}$ is the most stiffer ($H_V$ = 14.4), which is in good agreement with the higher values of Young's modulus (258 GPa) and shear ratio (104 GPa). For $KMgNO_{1-x}S_x$ alloys, as far as we know up to date, there are no experimental or theoretical results to compare our findings with. Accordingly, this finding could serve as a starting point for potential future research.

Further, for clear visualization and a perfect explanation of the anisotropy behavior of the mechanical moduli, it is recommended to study the elastic properties of the three-dimensional surfaces (3D). For the cubic structure (zinc blende phase), the crystallographic direction dependence of Young's modulus (E) [29], shear modulus (G) [30] and bulk modulus (B) are computed using a series of equations mentioned in Ref. [12].

The 3D plots of Young's, Poisson's, and shear moduli for $KMgNO_{1-x}S_x$ and $FeTiCrAl_{1-x}Si_x$ alloys are obtained using ELATE software [31]. These surfaces curves are illustrated in Figure.4.4 and Figure.4.5. The perfect shape of a sphere is correlated with the isotropic character of the compound, whereas the non-spherical shape is associated with the anisotropic character. It is obvious that the Young's, Poisson's, and shear moduli exhibit a significant degree of anisotropy by deviating significantly from the spherical form. The 3D curves of the surface of the mentioned mechanical moduli for the materials under investigation corroborate the anisotropic nature, which is predicted by the anisotropic factor (A).

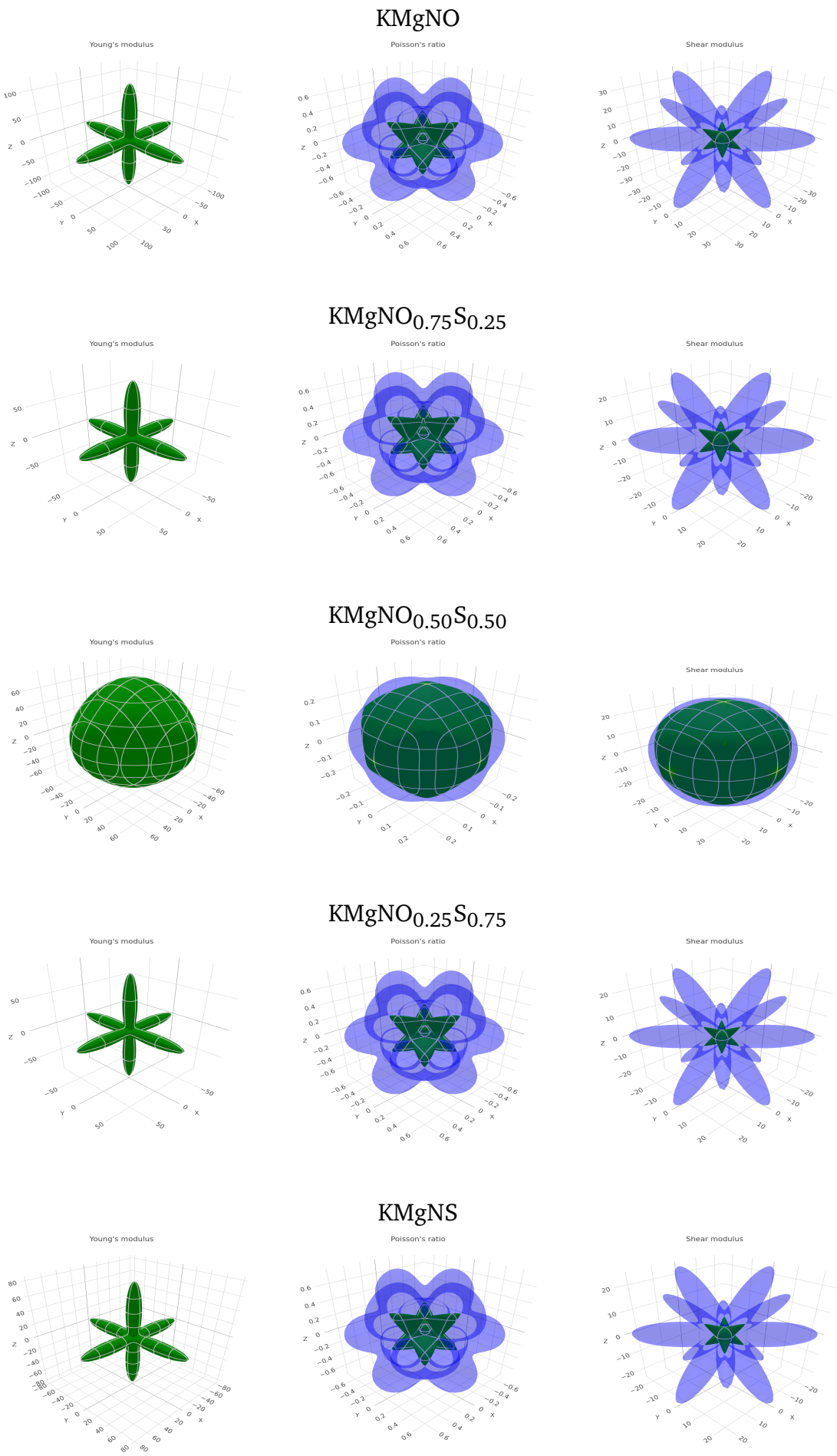


Figure 4.4: 3D surface of mechanical parameters of $KMgNO_{1-x}S_x$ alloys.

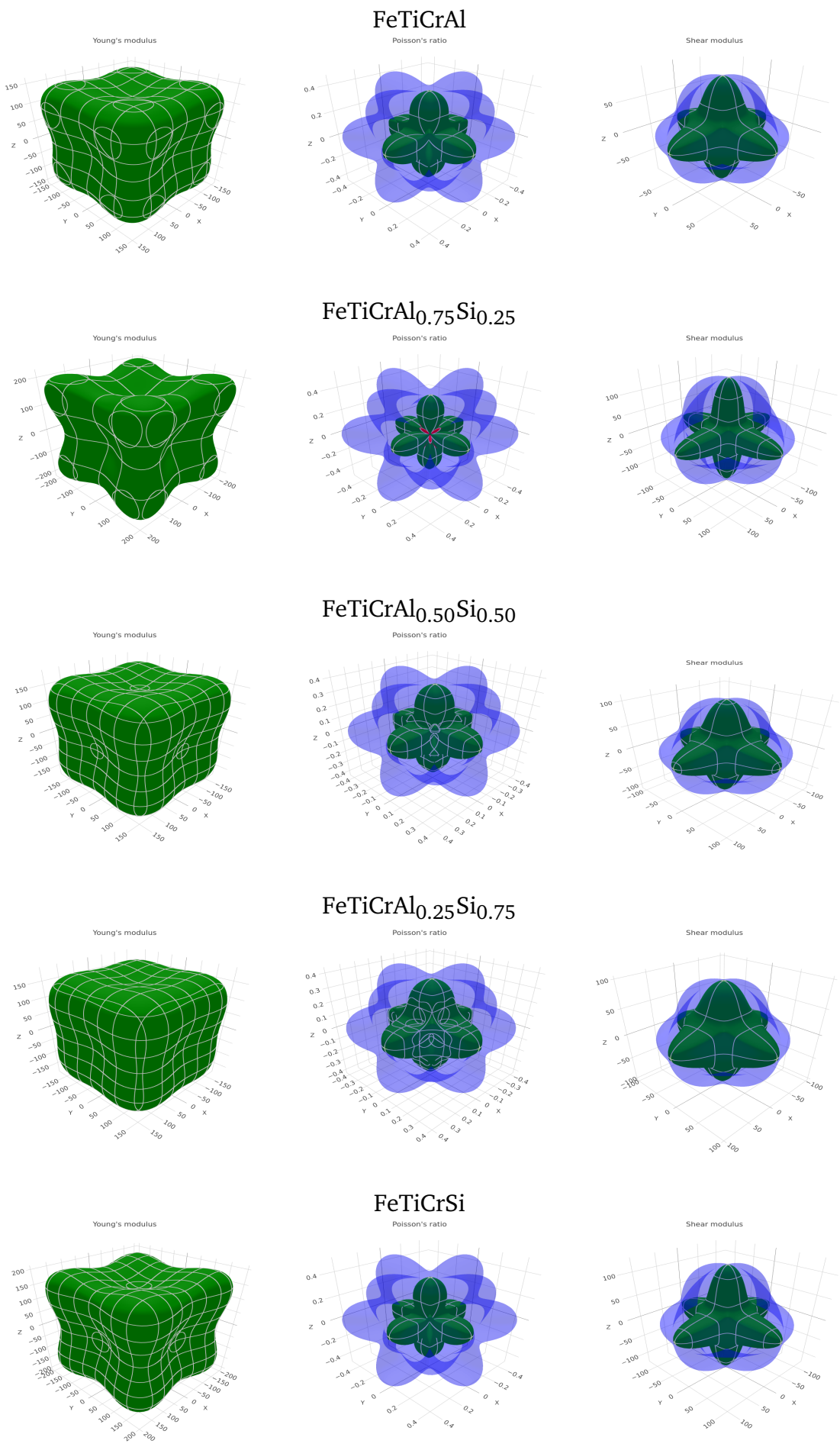


Figure 4.5: 3D surface of mechanical parameters of $FeTiCrAl_{1-x}Si_x$ alloys.

## 4.5 Electronic properties

### 4.5.1 Introduction

Before electronic or optoelectronic devices are realized, a basic examination of the electronic structure is conducted. The primary characteristics are first of all; the density of states (DOS) which specifies the contribution of each atom, then the band structure characterized by the energy value of the gap and finally the charge density, which reveals the type of crystalline bonding. The electronic structure of materials are decisive in determining Heusler alloys' magnetic characteristics and the half-metallic nature. Therefore, the calculation of electronic properties was performed using GGA, mBJ and GGA + U approximations at the equilibrium lattice parameter of the studied alloys $KMgNO_{1-x}S_x$ and $FeTiCrAl_{1-x}Si_x$.

It is important to emphasize that the mBJ approach is very accurate for the computing of band gaps, reliable, and closer to experimental values. Further, GGA and mBJ functional often yield good predictions, but when applied to tightly correlated electron systems, they were unable to yield an accurate orbital occupancy, accurate charge densities, or an insulating ground state. The GGA + Hubbard U (GGA + U) approach is created to get over the constraints. These errors can be overcome with the GGA + U technique by using a parameterized potential that uses a precise treatment of exchange interactions.
The GGA + U approach was applied to investigate the on-site correlation at the 3d transition metals. It is important to mention that the values of the parameter U are computed using the Quantum espresso package [6], and the obtained values are 5.00 eV, 3.75 eV and 4.68 eV for Fe, Ti and Cr atoms, respectively. These values of the Hubbard parameter for each atom are consistent with the computed values by R. Tesch et al. [32]. It is worth mentioning that it is unknown what values of the Hubbard parameter (U) are appropriate for the GGA + U approach; these values depend on the atomic species and its surroundings [33].

### 4.5.2 Band structures

A solid is a complex system that contains a large number of atoms and electrons. An atom has several distinct energy levels, an electron bound to this atom is necessarily in one of these levels. However, in a crystal structure, the energy levels of the independent atoms come together in the overall structure of the crystal to form energy bands, where these energy bands are called "allowed" energy bands that are separated by "forbidden" zones.

**Band structure $KMgNO_{1-x}S_x$ alloys:**

The band structures of $KMgNO_{1-x}S_x$ alloys using GGA and mBJ approaches are depicted in Figure.4.6.

The horizontal line (dashed line) set at zero represents the Fermi energy ($E_F$). For the spin up channels, there are no states at the $E_F$; in other words, this level is located in the forbidden band gap. Thus, the $KMgNO_{1-x}Si_x$ alloys with the configurations mentioned above reflect a typical of half-metallic ferromagnets (HMF) with 100% spin polarization, because the spin splitting among the spin up and spin down bands is clearly visible. It should be noted that the degree of spin polarization at the Fermi level was calculated by the following relationship [34]:

$$P\% = \frac{N\uparrow(E_F) - N\downarrow(E_F)}{N\uparrow(E_F) + N\downarrow(E_F)} \times 100 \tag{4.23}$$

$N\uparrow$ and $N\downarrow$ are the density of states at $E_F$ for the spin up and down, respectively. The difference between the bottom of the conduction band ($E_{CBM}$) and the maximum of the valence band ($E_{VBM}$) is commonly referred to as the gap energy ($E_g$). It is worth to mention that these gaps are essential to describe the stability of the half-metal (HM) magnetism [35, 36]. As shown in Figure.4.6, the parent compounds KMgNO and KMgNS exhibit indirect band gaps and display large gaps. The wide of these band gaps for $KMgNO_{1-x}Si_x$ alloys are summarized in Table.4.7. The energy band gap $E_g$ reaches the values 3.12 (6.00) and 2.01 (4.38) eV for KMgNO and KMgNS, respectively, using the GGA (mBJ) approach at their equilibrium lattice parameters. While the doped systems $KMgNO_{1-x}Si_x$ (x = 0.25, 0.50, and 0.75) reveal direct band gaps ( $\Gamma \longrightarrow \Gamma$), and their energy band gap $E_g$ fluctuates between 3.12 (6.00) and 2.01 (4.31) eV employing GGA (mBJ) approximation.

Table 4.7: Calculated energy band gap (in eV) and the degree of spin polarization for $KMgNO_{1-x}S_x$ Heusler alloys.

| **Compound** | $E_g$(GGA) | $E_g$(mBJ) | $E_g$(GGA + U) | Type of Gap | Spin Polar. |
|---|---|---|---|---|---|
| KMgNO | 3.12 | 6.00 | - | $X \longrightarrow \Gamma$ | 100% |
| $KMgNO_{0.75}S_{0.25}$ | 2.47 | 4.91 | - | $\Gamma \longrightarrow \Gamma$ | 100% |
| $KMgNO_{0.50}S_{0.50}$ | 2.67 | 4.60 | - | $\Gamma \longrightarrow \Gamma$ | 100% |
| $KMgNO_{0.25}S_{0.75}$ | 2.12 | 4.31 | - | $\Gamma \longrightarrow \Gamma$ | 100% |
| KMgNS | 2.01 | 4.38 | - | $X \longrightarrow \Gamma$ | 100% |

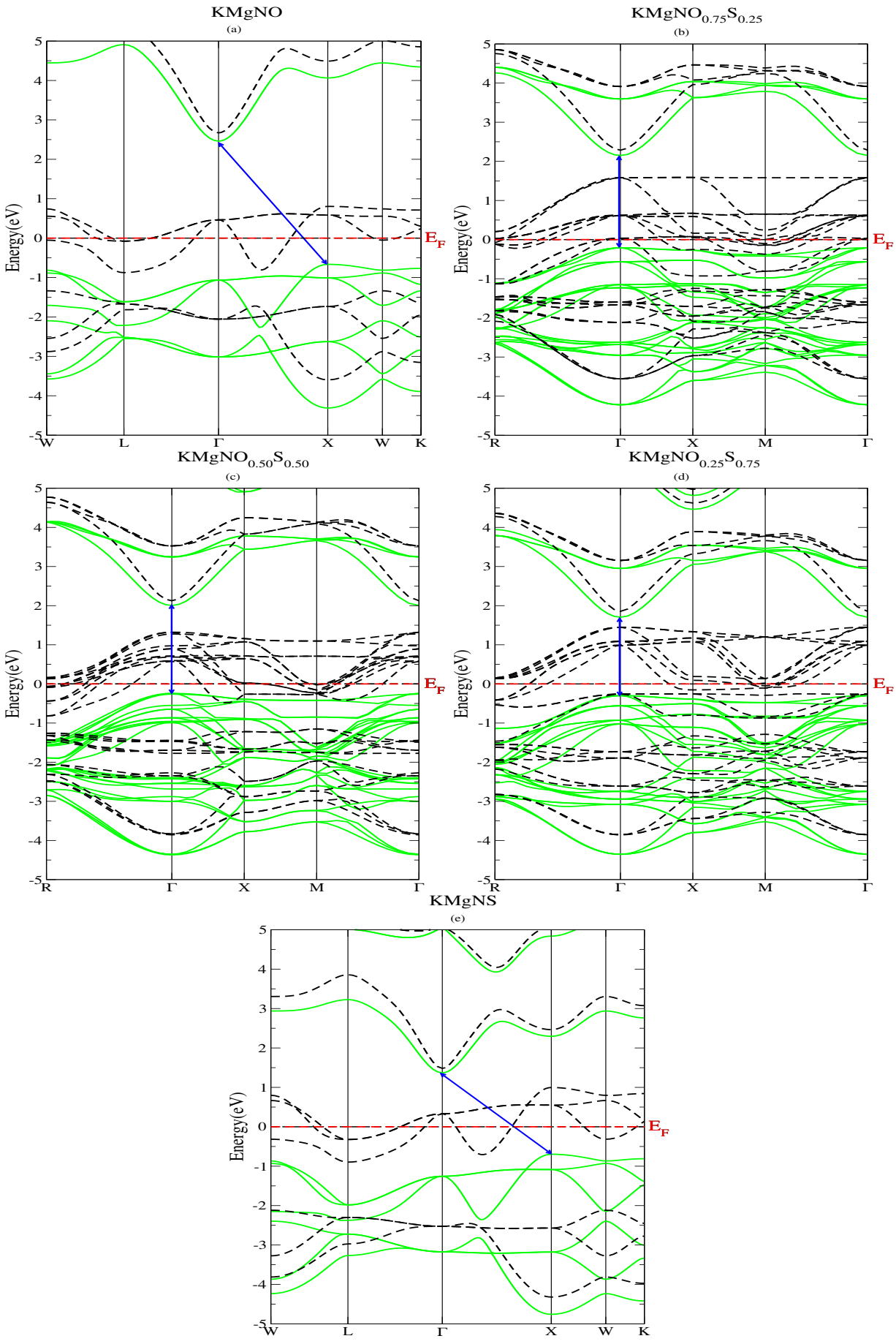


Figure 4.6: Band structures of $KMgNO_{1-x}S_x$ for spin up (solid line) and spin down (dashed line).

**Band structure** $FeTiCrAl_{1-x}Si_x$ **alloys:**

Figure.4.7 shows the calculated band structures of $FeTiCrAl_{1-x}Si_x$ Heusler alloys at their stable ferromagnetic phase using GGA approximation.

The Fermi energy ($E_F$) is represented by the horizontal line (dashed line) with zero. For the FeTiCrAl alloy (Figure.4.7-a), it is clear that the Fermi level for the spin up (solid line) and down (dashed line) bands is situated in the forbidden band gap since there are no states at this level, reflecting the semiconducting character of this compound. For x = 0.25, 0.50, 0.75 and 01 systems, the semiconducting character is revealed because the Fermi level is found in the forbidden zone for the spin up states. While it crosses the spin down states, hence these states have a metallic character. Thus, the (x = 0.25, 0.50, 0.75 and 01) alloys reflect a typical half-metallic ferromagnet (HMF). The computed energy gap for both FeTiCrAl and FeTiCrSi compounds and their doped alloys is quoted in Table.4.8, together with other theoretical results for comparison.

Table 4.8: Calculated energy band gap (in eV) and the degree of spin polarization for $FeTiCrAl_{1-x}Si_x$ Heusler alloys.

| **Compound** | $E_g$(GGA) | $E_g$(mBJ) | $E_g$(GGA + U) | Type of Gap | Spin Polar. |
|---|---|---|---|---|---|
| $FeTiCrAl^{\uparrow}$ | 0.76 | 0.61 | 0.95 | $\Gamma \longrightarrow \Gamma$ | - |
| $FeTiCrAl\downarrow$ | 00 | 0.61 | 0.57 | $L \longrightarrow W$ | 100% |
| $FeTiCrAl_{0.75}Si_{0.25}$ | 0.40 | 0.70 | 0.97 | $\Gamma \longrightarrow \Gamma$ | 100% |
| $FeTiCrAl_{0.50}Si_{0.50}$ | 0.71 | 0.96 | 0.58 | $\Gamma \longrightarrow \Gamma$ | 100% |
| $FeTiCrAl_{0.25}Si_{0.75}$ | 0.53 | 0.86 | 1.25 | $\Gamma \longrightarrow \Gamma$ | 100% |
| FeTiCrSi | 0.91 | 0.91 | 1.52 | $\Gamma \longrightarrow \Gamma$ | 100% |

It is evident that the electronic and magnetic properties are greatly improved by the DFT + U function, which accounts for the on-site Coulomb interaction [37]. Moreover, It is found that the parameter U opens the spin up channels' energy gap. In general, when U is added to the DFT (GGA), the band gap widens, and this is in good agreement with our results for almost all the specimens except $FeTiCrAl_{0.50}Si_{0.50}$. Also, one can notice that the estimated energy gap for the spin down of this compound is about 0.61 (0.57) eV using mBJ (DFT + U), while this gap is absent using GGA functional. For (x = 0.25, 0.50, 0.75 and 01), according to the band structures along the high-symmetry directions in the first Brillouin zone utilizing the aforementioned approaches, each material has a direct band gap (the upper of VB and bottom of CB are situated at the point $\Gamma$). In the case of the FeTiCrAl alloy (x = 00), the bottom of CB occurs at the W point, and the top of VB locates at the L point, resulting in an

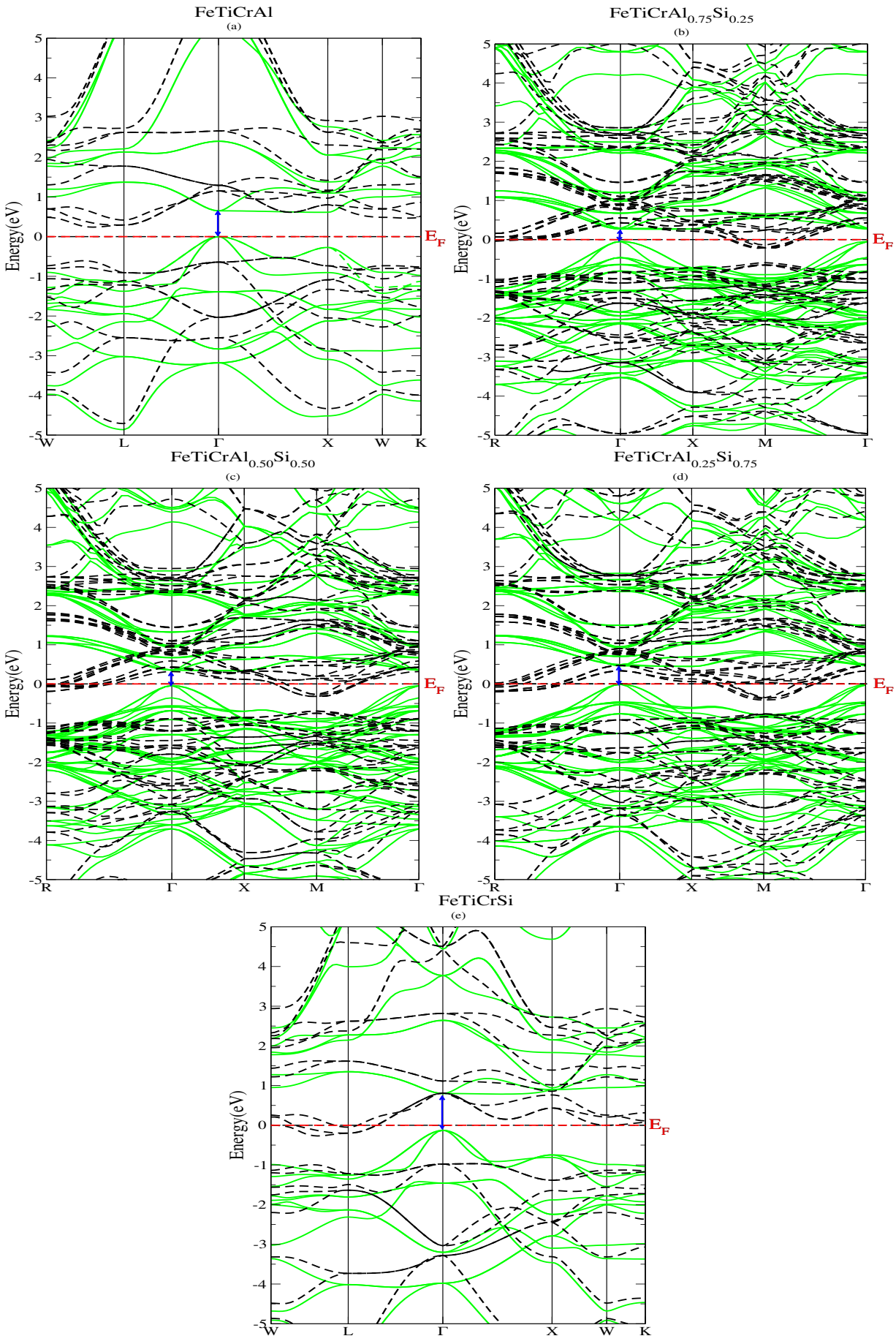


Figure 4.7: Band structures of $FeTiCrAl_{1-x}Si_x$ for spin up (solid line) and spin down (dashed line).

indirect band gap (L $\longrightarrow$ W) for the spin down channels. As depicted in Table.4.8, apart from FeTiCrAl alloy, we notice that the spin polarization in the considered alloys $FeTiCrAl_{1-x}Si_x$ is 100%, which designates their half-metallic feature and nominates them as spin injection materials.

### 4.5.3 Density of states

In order to determine the contribution from each element, we have calculated the total and partial density of states (DOS/PDOS) for $KMgNO_{1-x}S_x$ and $FeTiCrAl_{1-x}Si_x$ alloys at the most stable phase (type I) with their ferromagnetic feature.

**Density of states $KMgNO_{1-x}S_x$ alloys:**

The plots of the density of states for $KMgNO_{1-x}S_x$ alloys using GGA and mBJ approximations are presented in Figure.4.8.

It can be seen that the general shape of the DOS for these alloys is slightly similar. In addition, the DOS and PDOS confirm that the spin up states for the inspected $d^0$ Heusler alloys exhibit a semiconductor character, while the spin down states manifest a metallic character. Furthermore, the electrons were totally polarized at the Fermi level, and this situation resulted in 100% spin polarization. Thus, these results are consistent with the data of band structures. We note that in the spin up and down states, a five peaks structure is identified. These peaks are dominantly arising from the contribution of spin up and down bonding and anti-bonding states of K, Mg, N and Z (O and S) atoms. These bonding and anti-bonding states are separated by the energy band gap. In addition, one can notice that the patterns of spin splitting of N and Z (O and S) atoms are identical, demonstrating ferromagnetic (FM) couplings between these atoms. The N-p and Z-p states contribute mostly to the formation of the valence band peaks. Meanwhile, the peaks of the spin up channels of the conduction band are originated mainly by the contributions of empty d states of the K atom and with a small contribution of Mg-s states for the parent compounds and the doped system. Moreover, we notice that the contribution of O atom in the doped alloys for the concentrations x = 0.25 and 0.50 is higher than that of the S atom for the spin up and the spin down channels. Moreover, whereas the six bands in the spin down states are partially filled, the six bands in the spin up channels are entirely filled (valence band). We also found that the spin polarization is mainly due to the p-p bonding hybrids near the Fermi level. Conversely, the d(s) states of K and Mg atoms (cations) did not play an important role in the formation of the magnetism because they are slightly occupied. While the 2(3)-p states of N and Z atoms (anions) are

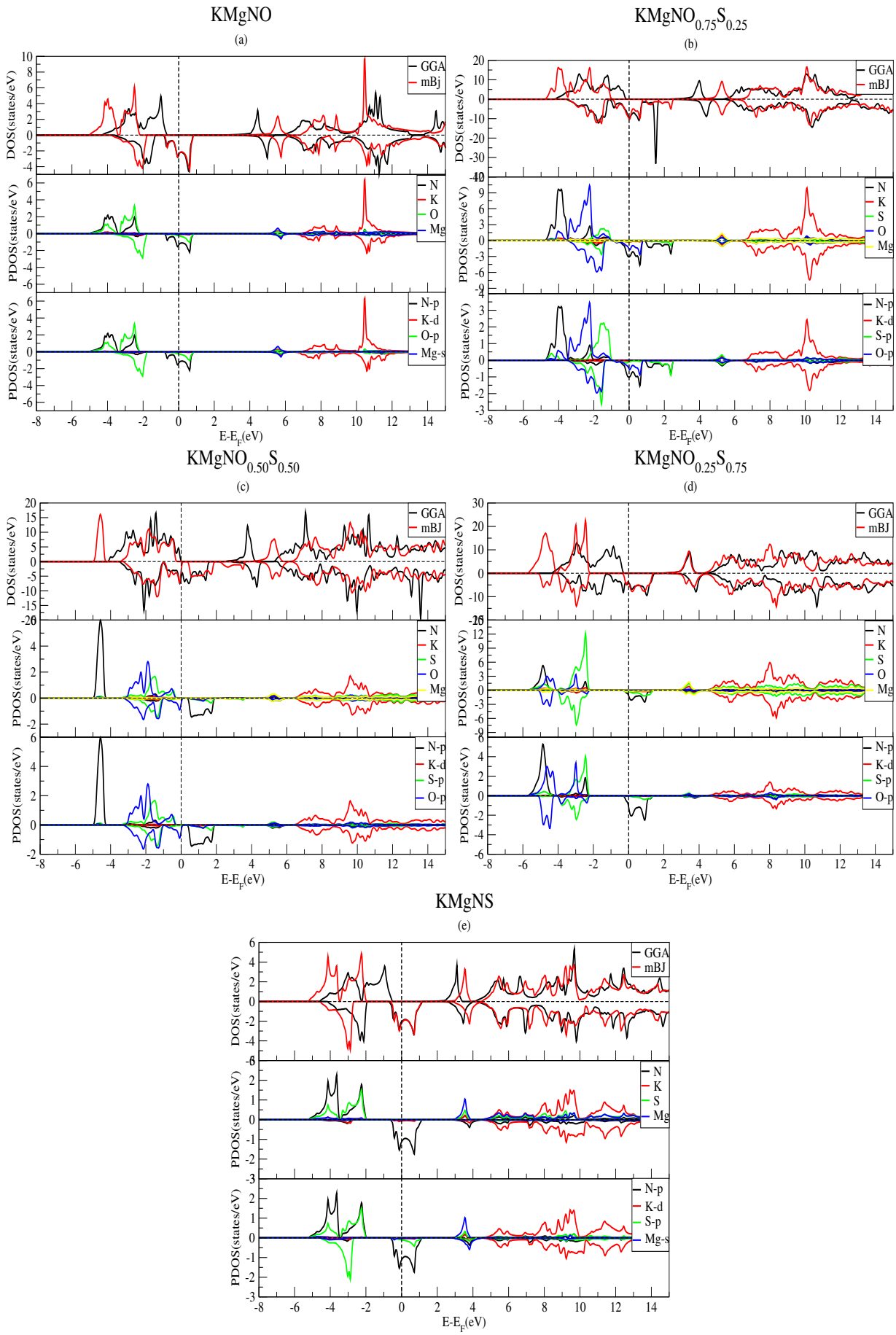


Figure 4.8: DOS structures of $KMgNO_{1-x}S_x$ for spin up (solid line) and spin down (dashed line).

fully occupied. As a result, the magnetism of these half-metallic alloys is widely provoked by p states of the anions. In addition, K. Kusakabe et al. and Sieberer et al. [38, 39] describe the magnetism of materials by the so-called flat band produced by the anionic p orbitals , therefore, our results are in agreement with their explanation. It is worth to mention that the gaps amounts of the considered alloys are higher than those of quaternary Heusler alloys including transition metals [40]. While they are comparable with those of quaternary alloys including only $d^0$ elements [41, 42]. This affirms that the half-metallic feature has been improved in non-containing transition elements Heusler alloys. Moreover, it is evident that the spin up states are shifted away from Fermi level when using the mBJ compared to the GGA approximation; this explains the increase in the value of $E_g$ for these alloys. It is worth to mention that the formation of the band gap in HM Heusler materials can be distributed either through: i) charge transfer, ii) covalent bond, or iii) d-d hybridization [43]. In the case of sp Heusler compounds and according to the partial DOS of the elements of KMgNZ, the p-p hybridization between the anionic atoms (N and Z) is dominant and hence accountable for the energy gap. Stated otherwise, in the spin up channel, the N/Z atoms' bonding states were primarily located in the energy range [-5; -1 eV]. While, the antibonding states of the N/Z atoms were mainly located in the energy range [0; 6 eV], and therefore, the corresponding bonding-antibonding states led to the formation of an energy band gap. While the s-p hybridization of cationic atoms (K and Mg) with anionic atoms is negligible. To clarity, the non-metals elements (N, O, and S) are the most electronegative constituents when compared to their associates (K and Mg). These atoms need five electrons to complete their octets provided by K and Mg (s-electrons). Consequently, the latter atoms contribute the least to the band formation at the Fermi level, as demonstrated by the N-p and Z-p states in the partial density of states (PDOS). These results confirm that the considered materials reveal a HM ferromagnetic property.

**Density of states** $FeTiCrAl_{1-x}Si_x$ **alloys:**

The curves of the total and partial densities of states (TDOS and PDOS) for the investigated alloys are displayed in Figure.4.9.

It is noteworthy that the spin up states of $FeTiCrAl_{1-x}Si_x$ alloys is semiconductive. A similar behavior is reflected by the spin down state of the FeTiCrAl alloy, unlike that of FeTiCrSi, which manifests a metallic feature. To put it clearly, we can nominate FeTiCrAl alloy as a semiconductor material, and this character is consistent with the earlier ab initio investigation by R. Dhaka et al. [9]. While (x = 0.25, 0.50, 0.75 and 01) alloys have a half-metallic

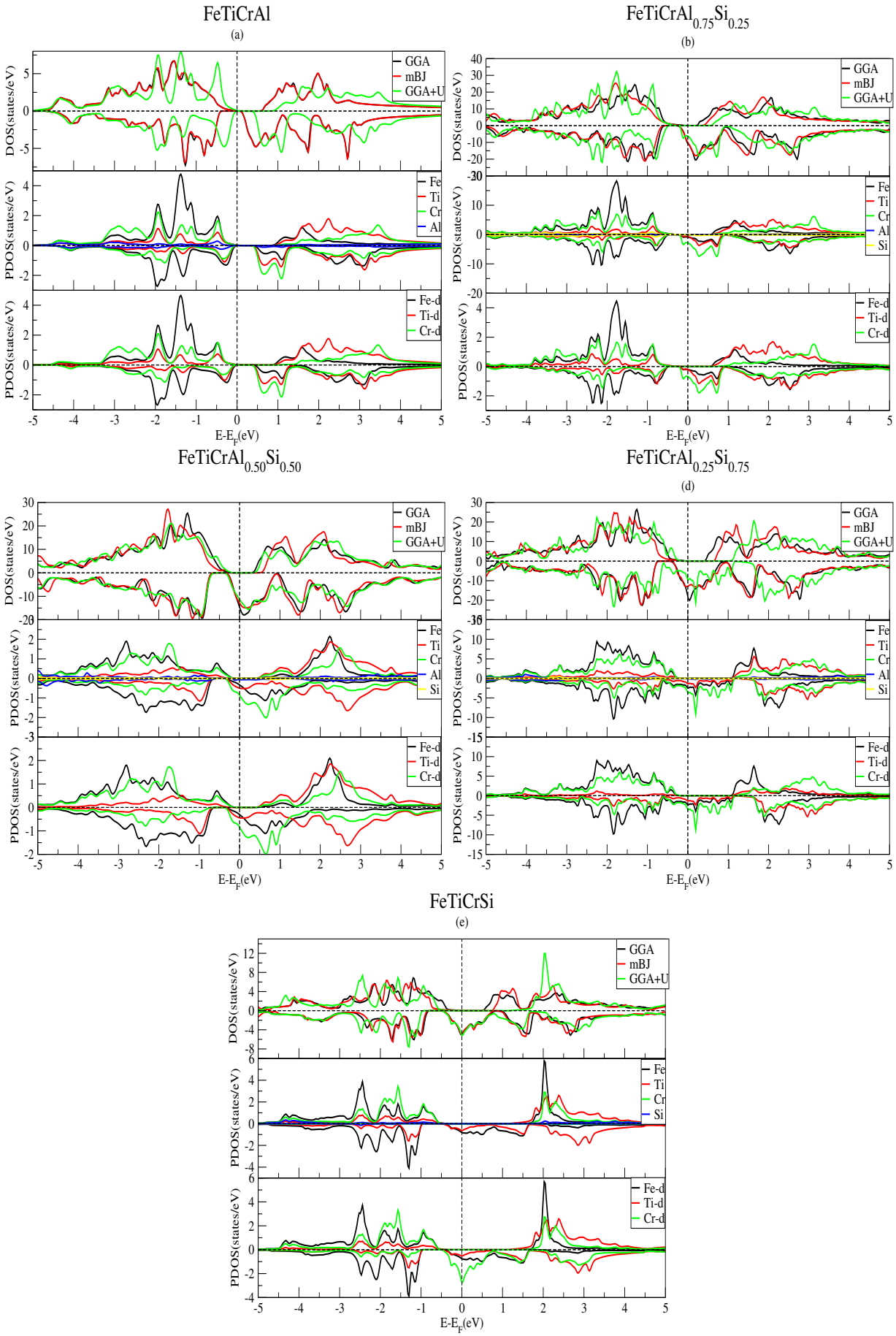


Figure 4.9: DOS structures of $FeTiCrAl_{1-x}Si_x$ for spin up (solid line) and spin down (dashed line).

behavior at their equilibrium state, and this result is consistent with the data of the band structures. In addition, PDOS plays a crucial part in figuring out each atom's contribution. It is clear that the peaks in the valence band (VB) of all systems are dominantly arising from the contribution of the d orbitals of Fe and Cr atoms; these orbitals dominate the bottom of valence band between -3 and -0.5 eV for the spin up and spin down states. The transition metals' d orbitals in the conduction band (CB) are primarily responsible for the PDOS for the spin up and down channels. Additionally, the d-states of the transition elements (Fe, Ti and Cr) are making metallic intersection at $E_F$ in the spin down configuration, resulting in the half-metallic nature of (x = 0.25, 0.50, 0.75 and 01) alloys. It should be noted that the creation of the bonding and anti-bonding states is not significantly influenced by the main group elements (Al and Si) of the inspected quaternary Heusler alloys. These bonding and anti-bonding states are separated by the energy band gap; this latter is originated due to the strong d-d hybridization between the orbitals, which accounts for the splitting.

## 4.6 Magnetic properties

### 4.6.1 Introduction

Heusler alloys have interesting magnetic properties due to their transition metals. The quaternary Heusler alloys with the configuration mentioned above showed a ferromagnetic property, and this motivated us to go further by exploring the magnetic properties. The magnetic feature in materials arises due to the orbital and rotational motions of the electron and depends on the alignment of the elements in a unit cell; a slight disturbance in the crystal structure can significantly change this parameter. It is important to note that the total magnetic moment is not only the combination of the partial magnetic moments but also the effect of the magnetic moment of the interstitial spaces between the atom sites where the wave functions are developed as plane waves. Any deviation from Heusler stoichiometry or small changes in the Heusler phase can greatly affect the magnetic properties of the alloys.

### 4.6.2 Magnetic moment of $KMgNO_{1-x}S_x$ alloys

In this study, we have calculated the total and partial magnetic moments of $KMgNO_{1-x}S_x$ alloys ($0 \leq x \leq 1$) using GGA and mBJ approximations, and the results are codified in Table.4.9.

We note that the total magnetic moment is an integer for the studied $KMgNO_{1-x}S_x$ alloys in the FM state and equal to 2 $\mu_B$ for each of them, indicating good agreement with

Table 4.9: Total magnetic moment $M_{tot}$, interstitial magnetic moment $M_{int}$, partial magnetic moment $M_K$, $M_{Mg}$, $M_N$, $M_O$ and $M_S$ in $\mu_B$ for $KMgNO_{1-x}S_x$ alloys.

| x | approach | $M_{tot}$ | $M_{int}$ | $M_K$ | $M_{Mg}$ | $M_N$ | $M_O$ | $M_S$ |
|---|---|---|---|---|---|---|---|---|
| x=00 | GGA | 02 | 0.18 | 0.02 | -0.02 | 1.25 | 0.58 | - |
| | mBJ | 02 | -0.09 | -0.01 | -0.07 | 1.55 | 0.62 | - |
| x=0.25 | GGA | 02 | 0.25 | 0.02 | -0.02 | 0.90 | 0.44 | 0.57 |
| | mBJ | 02 | 0.07 | 0.00 | -0.03 | 0.92 | 0.47 | 0.45 |
| x=0.50 | GGA | 02 | 0.31 | 0.03 | -0.01 | 1.32 | 0.20 | 0.43 |
| | mBJ | 02 | 0.12 | 0.01 | -0.02 | 1.50 | 0.19 | 0.37 |
| x=0.75 | GGA | 02 | 0.03 | 0.02 | -0.02 | 1.70 | -0.00 | 0.45 |
| | mBJ | 02 | 0.01 | 0.00 | -0.02 | 1.90 | -0.01 | 0.31 |
| x=01 | GGA | 02 | 0.35 | 0.01 | -0.03 | 1.41 | - | 0.26 |
| | mBJ | 02 | 0.14 | -0.00 | -0.07 | 1.69 | - | 0.24 |

similar $d^0$ quaternary Heusler alloys [44]. It is clear that N, O and S atoms for the parent compounds KMgNZ (Z = O or S) and their doped systems have the main contribution in the total magnetic moment. While K and Mg atoms have a slight contribution, $M_K < 0.03\mu_B$ and $M_{Mg} < -0.01\mu_B$ for all alloys. The opposite sign between the partial magnetic moments of K, N, Z and Mg atoms reveals that their electrons in the valence band interact in an antiferromagnetic (AFM) manner. In addition, it is clear that the total magnetic moment verified the Slater-Pauling rule of the studied Heusler alloys [45], which is expressed in the following expression:

$$M_{tot} = (N_{\uparrow} - N_{\downarrow}) = (2N_{\uparrow} - Z_t) \tag{4.24}$$

Where $Z_t$ represents the total number of valence electrons [46]. To clarify, KMgNZ quaternary Heusler alloys have 14 valence electrons in the unit cell (1 from K, 2 from Mg atom, 5 from N atom, and 6 from (Z= O or S) atom. According equation 4.24 the $M_t$ is equal to 2 $\mu_B$ for the considered quaternary Heusler alloys, which are in a good agreement with the results of Table.4.9, as expected, for the considered quaternary Heusler alloys exhibit an integer magnetic moment.

Furthermore, Figure.4.10 represents the local magnetic moments on the K, Mg, N, O and S atoms, for the studied alloys , as well as the total magnetic moments, which are given per unit cell as a function of the concentration.

It is clearly seen that S concentration does not effect the total magnetic moment; it reaches the value $M_{tot} = 2\mu_B$ for all alloys. While we notice that concentration effects the local magnetic moment of the anionic atoms (N, O and S), whereas this effect is negligible for the

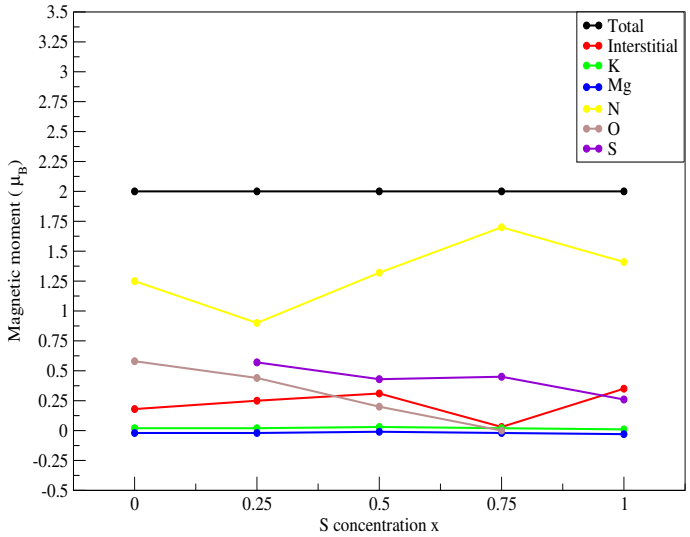


Figure 4.10: Total and partial magnetic moment of $KMgNO_{1-x}S_x$ alloys versus S concentration.

cationic elements (K and Mg). In addition, the nitrogen (N) atom always plays an important role in the total magnetic moment of the alloys under investigation $KMgNO_{1-x}S_x$.

### 4.6.3 Magnetic moment of $FeTiCrAl_{1-x}Si_x$ alloys

Table.4.10 contains the computed total and partial magnetic moment values for the materials being studied.

It is obvious that the Fe and Cr atoms contribute the most to the total magnetic moment. While, for any concentration x, the magnetic moment of the Al and Si atoms is very small, leading to a negligible contribution to the total magnetic moment. The anti-parallel behavior between the partial magnetic moments of Fe/Cr and Ti/Al/Si atoms reveals that their electrons in the valence band interact in an antiferromagnetic (AFM) manner, affirming the ferrimagnetic arrangement of our materials in LiMgPdSn structure at their equilibrium lattice parameter. It is noteworthy that the presence of the magnetic moment is shown by the difference in state densities between spin up and spin down configurations. In addition, the detailed explanation of the origin of the magnetism of Heusler alloys is very complicated, but their magnetic moments vary regularly according to their number of valence electrons and their crystal structures following the generalized Slater-Pauling rule [48], expressed as follows:

$$M_{tot} = |Z_t - 24| \tag{4.25}$$

Where $Z_t$ represents the total number of valence electrons. The quaternary Heusler al-

Table 4.10: Total magnetic moment $M_{tot}$, interstitial magnetic moment $M_{int}$, partial magnetic moment $M_{Fe}$, $M_{Ti}$, $M_{Cr}$, $M_{Al}$ and $M_{Si}$ in $\mu_B$ for $FeTiCrAl_{1-x}Si_x$ alloys.

| **x** | approach | $M_{tot}$ | $M_{int}$ | $M_{Fe}$ | $M_{Ti}$ | $M_{Cr}$ | $M_{Al}$ | $M_{Si}$ |
|---|---|---|---|---|---|---|---|---|
| | GGA | 03 | 0.31 | 0.62 | -0.20 | 2.27 | -0.01 | - |
| | **other calc.**[47] | 03 | - | 0.65 | -0.38 | 2.89 | - | - |
| x=0.00 | mBJ | 03 | 0.28 | 0.62 | -0.20 | 2.31 | -0.01 | - |
| | GGA + U | 03 | 0.28 | 1.14 | 0.18 | 1.39 | 0.00 | - |
| | GGA | 2.75 | 0.12 | 0.62 | -0.21 | 2.26 | -0.03 | -0.02 |
| x=0.25 | mBJ | 2.75 | 0.09 | 0.62 | -0.25 | 2.34 | -0.03 | -0.04 |
| | GGA + U | 2.75 | 0.23 | 1.13 | 0.11 | 1.30 | 0.01 | -0.03 |
| | GGA | 2.50 | 0.12 | 0.62 | -0.22 | 2.01 | -0.03 | -0.02 |
| x=0.50 | mBJ | 2.50 | 0.11 | 0.62 | -0.3 | 2.09 | -0.04 | -0.03 |
| | GGA + U | 2.50 | 0.19 | 0.80 | -0.20 | 1.76 | -0.02 | -0.01 |
| | GGA | 2.25 | 0.11 | 0.61 | -0.18 | 1.75 | -0.01 | -0.03 |
| x=0.75 | mBJ | 2.25 | 0.10 | 0.64 | -0.21 | 1.81 | -0.02 | -0.04 |
| | GGA + U | 2.25 | 0.21 | 0.83 | 0.01 | 1.21 | 0.02 | -0.01 |
| | GGA | 02 | 0.08 | 0.61 | -0.19 | 1.52 | - | -0.02 |
| | **other calc.**[47] | 02 | - | 0.65 | -0.30 | 1.75 | - | - |
| x=01 | mBJ | 02 | 0.06 | 0.64 | -0.2 | 1.58 | - | -0.03 |
| | GGA + U | 02 | 0.25 | 0.34 | -0.11 | 1.73 | - | -0.00 |

loys FeTiCrAl and FeTiCrSi in their equilibrium lattice parameter have 21 and 22 valence electrons ($Z_t$), respectively. To put it clearly, the spin up channels are fully filled by 16 electrons, whereas the spin down channels are partially filled with 5 electrons for FeTiCrAl and 6 electrons for FeTiCrSi. Thus, the total magnetic moment of the parent materials at hand has an integer value (3 $\mu_B$ for FeTiCrAl and 2 $\mu_B$ for FeTiCrSi), obeying the Slater-Pauling rule mentioned above. This result is in accordance with the obtained theoretical results predicted previously in Ref [9, 47, 49]. For $FeTiCrAl_{1-x}Si_x$ alloys (x = 0.25, 0.50 and 0.75), it is observed that the total magnetic moments do not agree with the Slater Pauling rule. This trend is similar to the work done on the Fe-based alloys; the work of S. S. Pedro et al. [50] expressed the disagreement between the values of $Fe_2MnSi_{1-x}Ca_x$ total magnetic moment calculated experimentally and those calculated by the Slater-Pauling rule. These discrepancies can be attributed to a partial atomic disorder in the structure. It is worth noting that all results of the magnetic moments for the studied systems are calculated by different GGA, mBJ and GGA + U approximations, and they all gave the same values of the total magnetic moments. Whereas, each atom's local magnetic moment is affected by the used approximation (GGA, mBJ or GGA + U).

In Figure.4.11, we present the local magnetic moments on the Fe, Ti, Cr, Al and Si atoms

for the alloys, as well as the total magnetic moments, which are given per unit cell as a function of the concentration. It should be noted that the magnetic moment decreases linearly with the concentration of silicon (Si), from 3 for FeTiCrAl to 2 for FeTiCrSi alloy. In addition, we observe a similar trend for the chromium (Cr) atom, while the concentration does not greatly affect the local magnetic moment of the other elements. Thereby, the chromium atoms play an important role in the total magnetic moment of the investigated alloys.

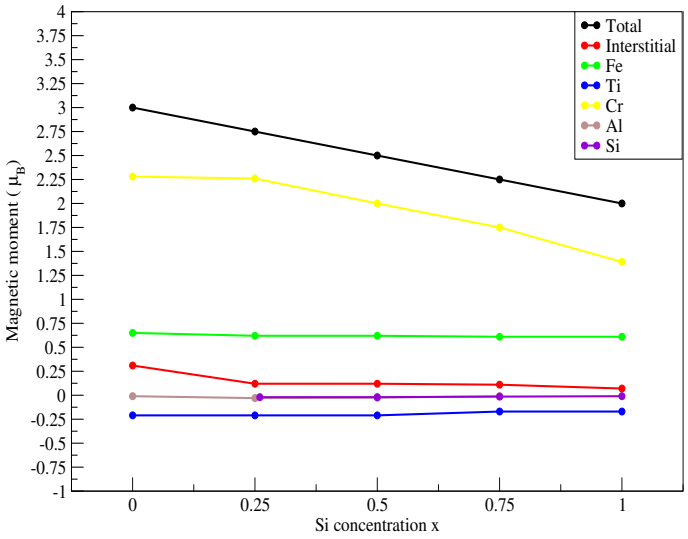


Figure 4.11: Total and partial magnetic moment of $FeTiCrAl_{1-x}Si_x$ alloys versus Si concentration.

## 4.7 Thermodynamic properties

### 4.7.1 Introduction

In addition to the investigations we conducted on materials, studying thermodynamic properties seems inevitable. For this purpose, we used the quasi-harmonic Debye model, which addresses the effect of materials under various conditions, such as high pressures and high temperatures.

In quantum mechanics, phonons are the equivalent of a particular category of vibrational movements known as normal modes of vibration in classical mechanics. A normal mode of vibration is one in which each element of a lattice vibrates at the same frequency. These modes are of great importance, particularly because any vibrational movement in a solid can be represented as the superposition of a certain number of normal modes of vibration with different frequencies ($\nu$). They can be understood as the fundamental vibrations of the lattice, where each atom within it can be viewed as a harmonic oscillator [51].

### 4.7.2 Quasi-harmonic Debye model

In order to study and determine the behavior of $KMgNO_{1-x}S_x$ and $FeTiCrAl_{1-x}Si_x$ alloys under varied temperature and pressure at the ferromagnetic phase, we have calculated their thermal properties using the quasi-harmonic Debye model implemented in the Gibbs program [52]. This model allows us to obtain all thermodynamic quantities from the calculated (volume-energy) points, in which the non-equilibrium Gibbs function $G^*(V, P, T)$ is expressed as follows:

$$G^*(V, P, T) = E(V) + PV + A_{vib}\left[\theta_D(V), T\right] \tag{4.26}$$

Herein, E(V), PV and $\theta_D$ represent the total energy per unit cell, the hydro-static pressure and Debye temperature, respectively. The vibrational Helmholtz free energy $A_{vib}$ is formulated as [52]:

$$A_{vib} = nK_BT\left[\frac{9\theta}{8T} + 3Ln\left(1 - e^{-\theta/T}\right) - D(\frac{\theta}{T})\right] \tag{4.27}$$

Here, n, $K_B$ and $D(\frac{\theta}{T})$ represent the number of atoms per formula unit, Boltzmann constant and the Debye integral, respectively. Pertinently, for an isotropic solid $\theta_D$ is given as follows [53]:

$$\theta_D = \frac{\hbar}{K_B}\left[6\pi^2V^{1/2}n\right]^{1/3} f(\sigma)\sqrt{\frac{B_S}{M}} \tag{4.28}$$

Where M and $B_S$ represent the molecular mass per unit cell and the adiabatic bulk modulus, respectively. The latter can be written as follows:

$$B_S \cong B_V = V\left(\frac{d^2E(V)}{dV^2}\right) \tag{4.29}$$

The function $f(\sigma)$ is given by reference [54]. Therefore, the minimization of non-equilibrium Gibbs function (Eq. (4.26)) with respect to volume (V), can be achieved as:

$$\left(\frac{\partial G^*(V, P, T)}{\partial V}\right)_{P,T} = 0 \tag{4.30}$$

By solving the Equation. (4.30), we obtain the thermal equation of states (EOS). The isothermal bulk modulus ($B_T$), heat capacity at constant volume ($C_V$), heat capacity at constant pressure ($C_P$) and the thermal expansion coefficient ($\alpha$) are given as follows [55]:

$$B_T(P, V) = V\left(\frac{\partial^2 G^*(V, P, T)}{\partial V^2}\right)_{P,T} \tag{4.31}$$

$$C_V = 3nK_B\left[4D\left(\frac{\theta}{T}\right) - \frac{3\theta/T}{e^{\theta/T} - 1}\right] \tag{4.32}$$

$$C_P = C_V(1 + \gamma\alpha T) \tag{4.33}$$

$$\alpha = \frac{\gamma C_V}{B_T V} \tag{4.34}$$

Herein, $\gamma$ is the Grüneisen parameter, which is expressed as:

$$\gamma = \frac{\partial \mathrm{Ln}\theta_D}{\partial \mathrm{Ln}V} \tag{4.35}$$

The entropy (S) has been computed by applying the following expression [53]:

$$S_V = nK_B \left[4D\left(\frac{\theta}{T}\right) - 3\mathrm{Ln}\left(1 - e^{-\theta/T}\right)\right] \tag{4.36}$$

### 4.7.3 Heat capacity

Using the quasi-harmonic Debye model mentioned above, the thermodynamic properties of $KMgNO_{1-x}S_x$ and $FeTiCrAl_{1-x}Si_x$ alloys such that (x = 00, 0.25, 0.50, 0.75, 01) in the most stable phase are illustrated and determined from 0 to 700 K with a step of 100 K. The temperature effects on the heat capacity at constant volume and pressure ($C_V$ and $C_P$) are shown in Figure.4.12.

Heat capacity at constant volume ($C_V$) as a function of temperature increases sharply up to 250 K as depicted in Figure.4.12 a-c, this behavior follows Debye's $T^3$ law. At high temperatures, the atoms of a solid behave like those of a monatomic gas at temperature T. Under the effect of thermal agitation, these atoms acquire a vibration energy of 3RT per mole (where R is the molar constant of ideal gases). Half of this energy (3/2RT) is the kinetic energy of the atoms, and the other half is their potential energy [56]. Therefore, at high temperatures, $C_V$ tends towards the Dulong-Petit limit ($C_V$ = 3RN=97.56 J/mol.K) [57] for all the studied systems; this pattern is common for all solids at high temperatures. This implies that at high temperatures the an-harmonic and pressure effects on $C_V$ are negligible.

On the other hand, the evolution of heat capacity at constant pressure ($C_P$) as a function of temperature is depicted in Figure.4.12-b-d. One can notice that at low temperatures (T < 250 K), the evolution pattern of $C_P$ is quite similar to that of $C_V$, that is to say, $C_P$ increases as $T^3$. While at high temperatures, this parameter ($C_P$) keeps increasing slightly as the temperature increases. Further, below 300 K, the S/Si concentration affects the heat capacity at constant volume and pressure. For the $KMgNO_{1-x}S_x$ alloy, both $C_v$ and $C_P$ increase with the decreasing of S in the doped system. While the heat capacity components ($C_V$ and $C_P$) decrease by increasing the concentration of silicon in $FeTiCrAl_{1-x}Si_x$ alloys.

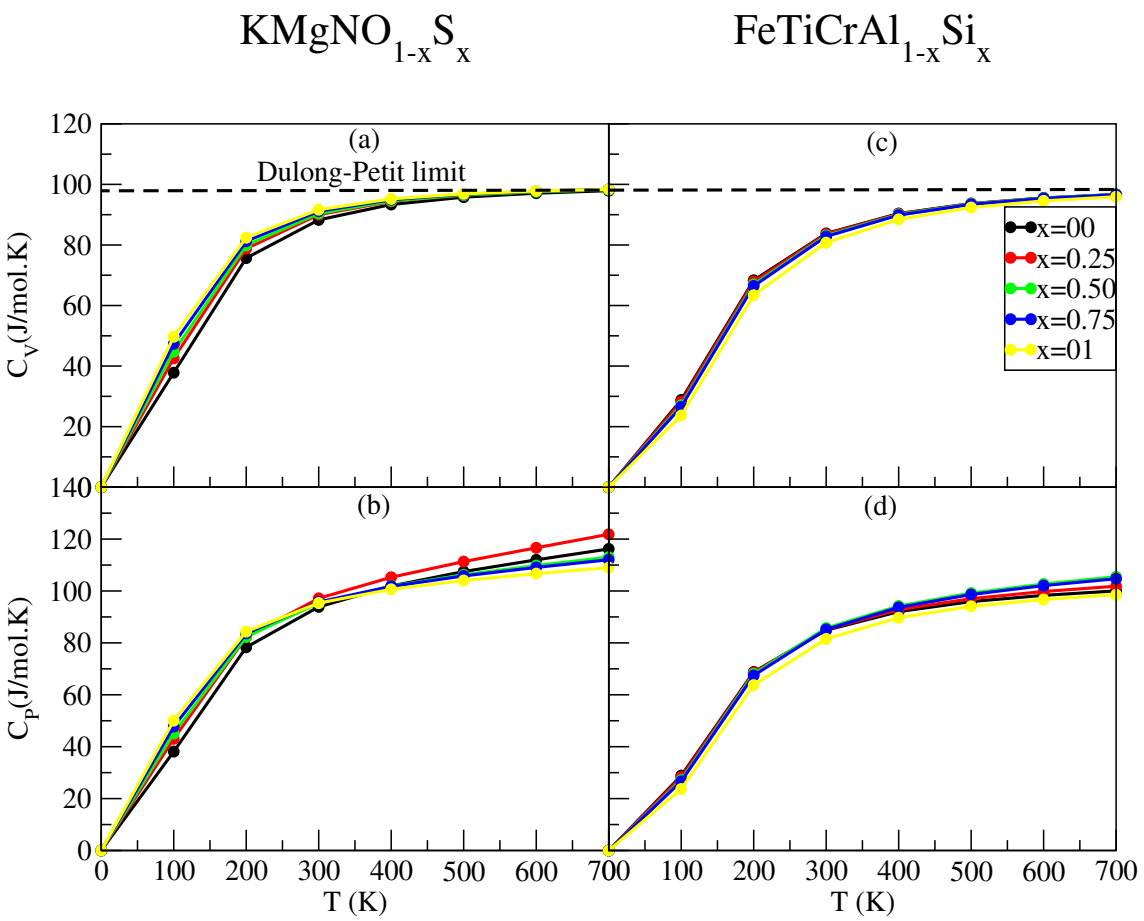


Figure 4.12: The heat capacity as a function of temperature.

### 4.7.4 Thermal expansion

The most direct effect of thermal agitation on a material lies in thermal expansion ($\alpha$). This effect arises from the increase in the average interatomic distance due to thermal agitation. This parameter is caused by the increase in volume occupied by atoms or molecules as the amplitude of their random vibrations increases with temperature. For the majority of materials, it is proportional to the change in temperature. Thermal expansion is manifested by an increase in the average distance between atoms due to the asymmetrical form of the potential energy well rather than due to the kinetics of atomic vibrations. Furthermore, the thermal expansion coefficient explains how an object's size varies when its temperature changes. More precisely, at constant pressure, it measures the fractional change in size for every degree of temperature variation. [56].

To study the effect of temperature and concentration on the thermal expansion coefficient of $KMgNO_{1-x}S_x$ and $FeTiCrAl_{1-x}Si_x$ alloys ($0 \leq x \leq 1$) in the most stable phase of each alloy, the main contribution to thermal expansion comes from lattice vibrations. In equilibrium, atoms in a crystal vibrate around their average positions. As the temperature increases,

more thermal energy is injected into the crystal, and the atoms vibrate with increasing amplitude. The average separation distance between atoms also increases with rising temperature, causing thermal expansion.

The evolution of this parameter ($\alpha$) versus temperature of the investigated materials is illustrated diagrammatically in Figure.4.13-c. It can be seen that at temperatures below 200 K, the parameter $\alpha$ grows linearly and sharply with temperature, revealing a similar behavior as both of $C_V$ and $C_P$. When the temperature is higher than 300 K, the thermal expansion coefficient $\alpha$ approaches a linear increase. The growth rate becomes moderate, which means that the temperature dependence of $\alpha$ is very weak for high temperatures and tends to converge to an almost constant value, hence the an-harmonic effect is negligible. Moreover, it can be noted that the concentration of S and Si affects the thermal expansion of the doped systems.

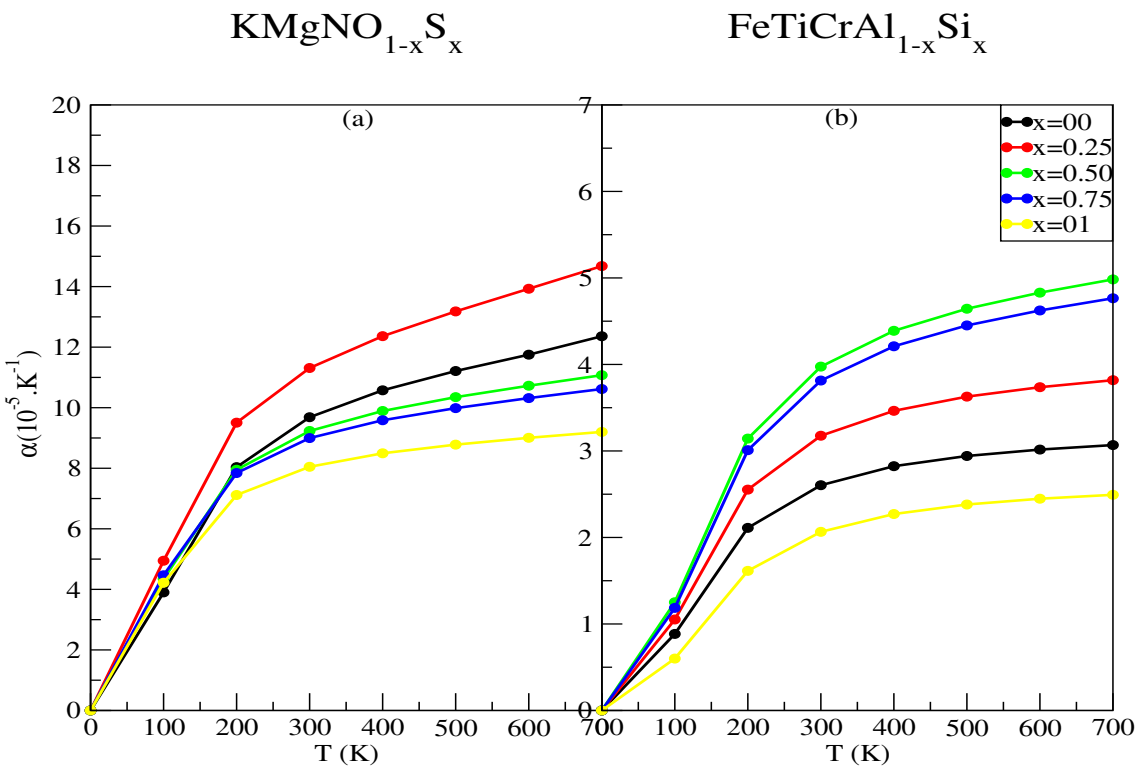


Figure 4.13: Thermal expansion as a function of temperature.

### 4.7.5 Debye temperature

The Debye temperature $\theta_D$, which corresponds to the crystal's maximum normal vibration mode, links thermodynamic parameters including specific heat, lattice enthalpy, thermal conductivity, phonons, and thermal expansion with elastic properties. Besides, above this temperature, quantum effects can be neglected. However, below the Debye temperature,

quantum mechanical effects are very important to understand thermodynamic properties. Besides, Debye temperature is generally related to the strength of chemical bonds and is proportional to the speed of sound, which increases with the hardness of the material [58]. The value of $\theta_D$ can vary greatly from one material to another, mainly depending on the type of bond. The more rigid the chemical bond, the higher $\theta_D$ will be. In addition, Debye temperature ($\theta_D$) is an important thermoelastic parameter that provides information about the material's hardness; materials with high Debye temperature reveal high hardness compared with those that have low $\theta_D$. The variation of $\theta_D$ as a function of temperature at constant pressure (P = 0 GPa) for the studied alloys is shown in Figure.4.14.

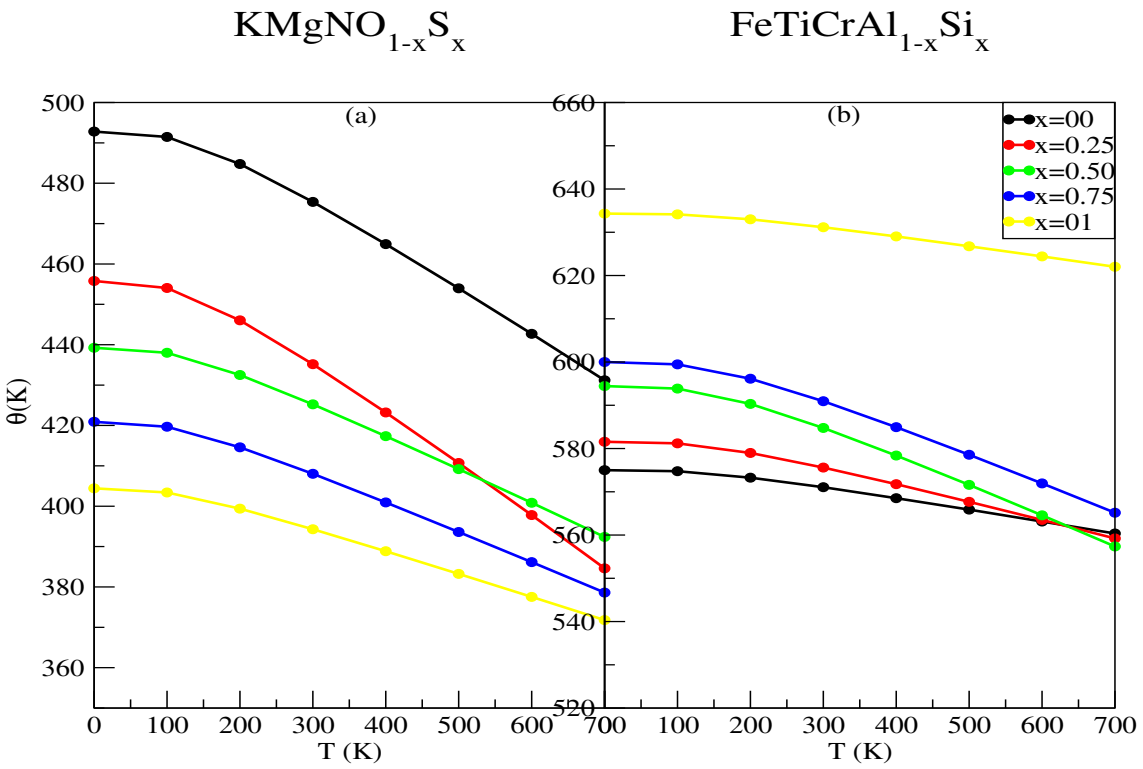


Figure 4.14: Debye temperature as a function of temperature.

It is clear that $\theta_D$ is almost constant below 100 K, whereas it decreases linearly from this temperature. We note that $\theta_D$ of $FeTiCrAl_{1-x}Si_x$ alloys is higher than that of $KMgNO_{1-x}S_x$ at a given temperature, indicating a better stiffness and a stronger interatomic force of Fe-based systems. This result corroborates the previous findings from the structural and mechanical properties. In generally, compounds with high bulk modulus have high debye temperature. From the previous results, for $KMgNO_{1-x}S_x$ alloys the bulk modulus decreases linearly (follows Vegard low), hence $\theta_D$ decreases by increasing the S concentration. While, for $FeTiCrAl_{1-x}Si_x$ materials, the bulk modulus increases with the increasing of Si, hence $\theta_D$ increases with x (x = 00, 0.25, 0.50, 0.75 and 01). Furthermore, the high values of $\theta_D$ imply

that even at higher temperatures, the considered quaternary Heusler alloys can be used for application purposes.

### 4.7.6 Entropy

The dispersion of energy and matter is described by entropy; it is denoted by the symbol S. On a microscopic scale, entropy can be defined as a measure of the disorder of a system. The variation of entropy S with respect to temperature of $KMgNO_{1-x}S_x$ and $FeTiCrAl_{1-x}Si_x$ alloys is shown in Figure.4.15. It can be seen that entropy for these systems increases almost linearly with increasing temperature. Additionally, one can notice that the effect of the concentration on the entropy of the parent compounds and the doped alloys can be neglected. These obtained values of S are purely predictive since we have no experimental data.

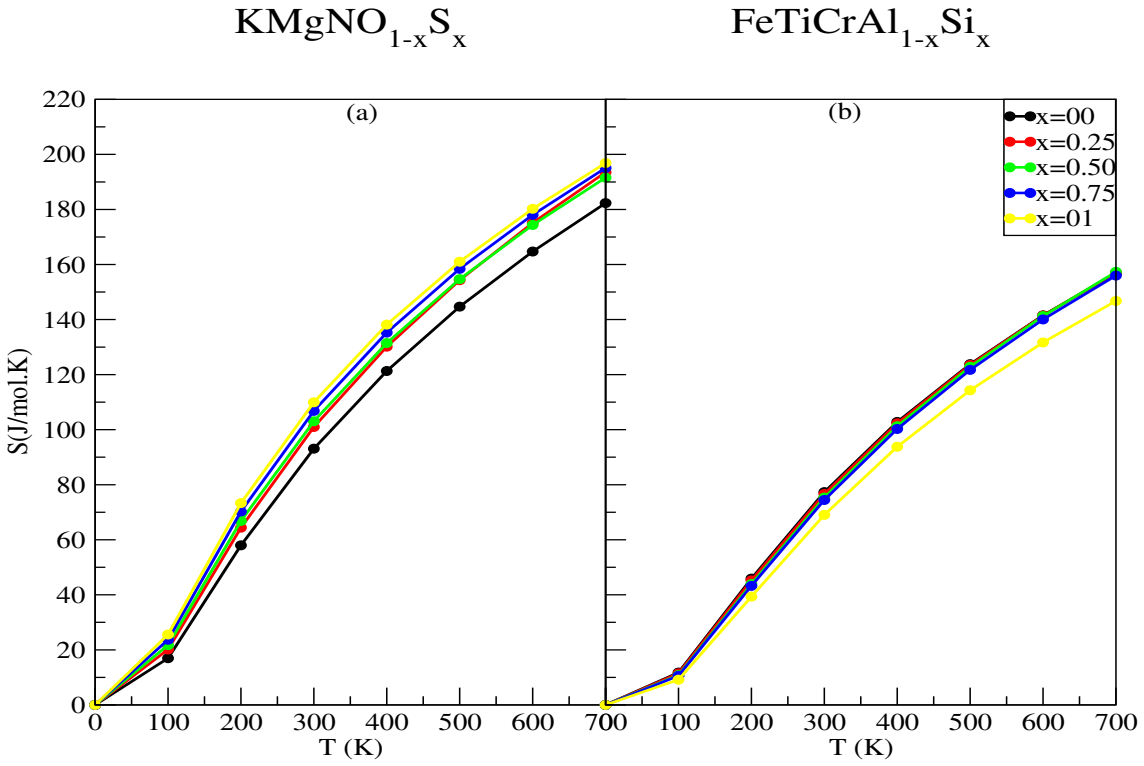


Figure 4.15: The entropy as a function of temperature.

### 4.7.7 Thermodynamic properties at different pressures

To give more data on thermodynamic properties for the $KMgNO_{1-x}S_x$ and $FeTiCrAl_{1-x}Si_x$ alloys, we report in Table.4.11 and Table.4.12, the values of the heat capacity, thermal expansion, Debye temperature and the entropy under different pressures and constant temperature. It can be seen that all the mentioned thermodynamic parameters, namely, $C_V$, $C_P$, $\alpha$ and S,

decrease by increasing the pressure from 00 to 10 GPa. While the Debye temperature $\theta_D$ increases with the increasing of the pressure for all doped systems.

Table 4.11: Heat capacity $C_V/C_P$ , thermal expansion $\alpha$, Debey temperature $\theta_D$ and entropy S at different pressure P and constant temperature (300 K) for $KMgNO_{1-x}S_x$ alloys.

| **x** | P(GPa) | $C_V$(J/mol.K) | $C_P$(J/mol.K) | $\alpha(10^-5/K)$ | $\theta_D$(K) | S(J/mol.K) |
|---|---|---|---|---|---|---|
| | 00 | 8.828970E+1 | 9.387148E+1 | 9.685366E+0 | 475 | 9.30998E+1 |
| x=00 | 05 | 8.451917E+1 | 8.845454E+1 | 7.133188E+0 | 556 | 7.94919E+1 |
| | 10 | 8.103312E+1 | 8.400628E+1 | 5.620937E+0 | 626 | 6.97434E+1 |
| | 00 | 3.600666E+2 | 3.885777E+2 | 1.131185E+1 | 435 | 4.03906E+2 |
| x=0.25 | 05 | 3.437210E+2 | 3.625434E+2 | 7.822962E+0 | 527 | 3.36502E+2 |
| | 10 | 3.286836E+2 | 3.423740E+2 | 5.950302E+0 | 604 | 2.90792E+2 |
| | 00 | 3.617097E+2 | 3.812023E+2 | 9.231506E+0 | 425 | 4.12249E+2 |
| x=0.50 | 05 | 3.480093E+2 | 3.616892E+2 | 6.733739E+0 | 504 | 3.51954E+2 |
| | 10 | 3.35311E+2 | 3.456719E+2 | 5.298352E+0 | 571 | 3.09503E+2 |
| | 00 | 3.644892E+2 | 3.829623E+2 | 8.998020E+0 | 408 | 4.27263E+2 |
| x=0.75 | 05 | 3.513072E+2 | 3.642469E+2 | 6.539267E+0 | 486 | 3.64785E+2 |
| | 10 | 3.390669E+2 | 3.488881E+2 | 5.142465E+0 | 551 | 3.21086E+2 |
| | 00 | 9.166091E+1 | 9.537333E+1 | 8.047376E+0 | 394 | 1.09943E+2 |
| x=01 | 05 | 8.871824E+1 | 9.139326E+1 | 5.990937E+0 | 465 | 9.49342E+1 |
| | 10 | 8.597596E+1 | 8.804856E+1 | 4.789823E+0 | 526 | 8.42837E+1 |

Table 4.12: Heat capacity $C_V/C_P$ , thermal expansion $\alpha$, Debey temperature $\theta_D$ and entropy S at different pressure P and constant temperature (300 K) for $FeTiCrAl_{1-x}Si_x$ alloys.

| x | P(GPa) | $C_V$(J/mol.K) | $C_P$(J/mol.K) | $\alpha(10^{-}5/K)$ | $\theta_D$(K) | S(J/mol.K) |
|---|---|---|---|---|---|---|
| x=00 | 00 | 8.380024E+1 | 8.486346E+1 | 2.603640E+0 | 571 | 7.73012E+1 |
| | 05 | 8.240344E+1 | 8.335665E+1 | 2.373830E+0 | 599 | 7.33269E+1 |
| | 10 | 8.105170E+1 | 8.191293E+1 | 2.180510E+0 | 626 | 6.97901E+1 |
| x=0.25 | 00 | 3.343010E+2 | 3.407043E+2 | 3.175502E+0 | 576 | 3.06547E+2 |
| | 05 | 3.275070E+2 | 3.330979E+2 | 2.830132E+0 | 609 | 2.87661E+2 |
| | 10 | 3.209630E+2 | 3.258989E+2 | 2.549511E+0 | 641 | 2.71184E+2 |
| x=0.50 | 00 | 3.324775E+2 | 3.428045E+2 | 3.975450E+0 | 585 | 3.01280E+2 |
| | 05 | 3.157280E+2 | 3.231609E+2 | 3.013121E+0 | 666 | 2.59029E+2 |
| | 10 | 3.003581E+2 | 3.059960E+2 | 2.402446E+0 | 737 | 2.27586E+2 |
| x=0.75 | 00 | 3.312412E+2 | 3.408112E+2 | 3.813699E+0 | 591 | 2.97794E+2 |
| | 05 | 3.151850E+2 | 3.221874E+2 | 3.292555E+0 | 669 | 2.57815E+2 |
| | 10 | 3.004082E+2 | 3.057823E+2 | 2.697578E+0 | 737 | 2.27680E+2 |
| x=01 | 00 | 8.075941E+1 | 8.153605E+1 | 2.064883E+0 | 631 | 6.90610E+1 |
| | 05 | 7.833615E+1 | 7.899049E+1 | 1.793513E+0 | 677 | 6.34406E+1 |
| | 10 | 7.604641E+1 | 7.660688E+1 | 1.582488E+0 | 720 | 5.87238E+1 |

## 4.8 Conclusion

This work was designed to study the physical properties of new innovative materials called $d^0$ Heusler alloys: $KMgNO_{1-x}S_x$ and $FeTiCrAl_{1-x}Si_x$ such that (x = 0, 0.25, 0.5, 0.75 and 01). For this purpose, we used an ab-initio method called linearized augmented plane waves (FP-LAPW) in the framework of density functional theory (DFT). The exchange and correlation potential is treated using the GGA approach to calculate the total energy. While the exchange and correlation potential is treated in mBJ and GGA + U to calculate the electronic and magnetic properties. Our study has provided a detailed description of the structural, electronic, magnetic, and thermodynamic properties, such as structural optimization, band structure, total and partial density of states, magnetic moment, spin polarization and the effect of temperature and pressure on some macroscopic parameters for each alloy.

The main results are summarized as follows:

- The whole series of $KMgNO_{1-x}S_x$ and $FeTiCrAl_{1-x}Si_x$ (x = 00, 0.25, 0.50, 0.75 and 01) Heusler alloys are more stable in type I in the ferromagnetic (FM) state.
- The negative formation energy and the positive cohesive energy reveal the thermodynamic and physical stability of these alloys.
- The variation of lattice parameter ($a_0$) and bulk modulus ($B_0$) versus S/Si concentration

follows Vegard's law, thus showing a concordance between the DFT calculations and this law. Further, the elastic constants $C_{ij}$ predict the mechanical stability of the considered alloys.

- Using ELATE software, the three-dimensional (3D) plots of the mechanical parameters, namely, Young's modulus (E), Poisson's ratio ($\nu$), hardness (H) and shear modulus (G) prove the anisotropic feature of the parent compounds and the doped alloys, which is predicted using the anisotropic factor (A).

- Band structures and density of states (DOS) curves show that these materials are half-metallic ferromagnets with a complete spin polarization (100%), except FeTiCrAl.

- The density of states shows a semiconducting feature of FeTiCrAl and the half-metallic character of $FeTiCrAl_{1-x}Si_x$ (x = 0.25, 0.50, 0.75 and 01) compounds using mBJ and GGA + U approximations.

- High Curie temperature and perfect spin polarization of the materials at hand reflect their suitability for spintronic devices.

- The half-metallic character of $KMgNO_{1-x}S_x$ alloys mainly originated from the hybridization between p orbitals of N and O (S) atoms.

- The d-states of the transition metals (Fe, Ti and Cr) in $FeTiCrAl_{1-x}Si_x$ alloys are making metallic intersection at $E_F$ in the spin down configuration, resulting in the half-metallic nature of (x = 0.25, 0.50, 0.75 and 01) alloys.

- The total magnetic moment reaches an integer value ($M_{tot} = 2\mu_B$) for the parent compounds KMgNZ (Z = O or S) and their doped system $KMgNO_{1-x}S_x$ (x = 0.25, 0.50 and 0.75), thus the concentration of the S atom does not effect $M_{tot}$.

- The parent compounds FeTiCrAl and FeTiCrSi have an integer value of the total magnetic moment, following the Slater-Pauling curve of $M_{tot} = |Z_t - 24|$.

- The total magnetic moment of the doped system $FeTiCrAl_{1-x}Si_x$ (x = 0.25, 0.50 and 0.75) alloys has a non-integer value, hence the accordance between $M_{tot}$ and SP rule disappears for these alloys. Thereby, the concentration of Si atom effects the total magnetic moment ($M_{tot}$) of $FeTiCrAl_{1-x}Si_x$.

- In the literature, we did not find any experimental or theoretical value that allows us to make the comparison with our calculated results of our alloys for the concentrations

(x = 0.25, 0.5, 0.75). We consider that our values will serve as a database for the prediction in the study of these alloys.

- The thermodynamic properties are predicted by the quasi-harmonic Debye model in the pressure range of 0 to 10 GPa and temperature range of 0 to 700 K. This study allowed us to have a global idea on the effect of temperature and pressure on certain macroscopic parameters such as the heat capacities $C_v$ and $C_p$, the thermal expansion coefficient $\alpha$, Debye temperature $\theta_D$ and the entropy S.

# REFERENCES


[1] N. Viglin, V. V. Ustinov, and V. V. Osipov, "Spin injection maser," *JETP Letters*, vol. 86, pp. 193–196, 2007.

[2] T. Klimczuk, C. Wang, K. Gofryk, F. Ronning, J. Winterlik, G. H. Fecher, J.-C. Griveau, E. Colineau, C. Felser, J. D. Thompson, *et al.*, "Superconductivity in the heusler family of intermetallics," *Physical Review B—Condensed Matter and Materials Physics*, vol. 85, no. 17, p. 174505, 2012.

[3] P. Blaha, K. Schwarz, G. Madsen, D. Kvasnicka, and J. Luitz, "WIEN2k, An Augmented Plane Wave Plus Local Orbitals Program for Calculating Crystal Properties (Vienna University of Technology, Austria, 2001)," *Google Scholar There is no corresponding record for this reference*, 2002.

[4] P. Hohenberg and W. Kohn, "Density functional theory (DFT)," *Phys. Rev*, vol. 136, p. B864, 1964.

[5] O. K. Andersen, "Linear methods in band theory," *Phys. Rev. B*, vol. 12, pp. 3060–3083, Oct 1975.

[6] P. Giannozzi, S. Baroni, N. Bonini, M. Calandra, R. Car, C. Cavazzoni, D. Ceresoli, G. L. Chiarotti, M. Cococcioni, I. Dabo, *et al.*, "Quantum espresso: a modular and open-source software project for quantum simulations of materials," *Journal of physics: Condensed matter*, vol. 21, no. 39, p. 395502, 2009.

[7] A. D. Becke and E. R. Johnson, "A simple effective potential for exchange," *The Journal of chemical physics*, vol. 124, no. 22, 2006.

[8] F. D. Murnaghan, "The compressibility of media under extreme pressures," *Proceedings of the National Academy of Sciences*, vol. 30, no. 9, pp. 244–247, 1944.

[9] R. Dhakal, S. Nepal, I. Galanakis, R. P. Adhikari, and G. C. Kaphle, "Prediction of half-metallicity and spin-gapless semiconducting behavior in the new series of FeCr-based quaternary heusler alloys: an ab initio study," *Journal of Alloys and Compounds*, vol. 882, p. 160500, 2021.

[10] J. Du, S. Dong, X. Wang, H. Zhao, L. Wang, and L. Feng, "First-principles study on the half-metallic properties of the d quaternary heusler compounds: KCaCBr and KCaCI," *AIP Advances*, vol. 6, no. 10, 2016.

[11] H. Frioui, A. Meddour, and M. H. Gous, "Structural, mechanical, electronic, magnetic, optical, and thermoelectric properties of a new equiatomic quaternary heusler compound FeZrCrZ (Z= Si, Ge, Sn): A first-principles investigation," *Materials Science in Semiconductor Processing*, vol. 182, p. 108697, 2024.

[12] A. Boumaza, S. Ghemid, H. Meradji, O. Nemiri, R. Belghit, F. Oumelaz, L. Hamioud, M. Gous, R. Khenata, S. B. Omran, *et al.*, "DFT-Based calculations of the structural stability, electronic and elastic characteristics of $BBi_{1-x}Sb_x$ ternary ordered alloys," *Journal of Electronic Materials*, vol. 50, pp. 598–612, 2021.

[13] P. Kurz, G. Bihlmayer, and S. Blügel, "Magnetism and electronic structure of hcp Gd and the Gd (0001) surface," *Journal of Physics: Condensed Matter*, vol. 14, no. 25, p. 6353, 2002.

[14] X.-P. Wei, Y.-D. Chu, X.-W. Sun, and J.-B. Deng, "First-principles study on stability, electronic and thermodynamic properties of $Ti_2CoIn$ and $Ti_2NiIn$," *The European Physical Journal B*, vol. 86, pp. 1–7, 2013.

[15] J. Kübler, G. Fecher, and C. Felser, "Understanding the trend in the Curie temperatures of $Co_2$-based heusler compounds: Ab initio calculations," *Physical Review B—Condensed Matter and Materials Physics*, vol. 76, no. 2, p. 024414, 2007.

[16] L. Vegard, "The constitution of the mixed crystals and the filling of space of the atoms," *Zeitschrift Fur Physik*, vol. 5, pp. 17–26, 1921.

[17] M. J. Mehl, B. M. Klein, and D. A. Papaconstantopoulos, "Intermetallic compounds: principle and practice," *Principles*, vol. 1, pp. 195–210, 1995.

[18] M. Matougui, B. Bouadjemi, M. Houari, A. Zitouni, T. Lantri, S. Haid, S. Bentata, B. Bouhafs, Z. Aziz, and R. Khenata, "Electronic structure, mechanical and thermoelectric properties of the full heusler $Ba_2AgZ(Z = Bi, Sb)$ alloys: insights from DFT study," *Indian Journal of Physics*, vol. 95, no. 12, pp. 2675–2686, 2021.

[19] P. Blaha, K. Schwarz, G. Madsen, D. Kvasnicka, J. Luitz, R. Laskowsk, F. Tran, L. Marks, and L. Marks, *WIEN2k: An Augmented Plane Wave Plus Local Orbitals Program for Calculating Crystal Properties*. Techn. Universitat, 2019.

[20] H. ABBASSA, "Contribution à l'étude des propriétés physico-chimiques des alliages d'Heusler," *Université de Mostaganem, Thèse*, 2015.

[21] G. Sin'ko and N. Smirnov, "On elasticity under pressure," *Journal of Physics: Condensed Matter*, vol. 16, no. 45, p. 8101, 2004.

[22] M. Fine, L. Brown, and H. Marcus, "Elastic constants versus melting temperature in metals," *Scripta metallurgica*, vol. 18, no. 9, pp. 951–956, 1984.

[23] R. Hill, "The elastic behaviour of a crystalline aggregate," *Proceedings of the Physical Society. Section A*, vol. 65, no. 5, p. 349, 1952.

[24] S. Pugh, "XCII. relations between the elastic moduli and the plastic properties of polycrystalline pure metals," *The London, Edinburgh, and Dublin Philosophical Magazine and Journal of Science*, vol. 45, no. 367, pp. 823–843, 1954.

[25] I. Frantsevich, F. Voronov, and S. Bokuta, "Elastic Constants and Elastic Moduli of Materials and Insulators," *Naokova Dumka, Kiev*, 1983.

[26] S. S. Essaoud and A. S. Jbara, "First-principles calculation of magnetic, structural, dynamic, electronic, elastic, thermodynamic and thermoelectric properties of $Co_2ZrZ(Z = Al, Si)$ heusler alloys," *Journal of Magnetism and Magnetic Materials*, vol. 531, p. bib40, 2021.

[27] A. Afaq, M. Shanian, and A. Bakar, "First-Principles study for structural, elastic and mechanical properties of CuCoMnZ (Z= Si, Sn, Sb) heusler alloys," *Materials Research Express*, vol. 6, no. 2, p. 026522, 2018.

[28] Y. Tian, B. Xu, and Z. Zhao, "Microscopic theory of hardness and design of novel superhard crystals," *International Journal of Refractory Metals and Hard Materials*, vol. 33, pp. 93–106, 2012.

[29] B. Huang, Y.-H. Duan, W.-C. Hu, Y. Sun, and S. Chen, "Structural, anisotropic elastic and thermal properties of MB (M= Ti, Zr and Hf) monoborides," *Ceramics International*, vol. 41, no. 5, pp. 6831–6843, 2015.

[30] Q. Wu and S. Li, "Alloying element additions to $Ni_3Al$: Site preferences and effects on elastic properties from first-principles calculations," *Computational Materials Science*, vol. 53, no. 1, pp. 436–443, 2012.

[31] R. Gaillac, P. Pullumbi, and F.-X. Coudert, "ELATE: an open-source online application for analysis and visualization of elastic tensors," *Journal of Physics: Condensed Matter*, vol. 28, no. 27, p. 275201, 2016.

[32] R. Tesch and P. M. Kowalski, "Hubbard U parameters for transition metals from first principles," *Physical Review B*, vol. 105, no. 19, p. 195153, 2022.

[33] K. Nawa and Y. Miura, "Exploring half-metallic Co-based full heusler alloys using a DFT+U method combined with linear response approach," *RSC advances*, vol. 9, no. 52, pp. 30462–30478, 2019.

[34] A. Tange, C. Gao, B. Y. Yavorsky, I. Maznichenko, C. Etz, A. Ernst, W. Hergert, I. Mertig, W. Wulfhekel, and J. Kirschner, "Electronic structure and spin polarization of the Fe (001)-p ($1\times$ 1) o surface," *Physical Review B*, vol. 81, no. 19, p. 195410, 2010.

[35] S. Alay-e Abbas, K. M. Wong, N. Noor, A. Shaukat, and Y. Lei, "An ab-initio study of the structural, electronic and magnetic properties of half-metallic ferromagnetism in Cr-doped BeSe and BeTe," *Solid State Sciences*, vol. 14, no. 10, pp. 1525–1535, 2012.

[36] S. Dong, X.-S. Song, and H. Zhao, "Can binary sp half-metallic ferromagnets maintain half-metallicity when they form superlattices? A first-principles approach," *Physics Letters A*, vol. 378, no. 16-17, pp. 1208–1212, 2014.

[37] S. Noui, Z. Charifi, H. Baaziz, G. Uğur, and Ş. Uğur, "Effect of structure on the electronic, magnetic and thermal properties of cubic $Fe_2Mn_xNi_{1-x}Si$ heusler alloys," *Journal of Electronic Materials*, vol. 48, pp. 337–351, 2019.

[38] K. Kusakabe, M. Geshi, H. Tsukamoto, and N. Suzuki, "New half-metallic materials with an alkaline earth element," *Journal of Physics: Condensed Matter*, vol. 16, no. 48, p. S5639, 2004.

[39] M. Sieberer, J. Redinger, S. Khmelevskyi, and P. Mohn, "Ferromagnetism in tetrahedrally coordinated compounds of I/II-V elements: Ab initio calculations," *Physical Review B*, vol. 73, no. 2, p. 024404, 2006.

[40] Y. Chen, S. Chen, B. Wang, B. Wu, H. Huang, X. Qin, D. Li, and W. Yan, "Half-metallicity and magnetism of the quaternary heusler compound $TiZrCoIn_{1-x}Ge_x$ from the first-principles calculations," *Applied Sciences*, vol. 9, no. 4, p. 620, 2019.

[41] J. Du, S. Dong, X. Wang, H. Rozale, H. Zhao, L. Wang, and L. Feng, "Half-metallic ferromagnetism in KCaNX (X= O, S, and Se) quaternary Heusler compounds: A first-principles study," *Superlattices and Microstructures*, vol. 105, pp. 39–47, 2017.

[42] K. Belkacem, Y. Zaoui, S. Amari, L. Beldi, and B. Bouhafs, "First-Principles Study of the New Half-Metallic Ferromagnetic Quaternary-Heusler Alloys NaXNO (X= Ca, Sr, Ba)," in *Spin*, vol. 10, p. 2050022, World Scientific, 2020.

[43] H. T. Nguyen, V. T. Vi, T. V. Vu, N. V. Hieu, D. V. Lu, D. Rai, and N. T. Binh, "Spin–orbit coupling effect on electronic, optical, and thermoelectric properties of janus $Ga_2SSe$," *RSC advances*, vol. 10, no. 73, pp. 44785–44792, 2020.

[44] J. Du, S. Dong, X. Wang, H. Rozale, H. Zhao, L. Wang, and L. Feng, "Half-metallic ferromagnetism in KCaNX (X= O, S, and Se) quaternary Heusler compounds: A first-principles study," *Superlattices and Microstructures*, vol. 105, pp. 39–47, 2017.

[45] J. Kübler, "First principle theory of metallic magnetism," *Physica B+ C*, vol. 127, no. 1-3, pp. 257–263, 1984.

[46] S. Benatmane and B. Bouhafs, "Investigation of new $d^0$ half-metallic full-heusler alloys $N_2BaX$ (X= Rb, Cs, Ca and Sr) using first-principle calculations," *Computational Condensed Matter*, vol. 19, p. e00371, 2019.

[47] K. Özdoğan, E. Şaşıoğlu, and I. Galanakis, "Slater-pauling behavior in LiMgPdSn-type multifunctional quaternary heusler materials: Half-metallicity, spin-gapless and magnetic semiconductors," *Journal of Applied Physics*, vol. 113, no. 19, 2013.

[48] S. V. Faleev, Y. Ferrante, J. Jeong, M. G. Samant, B. Jones, and S. S. Parkin, "Unified explanation of chemical ordering, the Slater-Pauling rule, and half-metallicity in full heusler compounds," *Physical Review B*, vol. 95, no. 4, p. 045140, 2017.

[49] Q. Gao, I. Opahle, and H. Zhang, "High-throughput screening for spin-gapless semiconductors in quaternary heusler compounds," *Physical Review Materials*, vol. 3, no. 2, p. 024410, 2019.

[50] S. Pedro, R. Caraballo Vivas, V. Andrade, C. Cruz, L. Paixao, C. Contreras, T. Costa-Soares, L. Caldeira, A. Coelho, A. M. G. Carvalho, *et al.*, "Effects of Ga substitution on the structural and magnetic properties of half metallic $Fe_2MnSi$ Heusler compound," *Journal of Applied Physics*, vol. 117, no. 1, 2015.

[51] M. Youcef, *Recherche de nouveaux matériaux à propriétés spécifiques pour la spintronique*. PhD thesis, 2019.

[52] M. Blanco, E. Francisco, and V. Luana, "GIBBS: isothermal-isobaric thermodynamics of solids from energy curves using a quasi-harmonic Debye model," *Computer Physics Communications*, vol. 158, no. 1, pp. 57–72, 2004.

[53] M. Ameri, F. Belkharroubi, I. Ameri, Y. Al-Douri, B. Bouhafs, F. Z. Boufadi, A. Touia, K. Boudia, and F. Mired, "Ab initio calculations of structural, elastic, and thermodynamic properties of HoX (X= N, O, S and Se)," *Materials science in semiconductor processing*, vol. 26, pp. 205–217, 2014.

[54] M. Flórez, J. Recio, E. Francisco, M. Blanco, and A. M. Pendás, "First-principles study of the rocksalt–cesium chloride relative phase stability in alkali halides," *Physical Review B*, vol. 66, no. 14, p. 144112, 2002.

[55] E. Francisco, M. Blanco, and G. Sanjurjo, "Atomistic simulation of $SrF_2$ polymorphs," *Physical Review B*, vol. 63, no. 9, p. 094107, 2001.

[56] S. Noui, *Les alliages d'Heusler demi-métallique: étude théoriques des propriétés magnétiques et électroniques*. PhD thesis, UB1, 2019.

[57] P. L. Dulong and A.-T. Petit, *Recherches sur quelques points importans de la theorie de la chaleur*. 1819.

[58] L. Ravindran, "Fast, PA Korzhavyi, B. Johansson, J. Wills, and O. Eriksson,"Density functional theory for calculation of elastic properties of orthorhombic crystals: Application to $TiSi_2$,"," *J. Appl. Phys*, vol. 84, no. 9, pp. 4891–904, 1998.